



KfK 4827

Juli 1991

# **Zircaloy Oxidation and Cladding Deformation in PWR-Specific CORA Experiments**

**K. Minato, W. Hering, S. Hagen  
Hauptabteilung Ingenieurtechnik  
Projekt Nukleare Sicherheitsforschung**

**Kernforschungszentrum Karlsruhe**



**Kernforschungszentrum Karlsruhe**

**Hauptabteilung Ingenieurtechnik  
Projekt Nukleare Sicherheitsforschung**

**KfK 4827**

**ZIRCALOY OXIDATION AND CLADDING  
DEFORMATION IN PWR-SPECIFIC  
CORA EXPERIMENTS**

**K. Minato\*, W. Hering\*\*, S. Hagen**

**\*Japan Atomic Energy Research Institute (JAERI), Tokai-Mura**

**\*\*Institut für Kernenergetik und Energiesysteme (IKE), Stuttgart**

**Kernforschungszentrum Karlsruhe GmbH, Karlsruhe**

Als Manuskript gedruckt  
Für diesen Bericht behalten wir uns alle Rechte vor

Kernforschungszentrum Karlsruhe GmbH  
Postfach 3640, 7500 Karlsruhe 1

ISSN 0303-4003

## Abstract

At the Kernforschungszentrum Karlsruhe, Federal Republic of Germany (FRG), out-of-pile bundle experiments are performed in the CORA facility to investigate the behavior of light water reactor (LWR) fuel elements during severe fuel damage (SFD) accidents. Within the international cooperation the most significant phenomena such as cladding deformation, oxidation (especially the zirconium/ steam reaction), melt formation, melt release, and relocation which were found in all tests have been analyzed.

Especially at high temperatures, the heat release due to the exothermal zirconium/steam reaction causes a temperature escalation which influences the damage progression in the bundle. To investigate the phenomena related to the cladding oxidation, three tests of the PWR (pressurized-water reactor) -type were chosen: CORA-2, CORA-5, and CORA-12. From each bundle, which has been embedded in epoxy, several samples were cut and their horizontal and vertical cross sections were examined using an optical microscope.

The main interest was focused on the understanding of the oxidation behavior of the fuel rod claddings and the mechanisms of cladding deformation. In addition, a comparison between test CORA-2 and CORA-5 considering the different test conditions has been performed. The influence of the test termination by flooding the test section with water from the bottom (quenching) was investigated with test CORA-12.

In general, the oxidation behavior shows a strong dependency on the axial temperature profile, dividing the bundle into several zones. Below 0.15 m the claddings are slightly oxidized whereas in the middle and upper part a nearly complete oxidation is found. In the middle the oxidation is often stopped by relocated melt which solidified at the cladding surface. In the upper part the oxidation is stopped by lack of unoxidized material due to melt and release of the innermost zircaloy layer. In this region the oxidized cladding is composed of an outer  $ZrO_2$  layer, which has been formed below the melting point of  $\alpha$ -zircaloy and an inner oxidized part, which was formed after the release of melt. The thickness of the oxide scales observed shows a variation from one rod to another at the same elevation as well as an azimuthal variation at each rod.

To investigate the influence of the test history an test sequence diagram was developed which allows a detailed analysis of the sequence of phenomena as well as a comparison between different tests. So the damage behavior of the bundle CORA-2 was mainly affected by ballooning and bursting at around 0.6 m, so that the transient started at this elevation. At CORA-5 , the absorber rod in the central position of the bundle released absorber melt which was sprayed over the whole cross section of the 25 rod bundle, leading to cladding failure due to eutectic reactions between Ag, In, and Zr.

In all analyzed tests a special type of cladding deformation ("flowering") was found in the high temperature region of the bundle. Due to the increase of the cladding surface, which can be oxidized further, the release of energy due to the cladding oxidation is enhanced, rising the initial heat-up rate. To explain this phenomenon a model will be proposed, which is based on all observations performed so far.

## Zusammenfassung

Am Kernforschungszentrum Karlsruhe werden in der Bündeltestanlage CORA Out-of-pile Experimente zur Untersuchung des Verhaltens von Leichtwasser-Reaktor (LWR)-Brennelementen unter Bedingungen, wie sie bei schweren Kernschäden (Severe fuel damage, SFD) auftreten können, durchgeführt. Im Rahmen der internationalen Kooperation wurde der Einfluß der wichtigsten Phänomene wie z. B. der Hüllrohrdeformation, der Hüllrohroxidation (Zirkon-Wasser-Reaktion), der Schmelzebildung, -freisetzung und -verlagerung auf den weiteren Schadensablauf im Bündel untersucht.

Speziell bei Temperaturen über 1500 K beeinflußt die Temperaturskalation durch die Wärmefreisetzung der exothermen Hüllrohroxidation die Schadensausbreitung im Bündel. Um die sich aus der Hüllrohroxidation ergebenden Phänomene zu untersuchen, wurden drei Druckwasserreaktor (DWR)-spezifische Tests, CORA-2, CORA-5 und CORA-12, ausgewählt. Die in Epoxidharz eingegossenen Bündel wurden in mehrere Bündelblöcke zersägt, so daß sowohl Quer- als auch Längsschnitte vorliegen. Von jedem Versuch wurden alle Querschnittsflächen, die bereits für metallurgische Analysen präpariert wurden mittels optischer Mikroskopie untersucht.

Ein Hauptziel ist die Untersuchung der axialen Verteilung der Oxidschichtdicken der Hüllrohre und des Zirkaloy-Shrouds. Ferner wurde der Einfluß unterschiedlicher Versuchsbedingungen anhand CORA-2 und CORA-5 sowie der Einfluß der Versuchsterminierung durch Fluten des Kühlkanals von unten mit Wasser (Quenchen) anhand CORA-12 analysiert.

Generell wird eine starke Abhängigkeit der axialen Verteilung der Oxidschichtdicken von der axialen Temperaturverteilung während des Versuchs beobachtet. Daher kann die ca. 1.0 m lange beheizte Zone des Stabbündel in drei axiale Zonen unterteilt werden: unterhalb von 0.15 m sind die Hüllrohre nur sehr leicht anoxidiert, während im mittleren Bereich die Oxidation durch Schmelzeanlagerungen gestoppt wird. Im oberen Drittel wird eine vollständige Oxidation aller Hüllrohre beobachtet, wobei durch Aufschmelzen und Verlagern von metallischem Zirkaloy die erreichbaren Oxidschichtdicken limitiert sind. In diesem Bereich setzt sich die Hülle aus zwei Schichten zusammen: einer äußeren  $ZrO_2$ -Schicht, die unterhalb der Schmelztemperatur von  $\alpha$ -Zirkaloy

gebildet wurde, und einer inneren Schicht, die erst durch Dampfzutritt nach der Schmelzefreisetzung entstand. Dabei variieren die innerhalb einer Bündelhöhe gemessenen Oxidschichtdicken beträchtlich sowohl azimuthal als auch von Stab zu Stab.

Zur Untersuchung des Einflusses des Versuchsablaufs auf den Bündelendzustand wurde ein Versuchsablaufdiagramm entwickelt, das auf Basis von Temperaturfront (TF)-Kurven sowohl eine zeitliche als auch eine axiale Lokalisierung der beobachteten Phänomene erlaubt. Damit ist ein Vergleich unterschiedlicher Tests unter Berücksichtigung der unterschiedlichen Versuchsbedingungen möglich. Mittels dieses Diagramms konnte für CORA-2 der Einfluß des Hüllrohrblähens und -berstens in ca. 0.6 m Bündelhöhe erkannt und bewertet werden. Ferner konnte in CORA-5 die Beeinflussung des Bündelverhaltens durch die Freisetzung von Schmelze aus dem zentral angeordneten Absorberstab abgeschätzt werden.

In allen untersuchten Tests wurden starke Hüllrohrdeformationen ("flowering") in Bündelbereichen mit hohen Temperaturen beobachtet. Da mit dieser Hüllrohrdeformation auch eine Freilegung von oxidierbarer Zirkaloyoberfläche verbunden ist, wird durch die dabei zusätzlich freigesetzte Energie die Bündelaufheizung beeinflusst. Um dieses Phänomen zu erklären, wurde ein neues Modell vorgestellt, das auf den bisherigen Beobachtungen basiert.



# Table of Contents

<b>1. Introduction</b> .....	<b>1</b>
<b>2. Description of the analyzed tests</b> .....	<b>3</b>
2.1 PWR-specific bundle components .....	3
2.2 General test description .....	4
2.3 Initial and boundary conditions .....	5
<b>3. Method and results of investigation</b> .....	<b>7</b>
3.1 Method of investigation .....	7
3.2 Results of CORA-2 .....	8
3.2.1 Description of the cross sections .....	8
3.2.2 End state of the claddings .....	8
3.2.3 Thickness of oxidized layers on the claddings .....	9
3.2.4 Oxidation behavior of the shroud .....	10
3.2.5 Cladding deformation .....	11
3.3 Results of CORA-5 .....	12
3.3.1 Description of the cross sections .....	12
3.3.2 End state of the claddings .....	13
3.3.3 Thickness of oxidized layers of the claddings .....	13
3.3.4 Oxidation behavior of the shroud .....	14
3.3.5 Behavior of the absorber rod .....	15
3.4 Results of CORA-12 .....	15
3.4.1 Description of the cross sections .....	15
3.4.2 End state of the claddings .....	16
3.4.3 Thickness of oxidized layers of the claddings .....	16
3.4.4 Oxidation behavior of the shroud .....	17
3.4.5 Behavior of the absorber rods .....	17
<b>4. Discussion of the results</b> .....	<b>19</b>
4.1 Behavior of heated and unheated fuel rods .....	19
4.2 Sequence of phenomena .....	20
4.2.1 CORA-2 bundle .....	20
4.2.2 CORA-5 bundle .....	22
4.2.3 CORA-12 bundle .....	23

4.3	Influence of test conditions	25
4.3.1	Initial and boundary conditions	25
4.3.2	Influence of quenching	27
4.4	Mechanisms of cladding deformation	29
4.4.1	Deformation due to high inner rod pressure	29
4.4.2	Deformation due to chemical interactions	29
<b>5.</b>	<b>Summary</b>	<b>32</b>
	<b>Appendix A. Acknowledgements</b>	<b>34</b>
	<b>Appendix B. References</b>	<b>35</b>
	<b>Appendix C. Detailed discription of the cross sections</b>	<b>37</b>
	<b>Appendix D. Tables</b>	<b>43</b>
	<b>Appendix E. Figures</b>	<b>49</b>

## List of Tables

Table 1.	CORA Test Matrix I	44
Table 2.	CORA Test Matrix II	45
Table 3.	Characteristics of bundles CORA-2, CORA-5, and CORA-12	46
Table 4.	List of the analyzed cross sections	47
Table 5.	Cladding outer oxide layer thicknesses	48
Table 6.	Outer diameter of the intact claddings of CORA-2	49

## List of Illustrations

Figure 1. Schematic overview of the CORA facility	50
Figure 2. Arrangements of the bundles	51
Figure 3. CORA-2, fuel rods at 268 mm elevation	52
Figure 4. CORA-2, rubble at 298 mm elevation	53
Figure 5. CORA-2, fuel rods at 480 mm elevation	54
Figure 6. CORA-2, fuel rods at 870 mm elevation	55
Figure 7. CORA-2, fuel rod, spacer and shroud at 870 mm elevation	56
Figure 8. CORA-2, shroud at 870 mm elevation	57
Figure 9. CORA-2, end state of the claddings	58
Figure 10. Outer oxidized layer thicknesses of CORA-2	59
Figure 11. CORA-2, axial and radial variation of the cladding state	60
Figure 12. Calculated outer oxidized layer thickness for CORA-2	61
Figure 13. CORA-2, flowering of the claddings	62
Figure 14. CORA-2, cladding deformation	63
Figure 15. CORA-2, radial growth of the claddings	64
Figure 16. CORA-2, calculated deformation of the claddings	65
Figure 17. CORA-5, fuel rods at 95 mm elevation	66
Figure 18. CORA-5, fuel rods at 208 mm elevation	67
Figure 19. CORA-5, fuel rods at 393 mm elevation	68
Figure 20. CORA-5, fuel rods at 408 mm elevation	69
Figure 21. CORA-5, fuel rod and spacer at 853 mm elevation	70
Figure 22. CORA-5, end state of the claddings	71
Figure 23. Outer oxidized layer thicknesses of CORA-5	72
Figure 24. CORA-5, axial and radial variation of the cladding state	73
Figure 25. CORA-5, shroud at around 270 mm elevation	74
Figure 26. CORA-5, central absorber rod	75
Figure 27. CORA-12, fuel rods at 216 mm elevation (1)	76
Figure 28. CORA-12, fuel rods at 216 mm elevation (2)	77
Figure 29. CORA-12, fuel rod and rubble at 533 mm elevation	78
Figure 30. CORA-12, end state of the claddings	79
Figure 31. Outer oxidized layer thicknesses of CORA-12	80
Figure 32. CORA-12, axial and radial variation of the cladding state	81
Figure 33. CORA-12, shroud oxidation	82
Figure 34. CORA-12, absorber rod	83

Figure 35. Isothermal diagram of CORA-2 .....	84
Figure 36. Isothermal diagram of CORA-5 .....	85
Figure 37. Isothermal diagram of CORA-12 .....	86
Figure 38. CORA-2, inner rod pressure .....	87
Figure 39. CORA-5, inner rod pressure .....	88
Figure 40. CORA-12, temperatures of fuel rods .....	89
Figure 41. Outer oxidized layer thicknesses .....	90
Figure 42. Comparison of the bundle end state .....	91
Figure 43. Comparison of the experimental conditions .....	92
Figure 44. Comparison of the remnants of the pellets .....	93
Figure 45. Mechanism of cladding deformation .....	94

## 1. Introduction

In the framework of the international cooperation of investigations on the light water reactor (LWR) fuel element behavior under severe fuel damage (SFD) conditions, out-of-pile bundle tests are performed in the CORA facility at the Kernforschungszentrum Karlsruhe (KfK) /1/. One main goal of the tests is to recognize the phenomena, their interactions, and their influence on the damage progression during heat-up and fast cool-down (quenching). Another goal is to complete the data base necessary for code verification, especially during heat-up when early melt formations and relocations occur.

So far eleven tests, eight pressurized water reactor (PWR) specific and three boiling water reactor (BWR) specific tests have been performed under various conditions (s. Table 1 and Table 2) /2/-/6/.

During the test, the on-line data, such as temperatures, initial fluid composition in the steam generator (s. Figure 1) system, and fuel rod pressures, were sampled and the optical inspections and documentation of the damage progression inside the bundle were performed using video cameras.

After the test the bundle end state is analyzed by two different kinds of investigation methods. One set of investigations tries to establish a global description of post-test bundle state based on axial profiles which describes the bundle cross section, the damage state, the bundle mass, the dissolution of the pellets, etc.. In this report an oxide profile is performed based on the optical inspection and examination of several cross sections by an optical microscope.

Other investigations are focused on the chemical reactions between the various reactor materials and their influence on the local damage progression. For this purpose metallurgical examinations using a scanning electron microscope (SEM) and microprobe analyses were performed at certain positions of the bundle /1/-/5/. The phenomena identified were investigated in detail in the separate effect tests mainly focused on the kinetics of chemical reactions and the chemical compositions of the resulting reaction products /7/-/11/.

In addition to the experimental work, analytical calculations have been performed using the stand-alone SCDAP computer code, which has been adapted

to the specific conditions of the CORA facility, to predetermine and to evaluate the CORA tests /12/,/13/.

Up to now the post-test bundle state of the first five tests, CORA-2 - CORA-15 (s. Table 1) have been examined using a computer assisted image analyzer /15/,/14/. So, in the horizontal cross sections the areas of residual pellets, which had not been affected at all, were identified. Together with the cross section areas of solid materials and those of the tungsten pins, the areas of the remnants of the claddings and relocated materials were calculated. Moreover, the positions and the size of coolant channel blockages and their coarse material composition were derived.

The main objective of the present investigation is an analysis of the overall oxidation behavior in the bundle including the Zircaloy (Zry-4) shroud. So the PWR-specific tests CORA-2, scheduled as a reference test, CORA-5, the first bundle with an absorber rod, and CORA-12, where the influence of the quenching was investigated, were selected for the analysis.

The bundle CORA-2 had no absorber rod and the observation holes (windows) in the shroud were quite large. In bundle CORA-5 the central unheated fuel rod was replaced by an absorber rod to investigate the influence of the absorber melt on the fuel rod behavior. Test CORA-12 was performed to analyze the behavior of a bundle, which was heated up to 2300 K, during quenching. Further, the Inconel spacer in the middle of the bundle was replaced by one made of Zry-4 in bundle CORA-12 (section 2).

Considering the different initial conditions, a comparison of these tests becomes very complicated. Therefore a special diagram has been established showing the sequence of phenomena observed and the relevant boundary conditions such as temperatures, damage progression in the bundle, thermohydraulic conditions and the electric power input. With these diagrams a global test analysis can be performed which allows an interpretation of the results of the post-test investigations. Moreover, different tests can be compared and the influence of the different test conditions can be quantified.

One phenomenon which was observed in all tests is the deformation of the cladding, which occurs at high temperatures. After a detailed analysis of this phenomenon a possible explanation of these deformations will be proposed (s. section 4).

## 2. Description of the analyzed tests

The three PWR-specific bundles, CORA-2, CORA-5, and CORA-12, have different goals (s. Table 1). To reach these goals different test conditions were used which cannot be neglected. In this section the different initial and boundary conditions will be discussed focused on their influence on the damage progression during test.

### 2.1 PWR-specific bundle components

Generally five different components were used to assemble a PWR-specific bundle. The geometric dimensions are given in the appendix (s. Table 3, /2/).

#### 1. *Heater rod:*

In the electrical heated out-of-pile experiment CORA the heat source is the central tungsten pin ( $\phi \sim 6\text{mm}$ ) of the heater rod. The annular  $\text{UO}_2$ -pellets, made of depleted uranium, separate the tungsten pin from the PWR-specific Zircaloy (Zry-4) -cladding. At the axial ends of the pellet stack (about 0.0 m and 1.0 m high), electrodes made of molybdenum ( $\phi \sim 8.6\text{mm}$ ), were connected to the tungsten pin.

#### 2. *Unheated rod:*

The PWR-specific Zry-4-cladding is filled with  $\text{UO}_2$ -pellets, made of depleted uranium. To measure bulk temperatures within the bundles, some pellets have a central hole ( $\phi \sim 1.8\text{ mm}$ ) which contains a high temperature thermocouple. The unheated rod is heated up by convection and radiation. It contains no heat source, except for the exothermal reaction (zirconium steam reaction) at temperatures above  $1200\text{ }^\circ\text{C}$ .

#### 3. *Absorber rod:*

The PWR-specific absorber rod is composed of a stainless steel (ss) -cladding which contains the absorber material (Ag,In,Cd) and is inserted in the guide tube made of Zry-4.

#### 4. *Shroud:*



The fuel rod bundle is surrounded by a 1.2 mm thick rectangular zircaloy liner which should provide a guidance of the fluid. A 20 mm thick ZrO<sub>2</sub>-fiber insulation is wrapped around the zircaloy shroud to reduce the radial heat losses so that a rather flat radial temperature distribution can be obtained. Up to ten observation holes in the Zry shroud and the insulation allow an optical inspection and documentation by video cameras of the damage progression in the bundle.

Nevertheless the high porosity of the insulation did not protect the outer surface of the shroud from steam exposure.

5. **Grid spacer:**

Two different types of grid spacers were used to arrange the bundle. The Zry spacer grid is a complex structure, made of Zry-4 and Inconel springs. The other spacer is completely made of Inconel-718.

## 2.2 **General test description**

### **Instrumentation**

The temperatures of the fuel rods, the fluid, the shroud, the fiber insulation and the high temperature shield (HTS) were measured at several axial bundle elevations by thermocouples. The inner pressure of some fuel rods and system pressure were also measured. The behavior of the bundle is observed and recorded by video system at ten axial bundle elevations through observation holes in the shroud and the fiber insulation (windows).

### **Test sequence**

Each CORA test is split into four phases, the preheating phase ( $0s < t < 3000s$ ), the heat-up phase ( $3000s < t < 3900s$ ), the escalation phase ( $3900s < t < 4900s$ ), and the cool-down phase ( $t > 4900s$ ), whereas in this report only the heat-up, the escalation, and the cool-down phases will be discussed.

The transient heat-up of each test starts at 3000s with the rise of the electric power to 6 kW. The fluid, at that time pure argon, is enriched by steam after 3300s, reaching a steady state fluid composition at 3600s. The temperature escalation due to the exothermal zirconium steam reaction occurs between

3900s and 4100s. At 4700s the electric power reaches the maximum value of about 28 kW which is shut down at about 4800s, starting the cool-down phase. The steam supply is stopped after and the bundle is cooled down.

The tests CORA-2 and CORA-5 were cooled down by a constant argon mass flow, whereas the test CORA-12 was terminated by quenching. To simulate the reflood phase the water surface in the quench tank was lifted over the bundle.

### **Post test analyses**

After the test, the HTS is lowered giving free access to the bundle, to allow an optical inspection and sample collection. Then the bundle is embedded in epoxy resin without moving the bundle, to fix the status of the bundle tested and avoid additional damage after the experiment. The embedded bundle is cut horizontally and vertically into several pieces. For metallurgical analyses some surfaces were grinded and polished.

## **2.3 Initial and boundary conditions**

### **CORA-2**

Two CORA-tests were run without any absorber rods as reference tests, CORA-2 for standard PWR-test and CORA-3 for high temperature test (up to 2400 °C). Bundle CORA-2 is composed of 16 heater rods and 9 unheated rods arranged by three grid spacers, the lower and the upper were made of Zry-4 whereas the middle one was made of Inconel-718 (s. Table 3). In this test the observation holes were quite large and located at the corner of the shroud (s. Figure 2).

The steady state mass flow of about 4 g/s argon and about 6 g/s steam is injected into the coolant channel. A certain amount of it will penetrate through the large (about 15 cm<sup>2</sup>) observation holes into the annulus (flow deviation), so that the net mass flow in the coolant channel is reduced. Further the internal fuel rod pressure of about 0.8 MPa at 400 °C (t=3000s) was large enough to cause ballooning of the claddings between 3800s and 3950s. This enhances the friction at the ballooned section so the amount of flow deviation increases, reducing the heat transfer and the cooling capacity of the fluid.

### **CORA-5**

At the CORA-5 bundle, the unheated rod at the central position was replaced by a PWR-specific absorber rod, so that the bundle has only 8 unheated rods (s. Figure 2). The axial arrangement of the grid spacer is similar to CORA-2 (s. Table 3). In this test the observation holes were closed by quartz plates so that no significant flow deviation into the annulus occurred.

In CORA-5 the quartz plates at the ten observation holes prevent a flow deviation and reduce the radiation losses. So the steady state mass flow of about 8 g/s argon and about 6 g/s steam remains in the coolant channel resulting in a higher fluid velocity. The internal fuel rod pressure of about 0.5 MPa at 340 °C ( $t=3000s$ ) was so low that no ballooning occurred, and the claddings failed by chemical perforation.

### **CORA-12**

In the bundle of test CORA-12 two unheated fuel rods were replaced by absorber rods, to simulated a PWR-specific arrangement of the absorber rods within a fuel element (FE). Moreover the lower two spacers were exchanged, so that the Inconel spacer was located below  $z=0.0$  m, outside the heated length of the bundle.

In CORA-12 the injected mass flow of about 8 g/s argon and about 6 g/s steam is reduced by a flow deviation into the annulus. The low internal fuel rod pressure avoided ballooning so that the claddings failed by chemical interaction leading to perforation. During test termination by quenching, a second damage was established in the bundle.

### **3. Method and results of investigation**

Each cross section of the three bundles shows various areas of quite different oxidation behavior. Therefore, all claddings at the cross sections have to be examined to get informations on the extent of the oxidation with respect to statistics. The method of the investigation will be described first, followed by the results of CORA-2, CORA-5, and CORA-12. In the descriptions of the results of each bundle, end state of the claddings, thickness of oxidized layers of the claddings, the oxidation behavior of the zircaloy shroud, etc., will be given. The detailed description of the analyzed cross sections is found in appendix C.

#### **3.1 Method of investigation**

The cross sections of the bundles were examined by optical microscope, with a magnification of up to 1000x. In several cases polarized light was used to distinguish phases.

The axial positions of the horizontal cross sections analyzed for the three tests, together with brief descriptions of each cross section, are listed in Table 4. In CORA-2 five polished horizontal cross sections were analyzed, which are located at elevations of *-13, 268, 298, 480, and 870 mm*. To allow a comparison of the CORA-5 test with the CORA-2 test, samples at relevant elevations have to be taken, but only polished samples at *95, 208, 393, 408, and 853 mm* were available. In addition to these five polished samples, one unpolished sample at *663 mm* was examined in CORA-5. In CORA-12 only two polished samples at *216 and 533 mm* were available, so that the unpolished samples at *51, 381, 711, and 876 mm* had to be used where detailed analyses could not be performed. Generally the upper surfaces of the samples were examined, except for the samples at *-13 mm* of the CORA-2 and at *533 mm* of the CORA-12 where the lower surfaces were used.

In order to understand the behavior of the absorber rods and the oxidation of the claddings and the shroud, some vertical cross sections of CORA-5 and CORA-12 were examined in addition to the horizontal cross sections.

The results of microprobe analysis on some of these samples performed at KfK /5/, /16/ were referred to identify chemical phases.

## **3.2 Results of CORA-2**

### **3.2.1 Description of the cross sections**

The first cross section, located below the heated zone of the bundle at -13 mm, shows a quite unaffected bundle state with only a few solidified melts on the zircaloy spacer. The second one (s. Figure 3) is located at 268 mm and gives informations on the top of the blocked zone formed by solidified melts. A short distance above, at 298 mm, no solidified melt but rubble was found on top of the blockage (s. Figure 4). The claddings were completely oxidized, consisting of two parts. One is a columnar structured outer  $ZrO_2$  layer, which was formed by oxidation of the cladding from the outside below the melting point of  $\alpha$ -Zr(O). The other is an inner oxidized part, which was formed by oxidation of molten Zry. The cross section at 480 mm reveals that the Inconel grid spacer melted down completely enhancing the damage of the claddings locally. The claddings were completely oxidized. The cross section at 870 mm can be divided into a central region (s. Figure 5) with small oxide scales and a corner region of the bundle near the shroud (s. Figure 7) showing large oxide scales. At this elevation the circumferential variation the oxidation state of the shroud (s. Figure 8) was investigated.

### **3.2.2 End state of the claddings**

The final appearance of the test bundle varies significantly even at the same elevation. Especially with respect to the evaluation of oxidation profiles the numbers of reacted or decayed rods have to be taken into account. In order to discuss the behavior of the bundle, it is important to clarify the end state of the claddings.

Figure 9 shows the end state of the claddings, where the state is classified in four groups: clad intact, clad missing, clad reacted, and clad flowered. At the

lowest position (-13 mm) all claddings are intact, but at other elevations observed the number of the intact claddings is small. Most of the remaining claddings are breached and deformed. Especially at the direct environment of the Inconel spacer nearly half of the claddings are missing (at 480 mm).

### 3.2.3 Thickness of oxidized layers on the claddings

As already pointed out, the main interest of this study is the analysis of the thickness of the  $ZrO_2$  layer, which has been formed from the outside below the melting point of  $\alpha-Zr(O)$ . It was found that the thickness was not uniform even at the same fuel rod and at the same axial elevation; the thickness of the outer  $ZrO_2$  layer varies circumferentially. Moreover, the mean layer thicknesses vary from one rod to another at the same elevation.

Figure 10 shows the azimuthal averaged outer  $ZrO_2$  layer thickness of each rod as a function of the axial elevation together with the maximum outer  $ZrO_2$  layer thicknesses of each rod at the corner positions of the bundle at 870 mm. The mean layer thickness is distributed widely. For example, at 298 mm elevation, it varies from 0.24 mm to 0.59 mm.

Table 5 lists the mean outer  $ZrO_2$  layer thicknesses and their standard deviations at each elevation. No significant difference in the thickness is seen between the heated rods and the unheated rods.

To evaluate these large variations, the mean outer  $ZrO_2$  layer thickness of each rod at 268, 298, 480, and 870 mm are plotted at horizontal cross sections in Figure 11, together with the clad end state as given in Figure 9.

At 268 mm the claddings were completely oxidized except for those in the blocked area. At 298 mm some claddings were completely lost. The position of these claddings was above the blocked area at 268 mm, suggesting that the loss of the claddings was caused by interaction with relocated melt. It is difficult to generalize the distribution of the layer thickness at these axial elevations, when the variation of the temperature is assumed to be small over the whole cross section.

At 480 mm the claddings of the central part of the bundle were lost except for one rod, whereas claddings remained at the outer part of the bundle. At

870 mm the claddings of the corners of the bundle were oxidized to a great extent at one side facing the shroud. But in the central part of the bundle at this elevation steam starvation must have occurred.

To assist these post-test investigations, calculations have been performed with the SCDAP/MOD1 code, which has been extended to handle the special properties of the out-of-pile test CORA /13/. In the calculation the conditions are more idealized (only outside oxidation considered) than in the experiment, so that a comparison with measured data could detect special phenomena /17/.

The oxide thicknesses calculated using a rate-law based on correlations show a maximum thickness of the outer  $ZrO_2$  layer of 0.4 mm at 0.35 m elevation. Due to the preceding melt relocation a complete consumption of the Zry stopped the oxidation, as shown in Figure 12. At lower elevations, the oxidation is limited due to the low temperatures and stopped by the relocation of the melt which covers the cladding surface. A comparison of Figure 10 with Figure 12 shows that the measured oxide layers were thicker than those of the calculation, but the tendency matches quite well, if the extremely thick oxide scales of the corner rods in the experiment were neglected.

### **3.2.4 Oxidation behavior of the shroud**

In a standard PWR-specific CORA-bundle the surface of the shroud (ca.  $0.324 \text{ m}^2/\text{m}$ ) contributes with 28% to the whole Zry surface (ca.  $1.2 \text{ m}^2/\text{m}$ ). Assuming double-sided oxidation, this ratio is increased up to 44%, so that the oxidation behavior of the shroud influences the energy balance to a great extent.

The oxidation behavior of the Zry-4 shroud was examined at cross sections of 268, 298, 480, and 870 mm elevations. As shown in Table 3, the lower end of the shroud was located at the 36 mm-elevation, so that there was no Zry shroud at -13 mm.

At 268, 298, and 480 mm only a small part of the shroud remained after removal of the fiber insulation. The remnants of the shroud were completely oxidized, but it was difficult to determine whether the shroud has been oxidized from the

both sides or from the one side, since the remnants were not large enough for a detailed examination.

The oxidation behavior of the shroud at 870 mm shows a double-sided oxidation. The shroud was completely oxidized at about a quarter of the circumference of the shroud, whereas at the other part of the shroud some metal remained. However, the thickness of the  $ZrO_2$  layer on the outer surface was more than ten times as thick as that on the inner surface, as shown in Figure 8.

### 3.2.5 Cladding deformation

At the axial bundle elevations of 268, 298, and 480 mm, most of the claddings were breached and deformed. The breaches occurred at one side, typically at the hot side of the cladding. In the case of the outermost positions of the bundle, the cladding that faced the center of the bundle represents hot side, besides the cladding facing the adjacent heated rod.

Two typical examples showing the edge of the cladding at breach position are given in Figure 13. This type of cladding deformation as shown in the schematic drawings of Figure 13 has been called "flowering" /5/. The thickness of the outer  $ZrO_2$  layer decreased with reaching the edge of the breach. At 298 mm the inner part of the cladding seems to have been oxidized after melting. On the other hand, at 480 mm almost all the material within the outer  $ZrO_2$  layer is lost.

It was observed that molten material, consisting of Zry with uranium and oxygen, penetrated into the outer  $ZrO_2$  layer, as shown in Figure 14. At 480 mm the molten material was oxidized immediately, so that the outflow of the liquid was stopped (left picture). Further it was also found that the cladding was breached 13 mm below (right picture), on the lower side of the sliced sample. Through the transparent epoxy resin it could be seen that both states are linked together as shown in the schematic of Figure 14. So, two typical states of the outflow of molten material can be seen within 13 mm.

At 268, 298, and 480 mm one or two claddings appeared to be intact, as shown in Figure 15. To detect the cladding deformation, the diameters of the intact claddings were measured and the results are given in Table 6. The cladding



shows a circumferential elongation widening the gap between the pellet and the cladding. This elongation may be caused by the high inner rod pressure and/or the volume growth due to the oxidation of the Zry claddings /18/.

The cladding deformation due to the difference between the internal rod pressure and the system pressure has been calculated by the SCDAP code (s. Figure 16). A comparison reveals that the calculated values are smaller than those observed at 268, 298, and 480 mm (Table 6).

The annular pellet used in the heated rods shown in Figure 15 is a good example for the crack formation of these CORA-typical pellets. Three cracks through the whole wall allow a relocation of the fragments after complete failure of the cladding, if no fuel-cladding interaction occurs.

In separate-effect tests to investigate fuel-cladding interaction in the MONA facility, no ballooning occurred because the external pressure was up to 4.0 MPa so that the gap between the pellet and the cladding was closed by the collapse of the cladding onto the  $\text{UO}_2$ -pellets establishing a good solid-state contact /7/,/18/. The enlarged gap in the present experiment must have retarded the  $\text{UO}_2$ /Zry interaction compared with the MONA test where the pellets contacted the cladding.

These results of the observations have to be considered for discussion of the basic mechanisms of cladding deformation.

### **3.3 Results of CORA-5**

#### **3.3.1 Description of the cross sections**

The cross section at 95 mm shows intact claddings with very slight oxidation (s. Figure 17). At the position of the lower blocked zone (at 208 mm), chemical interactions were found between claddings, pellets and relocated melts (s. Figure 18). The claddings were slightly oxidized from the outside. In the middle of the blocked zone (at 393 mm), solidified porous melt blocks some coolant channels (s. Figure 19). The claddings were completely oxidized, consisting of the outer  $\text{ZrO}_2$  layer and the inner oxidized part. The same situation was found at

408 mm, just below the initial position of the Inconel grid spacer (s. Figure 20). The unpolished cross section was analyzed at 663 mm, below the upper Zry grid spacer, showing breached and deformed claddings which were completely oxidized. At the position of the upper Zry grid spacer (at 853 mm) claddings, grid spacer, and pellets must have interacted with each other as well as with absorber material (s. Figure 21). No remaining metallic Zry was detected.

### 3.3.2 End state of the claddings

Figure 22 shows the end state of the claddings, classified as in the case of CORA-2; clad intact, clad missing, clad reacted, and clad flowered. It can be seen that up to 208 mm claddings are intact except for one which had reacted with the melt. Above 393 mm most of the remaining claddings exhibit flowering. At 853 mm, position of the upper Zry grid spacer, about half of the claddings are missing completely.

### 3.3.3 Thickness of oxidized layers of the claddings

In Figure 23 the outer  $ZrO_2$  layer thickness is given for each remaining cladding as a function of the axial elevation. Again it was found that the outer  $ZrO_2$  layer thickness of an individual rod was not uniform at the same elevation. The mean outer  $ZrO_2$  layer thicknesses of each rod were also different from one another, as shown in Figure 23.

Table 5 lists the mean outer  $ZrO_2$  layer thicknesses and their standard deviations at each elevation. No significant difference in the thickness is to be seen between the heated rods and the unheated rods.

Figure 24 shows the mean outer  $ZrO_2$  layer thickness of each fuel rod, together with the various state of the claddings, plotted at the horizontal cross sections of 95, 208, 393, 408, and 853 mm. At 95 mm the thickness of the  $ZrO_2$  layer of the unheated fuel rods was 4~5  $\mu m$  and that of the heated fuel rods was 6~7  $\mu m$ . At this elevation the temperature was below 750 °C and no temperature escalation occurred. Under these conditions the temperature of the heated fuel rods must have been significantly higher than that of the unheated fuel rods.

At 208 mm relocated material blocked one corner of the bundle in the direction of 255°. The thickness of the ZrO<sub>2</sub> layer of the claddings at this corner was large compared with others at this elevation and changed systematically; the thickness decreased with rods in the direction of the opposite corner of the bundle at the orientation of 75°. This systematic change of the thickness may be caused by the relocated material at the corner which transferred the heat to this elevation resulting in an asymmetric radial temperature distribution.

As already pointed out, the cross sections at 393 and 408 mm elevations show the same behavior. Here some parts of the coolant channel were blocked by the relocated material. Outside of the blocked area, the claddings were completely oxidized. The thickness of the ZrO<sub>2</sub> layer of the claddings was influenced by the relocated material which shielded the cladding from the steam.

At 853 mm some claddings were completely lost. The thicknesses of the ZrO<sub>2</sub> layer of the remnants of the claddings were also distributed widely. It should be noted that the thickness of the ZrO<sub>2</sub> layer at this elevation, the position of the upper Zry grid spacer, may have been affected by the reactions of the Zry claddings with the Inconel springs of the grid spacer and with the absorber melt which was caught on the grid spacer.

### 3.3.4 Oxidation behavior of the shroud

The oxidation behavior of the Zry shroud was examined at horizontal cross sections of 95, 208, 393, and 408 mm elevations and at a vertical cross section from 210 to 290 mm. No shroud remained at the horizontal cross section of 853 mm.

It was found that the shroud was oxidized on both sides. At 393 and 408 mm the shroud was oxidized completely, whereas metallic parts remained at other cross sections observed. The thickness of the ZrO<sub>2</sub> layer of the shroud showed axial and circumferential dependency. In almost all cases, the thickness of the ZrO<sub>2</sub> layer and the structure on both the sides were nearly the same, which can be seen in Figure 25 as a representative example.

### 3.3.5 Behavior of the absorber rod

At 95 mm, position of the intact claddings, the ss (stainless steel) cladding of absorber rod was intact. Molten absorber material containing Zr was relocated in the annular gap between the ss cladding and the Zry guide tube. The outer surface of the Zry guide tube was slightly oxidized, as shown in Figure 26(a).

Figure 26(b) shows the behavior of the absorber rod at 208 mm, the position of the lower blocked zone. The ss cladding was also intact, but the Zry guide tube was almost dissolved by molten material. A thin oxide skin kept the molten material from flowing out.

Beyond 300 mm the absorber rod was destroyed completely. Absorber material was spread over the whole bundle, influencing the behavior of the claddings.

## 3.4 Results of CORA-12

### 3.4.1 Description of the cross sections

The first cross section (unpolished), at 51 mm, shows intact claddings with very thin  $ZrO_2$  layers and some solidified metallic material between the claddings. In the center of the blocked zone, at 216 mm, solidified material has blocked some coolant channels interacting with the claddings (s. Figure 27). The remnant of the claddings, except one cladding, was completely oxidized consisting of two parts: outer  $ZrO_2$  layer and inner oxidized part. Above the blocked zone (unpolished), at 381 mm, the claddings were deformed and completely oxidized. Above the middle Zry grid spacer, at 533 mm, most of the claddings were relocated and the remnants were deformed. Dissolution of  $UO_2$  and rubble was found (s. Figure 29). Below the upper Zry grid spacer (unpolished), at 711 mm, most of the claddings were relocated, so that only the remnant of four claddings remained. The remaining claddings were completely oxidized which consist of the outer  $ZrO_2$  layer and the inner oxidized part. Above the upper Zry grid spacer (unpolished), at 876 mm, the same situation was found as at 711 mm.

### 3.4.2 End state of the claddings

In bundle CORA-12 some mechanically broken claddings were observed, which were not found in CORA-2 and CORA-5. Figure 30 shows an end state of the claddings at each elevation, where the state is classified in the five groups. It is characteristic in CORA-12 that at 216 mm about one third of the claddings are broken mechanically and 9 claddings are missing completely. At the upper half of the bundle most of the claddings are missing, which is not seen in CORA-2 and CORA-5 bundles.

### 3.4.3 Thickness of oxidized layers of the claddings

The mean thicknesses of the outer  $ZrO_2$  layer of each remaining fuel rod as a function of the axial elevation are shown in Figure 31. The same tendency was obtained as in CORA-2 and CORA-5; the outer  $ZrO_2$  layer thickness of an individual rod was not uniform at an elevation given, and the mean outer  $ZrO_2$  layer thicknesses of each rod were also different from one another. It is characteristic that the  $ZrO_2$  layer thickness at 216 mm in CORA-12 is large compared with the cases in CORA-2 and CORA-5.

Table 5 lists the mean outer  $ZrO_2$  layer thicknesses and their standard deviations at each elevation. It is found again that no significant difference in the thickness is to be seen between the heated rods and the unheated rods.

Figure 32 shows the mean outer  $ZrO_2$  layer thickness of each fuel rod, together with the various state of the claddings, plotted at the horizontal cross sections of 216, 381, 533, 711, and 876 mm. At 216 mm the claddings were interacted with the relocated melt, oxidized, or lost completely. The number of the rods with completely lost claddings is 9, which is much larger than that at the comparable cross sections in CORA-2 and CORA-5. This can be found at other elevations, too. At 533 mm, for example, the number of the rods whose claddings were completely lost is 16.

#### **3.4.4 Oxidation behavior of the shroud**

To examine the oxidation behavior of the Zry shroud, vertical cross sections from 53 to 201 mm and from 218 to 366 mm were used. No shroud remained at horizontal cross sections of 216 and 533 mm.

On the cross section from 53 to 201 mm, it was found that the shroud was oxidized from both sides. The  $ZrO_2$  layer thickness on the outer surface of the shroud was nearly the same as that on the inner surface, as shown in Figure 33(a). The thickness increased from about 2  $\mu\text{m}$  at 53 mm to 100  $\mu\text{m}$  at 190 mm. Structure of the oxidized layers on the both surfaces was nearly the same.

From 85 to 105 mm in the direction of  $120^\circ$ , relocated melt was found on the outer surface of the shroud, as shown in Figure 33(b). This means that the contact of the shroud with the fiber insulation was not tight during the test, indicating that argon gas with steam could have flowed between the shroud and the insulation.

On the cross section from 218 to 366 mm, most part of the shroud was lost, but the remnant was oxidized completely. At 381, 711, and 876 mm some parts of the shroud remained, which were oxidized completely from both sides.

#### **3.4.5 Behavior of the absorber rods**

Two absorber rods were assembled in bundle CORA-12, but one of them could be examined on the vertical cross section.

Up to about 110 mm the ss cladding and the guide tube kept the melt from flowing out. Figure 34 shows an example at about 100 mm, where the ss cladding is intact containing the absorber melt within it. The relocated melt mainly consisting of absorber material and zirconium is kept between the ss cladding and the guide tube. At around 110 mm the guide tube was breached and the melt flowed downward.

Below 270 mm the relocated melt froze to block some cooling channels. Above 270 mm the absorber rod was completely destroyed, where some part of the reacted and deformed guide tube remained.

## **4. Discussion of the results**

In order to extrapolate the CORA test results towards in-core behavior, it is necessary to clarify the test conditions and test history. Further, the differences between CORA-2 and CORA-5 and between CORA-5 and CORA-12 have to be pointed out.

First of all, the behavior of the CORA-typical heated fuel rods will be discussed in comparison with the unheated ones. Secondly, the sequence of phenomena of each test will be discussed with a special type of diagram containing the measured data and the results of the video inspections. Then the differences between CORA-2 and CORA-5, and the influence of the quenching will be discussed, considering the sequence of phenomena and the test conditions. At last, a mechanism of the cladding deformation will be proposed.

### **4.1 Behavior of heated and unheated fuel rods**

In the CORA experiments two types of fuel rods were used, the PWR-specific "unheated fuel rod" (without heat source) and the electrical heated "heater rod" which heats up the unheated rod, too. Therefore it is very important to be assured that the CORA-typical heated rods behave in the same manner as the unheated rods.

In bundle CORA-2 no significant difference in the cladding end state can be seen between the heated and the unheated rods, except at 480 mm, as shown in Figure 11. At 480 mm all claddings of the unheated rods are missing, whereas the claddings remain in 13 rods out of 16 heated rods. Considering the fact that the claddings remained at the rods of the outermost positions of the bundle, the difference observed at this elevation may be caused by the temperature difference.

In bundles CORA-5 and CORA-12 no significant difference in the cladding end state between the two types of the rods can be recognized (s. Figure 24 and Figure 32).



Table 5 shows that there is no significant difference in the oxidation behavior of the claddings between the heated and unheated rods.

## **4.2 Sequence of phenomena**

In order to establish an order of the phenomena, test sequence with the variables of time and axial bundle elevation were drawn for CORA-2, CORA-5, and CORA-12, which were based on the temperatures measured at the axial bundle elevations of 0, 150, 350, 550, 750 and 950 mm [2], [17], as shown in Figure 35, Figure 36, and Figure 37, respectively.

These temperature front curves, given in the uppermost part of each test sequence diagram, show in the horizontal direction the temperature rise at any axial positions within the bundle, whereas in the vertical direction the axial temperature gradient can be derived for any time between 3000s and 5700s.

Additionally, these diagrams show the cladding failure derived from the inner rod pressure recordings (dotted area), and the summary of the melt relocations observed by the video inspection (dashed area). Below, in the second part the fluid composition at the bundle entrance ( $z=0$  m) is given. The slopes of argon and steam were computed by a separate model which is based on the data of the fluid injected into the steam generator and the volume of the whole system of the CORA facility [17]. Furthermore the electric power input is given. In the lowest part significant phenomena are outlined.

In these diagrams the measured data of the experiments and the results of the video inspection are concentrated, allowing an extraction and an interpretation of the sequence of the phenomena.

### **4.2.1 CORA-2 bundle**

The isothermal diagram for CORA-2 is shown in Figure 35, starting at 3000 s and ending at 5700 s. The first significant event recognized during the experiment was the pressure drop of the fuel rods. The history of the inner pressure of the fuel rods is shown in Figure 38, which indicates that the pressure drop

occurred between 3900 s and 3950 s in all monitored fuel rods. The maximum inner pressure was about 0.9 MPa and the system pressure about 0.22 MPa, indicating a pressure difference of about 0.7 MPa.

Between 3900 s and 3950 s the fuel rod temperatures were below 1200 °C at any axial bundle elevations, as shown in Figure 35. Taking the results of creep rupture tests in steam atmosphere /19/ into consideration, it may be concluded that the mechanical stresses due to the pressure difference caused the rupture of the slightly oxidized cladding in the high temperature zone (about 1100 °C) of the bundle between 600 and 700 mm, which is marked as dotted area in Figure 35. The same result can be derived from the analysis of the pressure drop curves /17/.

Chemical interaction of the Inconel grid spacer with the slightly oxidized Zry-4 cladding at 450-488 mm may be another mechanism leading to a pressure drop due to the perforation of the cladding. But the temperature at the Inconel spacer was not high enough at the time of the pressure drop, so that a remarkable eutectic reaction could not take place /8/. In the lower half of the bundle, at 268 mm and 298 mm, no indication for a cladding rupture below the melting point of Zry-4 (about 1760 °C) could be observed in the metallurgical examination.

After 4000 s the temperatures increased rapidly especially between 500 and 800 mm due to the exothermal steam/Zry reaction, which caused a gradual increase in the H<sub>2</sub> concentration in the off-gas system. The rapid temperature increase at the lower part of the bundle was caused by material relocation.

From the observation of the video tapes, liquefaction of the Inconel spacer and relocation of molten material were recognized, marked as dashed area in Figure 35. The melting point of Inconel is about 1450 °C, but the liquefaction must have occurred below the melting point as a result of eutectic reactions of nickel and iron with zirconium /5/.

According to the metallurgical examination, the inner part of the claddings at 268, 298, and 480 mm was oxidized above the melting point of Zry-4. This fact indicates that the cladding deformation (flowering) occurred not before 4100-4300 s. The structure of the outer ZrO<sub>2</sub> layer derived from the metallurgical examination indicates that it must have been formed below the melting point of  $\alpha$ -Zr(O).

Further, a thin oxidized layer was formed on the Zry-4/ $\text{UO}_2$  reaction product at 870 mm, indicating that steam starvation must have occurred. Since the reaction occurred around melting point of Zry, this oxidation took place after about 4500-4600 s.

At the lowest part of the bundle (-13 mm) the temperature was always below 1000 °C, except for the hot spots caused by the relocated material, leading to a formation of the thin oxidized layers of  $\text{ZrO}_2/\alpha\text{-Zr(O)}$  on the claddings.

#### 4.2.2 CORA-5 bundle

In the same way as for CORA-2, an isothermal diagram, given in Figure 36, was established for CORA-5. It can be recognized that the temperature profile and the melt relocation observed in CORA-5 are quite different from those in CORA-2 shown in Figure 35.

In CORA-5 the drop of the fuel rod pressure occurred between 4100 s and 4150 s, as can be seen in Figure 36. The inner pressure of the rods was about 0.5 MPa and the system pressure was about 0.22 MPa at clad failure, as shown in Figure 39, and the maximum fuel rod temperature at cladding failure was about 1500 °C at around 800 mm.

The failure pressure difference was smaller and the failure temperature was higher in CORA-5 than those in CORA-2. Since the cladding failure occurred before the observation of melt relocation, it may be concluded that the interaction of Zry claddings with the Inconel springs at the upper Zry grid spacer caused the cladding failure /20/.

The melting point of the absorber material, the (Ag,In,Cd) alloy, is about 800 °C /11/, so that the absorber material started melting at about 3700 s between 500 and 800 mm, according to the 800 °C isothermal line in the diagram. As the interaction of the ss cladding with molten absorber material is negligible at all /11/, the molten alloy is kept in the ss cladding until it fails mechanically.

Two mechanisms are likely for the ss cladding failure: one is the melting of ss at about 1450 °C with the Zry guide tube intact, and the other one is the eutectic interaction of ss with the Zry of the guide tube above 1200 °C where the Zry

guide tube fails first (perforation) and the ss cladding ruptures at the position of the interaction due to the high inner rod pressure /11/.

During the temperature escalation due to the exothermal reaction between steam and Zry, melt relocation was observed above 1500 °C. This indicates that the ss cladding failed. Since the absorber material was spread radially as well as axially, the ss cladding may have failed by the latter mechanism, the eutectic interaction of ss with Zry. If the ss cladding melts where the Zry guide tube is intact, the guide tube would keep the low-viscous absorber melt and no spray of the absorber melt should be observed.

According to the metallurgical examination, the absorber rod was completely destroyed above 300 mm elevation. The isothermal diagram shows that the temperature was beyond the melting point of ss (about 1450 °C) above this elevation.

Around 200 mm elevation the maximum temperature was about 1000 °C, which is higher than the melting point of the absorber material, where the Zry guide tube was dissolved by the molten absorber material. On the other hand, 100 mm below, the maximum temperature was lower than the melting point of the absorber material, so that the Zry guide tube was almost intact though it was contacted by the absorber material.

Interaction of the Inconel grid spacer with the Zry claddings and subsequent melting with relocation occurred around 4300 s. Up to this time the spacer acted as obstacle for relocated melt which refroze there.

In the upper part between 400 and 900 mm the maximum temperature was beyond the melting point of  $\alpha$ -Zr(O), so that the claddings were breached, deformed (flowering), and completely oxidized. As mentioned above, the maximum temperature was lower than 1000 °C below 200 mm, where the claddings were oxidized slightly from the outside and most of the claddings were mechanically intact.

#### **4.2.3 CORA-12 bundle**

The isothermal diagram for CORA-12 is shown in Figure 37. It can be seen that in the heat-up and escalation phases the temperature profile and the melt relo-

cation observed in CORA-12 are nearly the same as those in CORA-5. The test CORA-12 was ended by quenching, so that the behavior of the bundle in the cool-down phase was quite different from that of CORA-5.

In CORA-12 the drop of the fuel rod pressure occurred between 4080 s and 4150 s. The inner pressure of the fuel rods and the system pressure at the cladding failure were about 0.35 and 0.22 MPa, respectively. The maximum fuel rod temperature at cladding failure was about 1500 °C between 700 and 800 mm. The pressure difference and the temperature at cladding failure in CORA-12 were nearly the same as those in CORA-5, indicating the same mechanism of the cladding failure, the chemical interaction of the Zry claddings with the Inconel springs at the upper Zry grid spacer.

As discussed in section 4.2.2, the absorber material melted at about 800 °C, kept inside the ss cladding until it failed. The ss claddings reacted with the Zry guide tubes above 1200 °C, resulting in breaches of the Zry guide tubes and the failure of the ss claddings with the spray of the absorber melt. During the temperature escalation, the melt relocation was observed above about 1200 °C.

Above 270 mm the maximum temperature was higher than the melting point of ss (about 1450 °C), resulting in a complete destruction of the absorber rods as observed in the metallurgical examination.

According to the metallurgical examination, the claddings between 381 mm and 876 mm, where the maximum temperature was beyond the melting point of Zry, were breached, deformed (flowering), and completely oxidized. The shroud in this region was also completely oxidized. It can be concluded that the oxidation of the claddings and the shroud in this region was completed at the end of the escalation phase as already observed in test CORA-5. The temperature profiles and the melt relocations observed were nearly the same as those in the test CORA-5.

According to the isothermal diagram, at around 200 mm the maximum temperature was lower than 1000 °C in the escalation phase, which is the same as in the case of the test CORA-5. It can be assumed that at the end of the escalation phase the claddings around 200 mm in CORA-12 were mechanically intact and the metallic part of the cladding remained inside the claddings, since the claddings at around 200 mm in CORA-5 were slightly oxidized and most of them were mechanically intact.

During the quenching, when the bundle was cooled down by rising water from the bottom of the bundle,  $H_2$  concentration in the off-gas system increased sharply, as shown in Figure 37, indicating rapid oxidation. The temperatures, for example at 1250 mm, also increased sharply, as shown in Figure 40.

The claddings, which were brittle due to the oxidation, were cracked by thermal shock and vibration of the rods due to the reflood. The metallic part of the remaining claddings at around 200 mm was exposed to steam, resulting in rapid oxidation and the temperature increase. The additional oxidation during quenching can be seen at around 200 mm in the axial profile of the oxide layer thickness, comparing with the case of CORA-5 as shown in Figure 41.

The claddings above 1000 mm, which must have been oxidized only slightly before the quenching, were oxidized rapidly by high temperature steam and the temperature was escalated. The copper electrode used above 1.25 m may have melted (the melting point of Cu is 1083 °C) and relocated downward. Melt relocations were observed in the upper part of the bundle by video inspections in the cool-down phase. The relocated melt was also observed at the cross sections of 711 and 876 mm by metallurgical examination.

The rapid oxidation and the temperature escalation were stopped by the rising water level of the quench tank.

### **4.3 Influence of test conditions**

The final states of all bundles, described in section 3, are different from each other. The influence of the different test conditions such as initial and boundary conditions as well as the test termination on the final state will be discussed in the following section.

#### **4.3.1 Initial and boundary conditions**

A comparison of the final states of CORA-2 and CORA-5 is given Figure 42, which shows areas of horizontal cross sections . /14/ together with the end state of the claddings observed metallurgically in the present examination. The

differences between CORA-2 and CORA-5, given in Figure 42, with respect to the oxidation of the claddings and the axial material distribution will be discussed in the following.

In CORA-2, local steam starvation occurred at the elevation around the upper Zry grid spacer and the molten Zry/ $\text{UO}_2$  reaction product contributed to the damage progression of the bundle. Below the Inconel grid spacer, Inconel/Zry interaction mainly dominated to the damage progression in this region.

On the other hand, in CORA-5, no steam starvation occurred. The absorber material, spread over the whole bundle, mainly contributed to the damage progression. The range of intact cladding was larger in CORA-5 than in CORA-2, which resulted from the differences in the axial temperature profile.

To investigate the differences in the bundle end state mentioned above, the test conditions and the damage scenarios were compared. In Figure 43, the different initial and boundary conditions are listed on the left side, together with their interactions during the test up to the end.

#### **Inner rod pressure**

Generally, the cladding failure mechanisms are governed by the internal fuel rod pressure and the system pressure. If the internal pressure is high enough compared to the system pressure, the cladding balloons and ruptures. The rupture time depends on the total pressure difference and the thickness of the oxide scales. If the pressure difference is reversed, a collapse of the cladding onto the fuel pellets occurs enhancing the dissolution of the fuel.

In CORA-2 the claddings ballooned and ruptured mechanically, whereas in CORA-5 the claddings failed by chemical interaction, as already discussed in section 4.2. The ballooning of the cladding causes a reduction of the effective coolant channel causing an orifice-like cross section which then influences the flow pattern of the fluid. Due to the increase in friction, a part of the fluid tends to bypass the coolant channel (through the observation holes and flow in the annulus between the shroud and the HTS).

#### **Absorber rod**

The absorber rod represents a source of low-melting oxidation resistant material which is spread over the bundle. As shown in Figure 35 and Figure 36, the

melt relocations observed in CORA-2 and in CORA-5 started at different axial elevations. In CORA-2 melt relocation was observed only below the Inconel grid spacer ( $z < 0.5$  m), whereas in CORA-5 it was observed below  $z \sim 0.9$  m.

The first relocation phenomena observed in CORA-5 were droplets of absorber material at 4150 s as shown in Figure 36. Though the original absorber rod cannot be seen directly by the video cameras (Figure 2), the droplets must have been sprayed over several rows of rods due to the high internal pressure within the absorber rod.

#### **Observation holes (windows)**

As described in section 2, observation windows were open in CORA-2 and closed by quartz glass in CORA-5. In the case the windows are open, argon gas can flow out of the bundle into the annulus. This bypass flow influences the axial temperature profile of the bundle. If the bypass ratio is enlarged, i.e. reduction of the coolant channel cross section, the flow is split into the channel flow ( $\gtrsim 70$  %) and a bypass flow ( $\lesssim 30$  %). Therefore, the heat transfer in the bundle is reduced allowing a faster heat up because the heat transfer to the fluid is reduced. Argon flow rate also influences the axial temperature profile since cooling capacity is also dependent on the argon flow rate.

#### **Fluid composition**

As can be seen in Figure 35 and Figure 36, the temperature of the lower part of the bundle in CORA-2 was higher than that in CORA-5. The highest temperature region was around 600 mm in CORA-2 and around 700 mm in CORA-5. The difference in the temperature profile between CORA-2 and CORA-5 may be caused by the effects of the bypass flow and the different argon flow rates.

The different bundle end states observed are mainly caused by the different test conditions: the high inner rod pressure in CORA-2, the large observation holes in CORA-2, and the absorber rod in CORA-5.

### **4.3.2 Influence of quenching**

Axial temperature profile and melt relocations observed in test CORA-12 before the cool-down phase were nearly the same as those in test CORA-5. It is adequate to compare the two tests to discuss the influence of the quenching.



During quenching rapid increase of  $H_2$  concentration in the off-gas and the temperature escalation were observed, as shown in Figure 37 and Figure 40, respectively, indicating a rapid exothermal steam/Zry reaction.

In order to clarify which parts of Zry were oxidized during the quenching, the oxidation profiles of tests CORA-5 and CORA-12 are compared (s. Figure 41). In CORA-5 below 200 mm the claddings were intact and were oxidized slightly with the metallic parts inside the cladding. Above 400 mm the claddings were breached, deformed (flowering), and completely oxidized (s. Figure 42, bottom). In CORA-12 even at 216 mm the claddings were oxidized completely, except for a small part of the cladding at one corner of the bundle. The thickness of the outer oxide layer at 216 mm in CORA-12 is much larger than that at 208 mm in CORA-5. The thicknesses of the outer oxide layer at other elevations, except for the highest position, are nearly the same between those in CORA-12 and CORA-5, as shown in Figure 41.

It should be noted again that in CORA-5 at 853 mm elevation the thickness of the outer oxide layer may have been affected by the reactions of the Zry claddings with the Inconel springs of the grid spacer and with the absorber melt which was caught by the grid spacer. The position of 876 mm in CORA-12 was above the upper Zry grid spacer.

Assuming the bundle end state of CORA-5 as an intermediate bundle state of CORA-12 just before the quenching, it can be concluded that the additional oxidation took place at around 200 mm where the metallic parts of the claddings remained. This assumption does not stand apart from the real state, because the temperature profile and the melt relocations observed are nearly the same between tests CORA-5 and CORA-12.

Comparing the end state of the claddings in CORA-12 (Figure 30) with that in CORA-5 (Figure 22), it can be seen that in CORA-5 below 400 mm all claddings remained, whereas in CORA-12 some of the claddings were completely lost. For the fuel pellets, Nagase /14/ examined the axial profiles of the remnants of the pellets, which are shown in Figure 44. It can be seen again that in CORA-5 below 400 mm most of the pellets remained, while in CORA-12 some of the pellets were lost. These facts indicate that during quenching the claddings, which were brittle due to the oxidation, were broken mechanically, resulting in the exposure of the metallic parts of the claddings to steam together with the frag-

mentation of the pellets. These fresh metallic surfaces were oxidized immediately, so the oxidation region was extended axially to lower elevations.

It cannot be excluded that due to the high temperatures above 1.0 m additional hydrogen could have been produced, but this is outside the heated zone of the bundle and cannot be checked further because no cross sections are available.

#### **4.4 Mechanisms of cladding deformation**

So far two different types of mechanisms leading to cladding deformations were found in the high temperature region of the three analyzed bundles.

##### **4.4.1 Deformation due to high inner rod pressure**

At temperatures below 1100°C a high inner rod pressure leads to ballooning with subsequent rupture of the cladding. This process starts with a slight circumferential elongation over nearly the whole length of the rod, widening the gap between pellet and cladding. Then the cladding balloons in the hot region of the rod until it ruptures due to mechanical stress at the hottest azimuthal position. This rupture releases the fill-gas of the rod so that the pressure curves (s. Figure 38) show a sudden drop down to the system pressure. The ballooning, which is already well understood /19/, /24/, was observed in test CORA-2 and dominates the early failure of the claddings.

This mechanical deformation, however, cannot lead to such strong deformations of the claddings which were observed in all three tests, because the cladding cross section remains quite cylindrical and no flattening occurs.

##### **4.4.2 Deformation due to chemical interactions**

A mechanism to explain the observed flattening of the cylindrical claddings is the chemical interaction between the inner still metallic surface of the zircaloy cladding and steam.

### **Oxidation of the inner surface**

One possible mechanism is based on the double sided oxidation of the claddings below the melting temperature of  $\beta$ -zircaloy /5/. When the cladding ruptures due to a high inner rod pressure and the fill gas has pured out, steam can diffuse through the breach. The subsequent oxidation of the inner metallic surface of the cladding leads to  $\alpha$ -Zr(O) and  $ZrO_2$  which creates compressive stresses. These stresses were reduced by a bending of the cladding which increases the size of the breach. A larger breach allows a better access of the steam, so that the oxidation continues until the whole inner surface is oxidized /6/.

### **Oxidation of molten zircaloy**

To explain the cladding deformations found in the metallurgical observation of this report another mechanism will be proposed. The mechanism is divided into six steps, which are given in the schematic representation of Figure 45. An annular gap of about  $50\mu\text{m}$  between the  $UO_2$  pellets and the Zry-4 cladding is assumed for starting conditions (*step 1*). The model will not distinguish between heated and unheated rods because they have the same dimension of the annular gap between pellet and cladding.

At elevated temperatures in steam atmosphere, the Zry-4 cladding is oxidized from the outside only as long as the cladding is intact. Then reaction layers of  $ZrO_2$  and  $\alpha$ -Zr(O) are formed (*step 2*), causing a volume increase due to the oxidation of the Zry-4. This creates a tensile stress at the outer surface of the oxidized cladding and a compressive stress at the inner surface of the oxidized layer.

When the temperature rises up to the melting point of Zry-4 (about  $1760^\circ\text{C}$ ), the inner still metallic part of the cladding melts. Assuming a circumferential temperature variation, the Zry-4 melts at the hot spot first. Then the gap between fuel and cladding is filled with liquid Zry (*step 3*).

The liquid metal reacts with the oxidized cladding reducing the layer thickness locally, since the diffusivity of oxygen in the just molten Zry is several times larger than that in  $ZrO_2$  /21/. In this step it is not necessary to assume steam starvation /21/. Some part of the  $UO_2$  is also dissolved by the liquid metal (*step 4*). Both dissolution processes increase the oxygen concentration of the melt so that the melting temperature rises too.

The locally thinned oxidized layer ruptures due to the mechanical stresses in the oxidized layer. Some parts of the liquid metal flow out forming voids (*step 5*) (e.g. Figures 3(b), 20(a),(b)). The breach of the cladding allows steam to contact locally the inner metallic surface of the cladding. Oxidation of the inner metallic part and the mechanical stresses created in the outer oxidized layer lead to cladding deformation, called "flowering" (*step 6*).

*Step 6* shows the final state of the flowering. This type of deformation is observed as shown in Figure 13(a). In the extreme case, i.e. at high temperature when the viscosity of the liquid is very low, almost all inner metallic melt flows out at *step 5*. A typical representation of this state can be seen in Figure 13(b).

As already pointed out, a circumferential temperature variation causes the flowering above the melting point of  $\alpha$ -Zr(O). In power plants the flowering would occur, if the cladding temperature varies circumferentially. Actually, some claddings flowered probably by such a mechanism were observed in in-pile tests /22/, /23/.

## 5. Summary

With the present study the series of post-test investigations focussed on a global description of the tests CORA-2, CORA-5, and CORA-12 is complete.

Main interests of the present study are the interpretation of the oxidation behavior of the Zry-4 claddings and the shroud, as well as the explanation of the high-temperature cladding deformations observed in all CORA tests. Therefore, cross sections of the three CORA bundles were examined with optical microscope. To explain the different bundle end states, a sequence of phenomena was created for each test, so that a temporal and axial location can be given for each phenomenon observed. Taking into account these sequences of phenomena, the discussion of the results of the metallurgical examination leads to the following conclusions:

- The thickness of the  $ZrO_2$  layer formed on the outer surface of a Zry-4 cladding is dependent on not only the axial elevation but also on the circumferential positions. Moreover, the mean layer thickness also varies from one rod to another with a standard deviation of about 20 % at an axial elevation given.
- The sequence of the phenomena for CORA-2, CORA-5, and CORA-12 could be explained using special test sequence diagrams which compiles all informations available during test. With these diagrams the differences between CORA-2 and CORA-5 as well as between CORA-5 and CORA-12 were qualified and their influences on the bundle end state were estimated.
- The differences in the bundle end state between CORA-2 and CORA-5 were mainly caused by the effect of the absorber rod, thermohydraulic boundary conditions, and the design of the observation holes (windows). Therefore, the most dominant mechanisms of damage progression of the bundle were different, too. In CORA-2, besides the Zry/Inconel interaction, molten Zry/ $UO_2$  interaction around the upper zircaloy grid spacer contributed to the damage progression. In CORA-5, absorber materials were spread over the whole bundle initiating the damage progression of the fuel rods.

- The differences in the bundle end state between CORA-5 and CORA-12 were discussed in terms of the influence of quenching. The number of the rods with completely lost claddings in CORA-12 was much larger than that in CORA-5, where the test was ended without quenching. The axial distribution of the thickness of the outer  $ZrO_2$  layer showed that additional oxidation took place around 200 mm and above 1000 mm elevations during quenching.
- The mechanisms of the cladding deformation were discussed. To explain the deformations ("flowering") observed in all analyzed tests a new model was proposed. According to this model, the flowering occurs above the melting point of Zry-4 under a circumferential temperature distribution. At the hottest position the outer oxidized layer is thinned locally by the liquid metal from the inside, ruptures due to mechanical stresses and deforms due to oxidation of metallic liquid.

With the combination of the measured data compiled in the test sequence diagrams and those of the post-test investigation a global interpretation of the CORA experiments can be carried out. This interpretation can qualify the influence of single effects such as ballooning, rupture and deformation of the cladding on the global bundle behavior. Since the "flowering" influences the energy release due to an increase of cladding surface single effect tests are necessary to quantify this additional release.

## **Appendix A. Acknowledgements**

The authors gratefully thank Mr. L. Sepold for his review of this paper and Mr. G. Schanz for his fruitful discussions concerning the interpretation of the observed phenomena. Furthermore the authors appreciate the support by Dr. B. Kuczera and Dr. P. Hofmann, Projekt Nukleare Sicherheitsforschung, and Dr. H. Rininsland, head of the Hauptabteilung Ingenieurtechnik.

## Appendix B. References

- /1/ S. Hagen and K. Hain, Out-of-pile Bundle Experiments on Severe Fuel Damage (CORA-Program), Objectives, Test Matrix and Facility Description, KfK 3677 (1986).
- /2/ S. Hagen, L. Sepold, P. Hofmann and G. Schanz, Out-of-pile Experiments on LWR Severe Fuel Damage Behavior, Tests CORA-C and CORA-2, KfK 4404 (1988).
- /3/ S. Hagen and P. Hofmann, Nucl. Eng. Des. 103 (1987) 85.
- /4/ S. Hagen, P. Hofmann, G. Schanz and L. Sepold, Kerntechnik 53 (1988) 15.
- /5/ S. Hagen, P. Hofmann, G. Schanz and L. Sepold, Interaction in Zry/UO<sub>2</sub> Fuel Rod Bundles with Inconel Spacers at Temperatures above 1200 °C (Posttest Results of Severe Fuel Damage Experiments CORA-2 and CORA-3), KfK 4378 (1990).
- /6/ Sicherheitsorientierte LWR-Forschung, Jahresbericht 1988, KfK 4550 (1989).
- /7/ P. Hofmann and D. Kerwin-Peck, J. Nucl. Mater. 124 (1984) 80.
- /8/ P. Hofmann, S. Hagen, G. Schanz and A. Skokan, Nucl. Technol. 87 (1989) 146.
- /9/ H. Uetsuka and P. Hofmann, J. Nucl. Mater. 168 (1989) 47.
- /10/ P. Hofmann, M. Markiewicz and J. Spino, Reaction Behavior of B<sub>4</sub>C Absorber Material with Stainless Steel and Zircaloy in Severe LWR Accidents, KfK 4598 (1989).
- /11/ P. Hofmann and M. Markiewicz, Chemical Behavior of (Ag,In,Cd) Absorber Rods in Severe LWR Accidents, KfK 4670 (1990).
- /12/ W. Hering and R. Meyder, Kerntechnik 53 (1988) 21.



- /13/ W. Hering, Analytical Evaluation of CORA-Experiments using an extended SCDAP version, Heat Transfer and Fuel Behavior in Nuclear Accidents: 26th ASME/AIChE/ANS National Heat Transfer Conference, Philadelphia, PA, USA, August 6-9, 1989, New York: AIChE, 1989 - S.141 (AIChE Symposium Series: Vol. 85 ; 269)
- /14/ F. Nagase, unpublished report (1989).
- /15/ F. Nagase and W. Hering, unpublished report (1988).
- /16/ P. Hofmann, Private communication (1990).
- /17/ W. Hering, Interpretation und Modellierung des CORA-Experiments mit dem erweiterten Kernschmelz-Code SCDAP/MOD1, Dissertation, IKE, to be presented (1991).
- /18/ P. Hofmann, H. J. Neitzel and E. A. Garcia, Chemical Interactions of Zircaloy-4 Tubing with UO<sub>2</sub> Fuel and Oxygen at Temperatures between 900 and 2000 °C (Experiments and PECLOX Code), KfK 4422 (1988).
- /19/ S. Leistikow and G. Schanz, The Oxidation Behaviour of Zircaloy-4 in Steam between 600 and 1500 °C, Werkstoffe und Korrosion 36 (1985) 105.
- /20/ K. Müller, W. Hering, A. Schatz, Verifikation des KESS-III Codes anhand des Out-of-pile Experiments CORA-2, IKE 2-91 (1991).
- /21/ D. R. Olander, J. Nucl. Mater. 119 (1983) 245.
- /22/ PHEBUS - FP- Program, Report IPSN Nr. 3.87 (1987).
- /23/ R. R. Hobbins, G. D. McPherson, A Summary of Results from the LOFT LP-FP-2 Test and Their Relationship to other Studies at the Power Burst Facility and the Three Mile Island Unit 2 Accident, OECD/LOFT Final Event, 9.-11.5. 1990, Madrid.
- /24/ E. H. Karb, M. Prößmann, L. Sepold, P. Hofmann, G. Schanz: LWR Fuel Rod Behaviour in the FR2 In-pile Tests Simulating the Heatup of a LOCA, KfK 3346 (1983).

## Appendix C. Detailed description of the cross sections

### CORA-2

---

#### 1. *At -13 mm: Position of the lower Zry grid spacer*

The claddings were oxidized very slightly from the outside only. Reaction layers of  $ZrO_2/\alpha-Zr(O)$  were observed. The thickness of  $ZrO_2$  was about  $5 \mu m$  and that of  $\alpha-Zr(O)$  was about  $4 \mu m$ . Interaction of Zry claddings with  $UO_2$  pellets was not observed at the inner surface of the claddings. At some positions, molten material was relocated from the upper part of the bundle which refroze on the Zry grid spacer.

#### 2. *At 268 mm: Top of the blocked zone (solid melt)*

Relocated molten material mainly consisting of (U,Zr,O) /5/ refroze in the center of the bundle and blocked the inner cooling channels, as shown in Figure 3. It does not appear that the relocated material is porous, and it contains only a few cracks.

At the unblocked area most of the claddings were breached and deformed. The claddings were completely oxidized, consisting of two parts. One is a columnar structured outer  $ZrO_2$  layer, which was formed by oxidation of the cladding from the outside below the melting point of  $\alpha-Zr(O)$ . The other part is an inner part of  $ZrO_2$  (and (U,Zr) $O_2$ ), which was formed by oxidation of molten Zry.

At the blocked area, the claddings were not completely oxidized. The relocated molten material must have shielded the cladding from being exposed to steam. The inner parts of the claddings remained mainly metallic. Interaction of claddings and  $UO_2$  pellets with the relocated material was observed at some parts of the blocked area.

#### 3. *At 298 mm: Just above the blocked zone (rubble)*

Most of the claddings were breached and deformed. The claddings of the analyzed rods were completely oxidized. The oxidation behavior was the same as that of the unblocked area at 268 mm: the outer  $ZrO_2$  layer, formed from the outside below the melting point of  $\alpha-Zr(O)$ , and the inner part, due to the steam access above the melting point of Zry-4.

No relocated molten material was observed. But rubble, which had formed during the cool-down phase, accumulated in the space between the claddings, as shown in Figure 4. A drastic change in material relocation behavior, from the relocated molten material at 268 mm to the rubble at 298 mm, has been observed.

**4. At 480 mm: Position of the Inconel grid spacer**

No part of the Inconel grid spacer remained. It must have completely relocated due to liquefaction during the escalation phase between 4000 and 4300s.

The claddings at the central part of the bundle were almost lost. At the outermost rod positions facing the shroud, the claddings were completely oxidized. Most of them were breached and deformed.

Figure 5 shows typical examples of oxidized claddings at 480 mm. In the case of Figure 5(a), only outer  $ZrO_2$  layer remained, where the  $\alpha$ -Zr(O) as well as an unoxidized part appears to have melted and flowed downward leaving behind the outer  $ZrO_2$  layer. In Figure 5(b) a small amount of the inner oxidized part remained. It appears that first the inner unoxidized part melted and relocated. Then the residual  $\alpha$ -Zr(O) layer was oxidized from the both sides. This indicates that the temperatures must have been different between the two cases when the cladding failed.

**5. At 870 mm: Position of the upper Zry grid spacer**

Oxidation behavior of Zry at this elevation was quite different from that already observed at 268, 298, and 480 mm. Here two different regions could be distinguished: central region and corner region. In the central region most of the claddings and the grid spacer reacted with  $UO_2$  pellets and some of the pellets were completely relocated in solid state, as shown in Figure 6. It can be concluded that the reaction occurred around the melting point of  $\beta$ -Zry. A thin oxidized layer was formed on the claddings and the grid spacer after the reaction, which can be seen in Figure 6.

In the corner region the claddings of the rods were oxidized to a great extent from the outside, but only at positions facing the shroud. The thickness of the  $ZrO_2$  layer changed circumferentially, as can be seen in Figure 7(a). Here the Zry grid spacer remained between the fuel rod and the shroud. The surface of the grid spacer, facing the fuel rod, was oxidized

remarkably compared with the other surface facing to the shroud, as shown in Figure 7(b). One reason may be that fluid with steam must have flowed between the fuel rod and the grid spacer.

Figure 8 shows the oxidation behavior of the shroud. At about three quarters of the circumference of the shroud from 165° to 360° and from 0° to 75°, the thickness of the ZrO<sub>2</sub> layer of the outer surface of the shroud was more than ten times as thick as that of the inner surface. This indicates that coolant of argon containing steam flowed mainly outside of the shroud. This may be a reason why most of the claddings were oxidized only slightly at this elevation. On the other hand, the shroud was completely oxidized at the rest of its circumference.

To explain this, a closer look at the shroud configuration is necessary. At each corner, the shroud had windows for the video cameras at each 100 mm step, as shown in the schematic of Figure 8. At the azimuthal angle of 120° the shroud had four windows at 200, 400, 600, and 800 mm elevations. The strange oxidation behavior at this elevation may be caused by a diversion of the fluid at lower elevations. The steam content of the fluid in the coolant channel was reduced due to the Zr/steam reaction in the hot center of the bundle. The fluid in the annulus passes the hot center without consumption of steam, so that enough steam is available in the highest part of the heated zone.

## **CORA-5**

---

### **1. At 95 mm: Position of the intact claddings**

The claddings analyzed were oxidized very slightly from the outside forming reaction layers of ZrO<sub>2</sub>/α-Zr(O), as shown in Figure 17(a). The thickness of the ZrO<sub>2</sub> layer was 4~5 μm on the unheated rods and 6~7 μm on the heated rods. The claddings were mechanically intact and not deformed. No interaction was observed between the pellets and the claddings. A small amount of relocated metallic material was observed on the outer surface of the claddings, as shown in Figure 17(b). The ZrO<sub>2</sub> layer of the cladding protected the Zry cladding from an interaction with relocated molten metallic material.

### **2. At 208 mm: Position of the lower blocked zone**

The claddings were slightly oxidized from the outside. In some fuel rods molten material had relocated into the gap between the cladding and the pellet, and interacted with Zry and  $\text{UO}_2$ , as can be seen in Figure 18(a). Some parts of the fuel rod surface were attacked by relocated metallic material from the outside, and an oxide layer was formed on the relocated melts, as shown in Figure 18(b). Although some claddings were attacked from the outside, they were not breached and remained mechanically intact.

**3. At 393 mm: Position of the middle blocked zone**

Some coolant channels were blocked by relocated material which shows a lot of pores due to shrinking effect of melts within an already solidified matrix. In general, however, flowering occurred and the claddings were oxidized completely. The cladding consisted of the outer  $\text{ZrO}_2$  layer and the inner oxidized part, as shown in Figure 19. Such an oxidation behavior was observed at bundle CORA-2, too. Some inner metallic parts melted and flowed downward forming voids between  $\text{ZrO}_2$  and  $\text{UO}_2$ .

**4. At 408 mm: Below the Inconel grid spacer**

The same situation as at 393 mm was found at 408 mm. Refrozen porous material blocked some coolant channels, and the claddings were oxidized completely and consisted of two parts, outer  $\text{ZrO}_2$  and inner oxidized part, as shown in Figure 20. Figure 20(b) indicates that the thickness of the outer  $\text{ZrO}_2$  layer was not uniform on the circumference and that the cladding was breached and deformed (flowering). The thickness of the cladding decreased with reaching the edge of the breach where only the inner oxidized part remained.

**5. At 663 mm: Below the upper Zry grid spacer (unpolished)**

The remaining claddings were breached and deformed (flowering) and were oxidized completely. The oxidized claddings consisted of the two parts, the same as described above. One third of the claddings were missing completely.

**6. At 853 mm: Position of the upper Zry grid spacer**

The claddings were breached and some parts of claddings, grid spacer, and pellets were relocated. The remnants of the claddings and the grid spacers were oxidized completely. It appears that the claddings, grid spacer, and

pellets interacted with one another as well as with absorber material, as shown in Figure 21. No remaining metallic Zry has been detected.

## **CORA-12**

---

### **1. At 51 mm: Above the Inconel grid spacer (unpolished)**

All claddings were intact. It was very difficult to measure the ZrO<sub>2</sub> layer thickness of the claddings and the shroud, since the sample was not polished and the layer was very thin. The ZrO<sub>2</sub> layer thickness obtained at some claddings was 2-4 μm. A small amount of relocated material, which appeared metallic, refroze between the claddings.

### **2. At 216 mm: Center of the blocked zone**

Relocated material blocked some coolant channels. The claddings at the blocked area interacted with relocated melt, as shown in Figure 27(a). The oxidized layer was formed around the melt. Most of the claddings at the other area were broken and lost at this elevation. The claddings appeared to be mechanically broken, as shown in Figure 27(b). This phenomenon is different from the cladding deformation (flowering) observed in the CORA-2 and CORA-5 bundles. The remnant of the claddings, except one cladding of the corner rod in the direction of 165°, revealed that the claddings were oxidized completely and that they consisted of two parts: outer ZrO<sub>2</sub> layer and inner oxidized part, as shown in Figure 28(a). Some inner part flowed downward leaving a void. The inner metallic part of the cladding remained only in the corner rod in the direction of 165°, as shown in Figure 28(b).

### **3. At 381 mm: Above the blocked zone (unpolished)**

The flowering occurred and the claddings were oxidized completely. The oxidized claddings consisted of the outer ZrO<sub>2</sub> layer and the inner oxidized part. No metallic part of the claddings remained. A small part of the shroud remained, which was oxidized completely.

### **4. At 533 mm: Above the middle Zry grid spacer**

Most of the claddings were lost at this elevation. Parts of the cladding remained only at the outermost position of the bundle. Flowering occurred and the claddings were oxidized completely consisting of two parts, as mentioned above. Some UO<sub>2</sub> pellets interacted with the relocated melt resulting in a loss of UO<sub>2</sub>, as shown in Figure 29(a). Although only a small

amount of relocated melt was observed at this elevation, rubble, which mainly consisted of  $\text{UO}_2$ , accumulated at the center of the bundle cross section. A typical example is shown in Figure 29(b).

5. ***At 711 mm: Below the upper Zry grid spacer (unpolished)***

Most of the claddings were lost at this elevation. Only the remnant of four claddings remained. The flowering occurred and the claddings were completely oxidized, consisting of an outer  $\text{ZrO}_2$  layer and an inner oxidized part. In the case of the unheated rods, most of the pellets were lost as well as the claddings. A small amount of relocated material, which appeared metallic, is found between pellets and claddings of the heated rods.

6. ***At 876 mm: Above the upper Zry grid spacer (unpolished)***

The appearance observed at this elevation is similar to that at 711 mm. Most of the claddings were lost, and the remaining claddings were oxidized completely. The oxidized claddings consisted of the two parts as described at 711 mm. Two claddings were mechanically intact and the others were breached and deformed (flowering). A small amount of probably metallic relocated material was observed mainly between pellets and claddings of the heated rods. The remnant of the shroud was completely oxidized.

## Appendix D. Tables

<b>CORA TEST MATRIX (status: Januar 1991)</b>				
<b>Test Nr.</b>	<b>Max. Cladding Temp.</b>	<b>Absorber Material</b>	<b>Other Test Conditions</b>	<b>Date of Test</b>
2	~2000°C	---	<i>UO<sub>2</sub>-Reference Test, Inconel Spacer</i>	06.08.1987
3	~2400°C	---	UO <sub>2</sub> -High Temp., Inconel Spacer	03.12.1987
5	~2000°C	Ag,In,Cd (1)	<i>PWR Absorber Rod</i>	26.02.1988
12	~2000°C	Ag,In,Cd (2)	<i>Quenching, Zry Spacer</i>	09.06.1988
16	~2000°C	B <sub>4</sub> C (1)	BWR Absorber, Reference	24.11.1988
15	~2000°C	Ag,In,Cd (2)	High Fuel Rod Pressure	02.03.1989
17	~2000°C	B <sub>4</sub> C (1)	BWR, Quenching	29.06.1989
9	~2000°C	Ag,In,Cd (2)	High System Pressure ~1.0 MPa	09.11.1989
7	<2000°C	Ag,In,Cd (5)	57 Rod Bundle, predef. Test-Stop	22.02.1990
18	<2000°C	B <sub>4</sub> C (1)	59 Rod Bundle predef. Test-Stop	21.06.1990
13	~2000°C	Ag,In,Cd (2)	ISP-31, Quenching at very high Temperatures (s. CORA-12)	15.11.1990
29	~2000°C	Ag,In,Cd (2)	PWR specific Pre-Oxidation	in 1991
31	~2000°C	B <sub>4</sub> C (1)	Slow Heat-up ~0.3 K/s	in 1991

**Table 1. CORA Test Matrix I:** experiments performed so far and further tests up to 1991

Standard test conditions: initial heat-up rate ca. 1.0 K/s, Argon mass flux: 8 g/s, Steam mass flux: PWR: 6.0 g/s, BWR: 2.0 g/s, Quench rate (from bottom) ca. 0.01 m/s



Further Tests (are planned to be performed in test facility CORA-II)				
Test Nr.	Max. Cladding Temp.	Absorber Material	Other Test Conditions	Date of Test
28	~2000°C	B <sub>4</sub> C (1)	BWR specific Pre-Oxidation	> 1992
30	~2000°C	Ag,In,Cd (2)	slow Heat-up ~0.3 K/s	> 1992
10	~2400°C	Ag,In,Cd (2)	H <sub>2</sub> O-Level in the lower part of the bundle	
27	~2400°C	B <sub>4</sub> C (1)	H <sub>2</sub> O-Level in the lower part of the bundle	
25	~2000°C	B <sub>4</sub> C (1)	System Pressure ~1.0 MPa	
26	~2000°C	B <sub>4</sub> C (1)	fast Heat-up, Quenching	
24	~2000°C	B <sub>4</sub> C (1)	Steam-rich, Quenching	
32	~2000°C	Ag,In,Cd (2)	Quenching from the top	

**Table 2. CORA Test Matrix II:** further tests in the replaced facility (CORA-II)  
 Standard test conditions: initial heat-up rate ca. 1.0 K/s, Argon mass flux: 8 g/s, Steam mass flux: PWR: 6.0 g/s, BWR: 2.0 g/s, Quench rate (from bottom) ca. 0.01 m/s

		<b>CORA-2</b>	<b>CORA-5</b>	<b>CORA-12</b>
<b>Rod</b>	heated: unheated: absorber:	16 9 0	16 8 1	16 7 2
<b>Pellet (UO<sub>2</sub>)</b>	heated: outer diam.: inner diam.: unheated: outer diam.:	annular 9.1 mm 6.1 mm solid 9.1 mm	annular 9.1 mm 6.1 mm solid 9.1 mm	annular 9.1 mm 6.1 mm solid 9.1 mm
<b>Cladding (Zry-4)</b>	outer diam.: thick.: length:	10.75 mm 0.725 mm 2175 mm	10.75 mm 0.725 mm 2175 mm	10.75 mm 0.725 mm 2175 mm
<b>Heater (W)</b>	diam.: length:	6 mm 1000 mm	6 mm 1000 mm	6 mm 1000 mm
<b>Grid spacer</b>	lower: elevation*: middle: elevation*: upper: elevation*:	Zry-4 -47 - -5 mm Inconel-718: 450 - 488 mm Zry-4: 838 - 880 mm	Zry-4 -47 - -5 mm Inconel-718: 458 - 496 mm Zry-4: 838 - 880 mm	Inconel-718: -43 - -5 mm Zry-4 446 - 488 mm Zry-4 838 - 880 mm
<b>Shroud (Zry-4)</b>	wall thick.: outside: elevation*:	1.2 mm 86 x 86 mm 36 - 1241 mm	1.2 mm 86 x 86 mm 36 - 1260 mm	1.2 mm 86 x 86 mm 36 - 1234 mm
<b>Insulator (ZrO<sub>2</sub> fiber)</b>	thickness: elevation*:	20 mm 36 - 1000 mm	20 mm 36 - 1000 mm	20 mm 36 - 1000 mm
<b>Windows</b>	position: area: quartz glass:	corner 15 cm <sup>2</sup> no (open)	side 6 cm <sup>2</sup> yes (closed)	side 6 cm <sup>2</sup> no (open)

**Table 3. Characteristics of bundles CORA-2, CORA-5, and CORA-12:** elevation\* means axial bundle elevation from the bottom of the heated zone.

<b>cross section</b>	<b>CORA-2</b>	<b>CORA-5</b>	<b>CORA-12</b>
<b>1:</b>	<b>-13 mm</b> Position of the lower Zry grid spacer	<b>95 mm</b> Position of the intact claddings	<b>51 mm</b> Above the Inconel grid spacer (unpolished)
<b>2:</b>	<b>268 mm</b> Top of the blocked zone	<b>208 mm</b> Position of the lower blocked zone	<b>216 mm</b> Position of the blocked zone
<b>3:</b>	<b>298 mm</b> Just above the blocked zone	<b>393 mm</b> Position of the middle blocked zone	<b>381 mm</b> Above the blocked zone (unpolished)
<b>4:</b>	<b>480 mm</b> Position of the Inconel grid spacer	<b>408 mm</b> Below the Inconel grid spacer	<b>533 mm</b> Above the middle Zry grid spacer
<b>5:</b>	<b>870 mm</b> Position of the upper Zry grid spacer	<b>663 mm</b> Below the upper Zry grid spacer (unpolished)	<b>711 mm</b> Below the upper Zry grid spacer (unpolished)
<b>6:</b>	—	<b>853 mm</b> Position of the upper Zry grid spacer	<b>876 mm</b> Above the upper Zry grid spacer (unpolished)

**Table 4. List of the analyzed cross sections: elevation and global description**

Test	Elevation (mm)	Heated rods ( $\mu\text{m}$ )	Unheated rods ( $\mu\text{m}$ )	Total ( $\mu\text{m}$ )	Total Min. Med. Max. ( $\mu\text{m}$ )
CORA-2	268	476 $\pm$ 84	442 $\pm$ 117	465 $\pm$ 95	240, 490, 560
	298	465 $\pm$ 85	466 $\pm$ 67	468 $\pm$ 79	240, 490, 590
	480	506 $\pm$ 46	--	506 $\pm$ 46	420, 520, 590
	870	52 $\pm$ 36	62 $\pm$ 50	54 $\pm$ 40	20, 50, 160
	870 <sup>x</sup>	870 $\pm$ 100	660 <sup>a</sup>	635 $\pm$ 126	660, 880, 940
CORA-5	95	6.6 $\pm$ 0.5	4.9 $\pm$ 0.6	6 $\pm$ 1	4, 6, 7
	208	52 $\pm$ 29	57 $\pm$ 29	54 $\pm$ 28	20, 45, 114
	393	342 $\pm$ 82	284 $\pm$ 84	323 $\pm$ 86	190, 330, 470
	408	311 $\pm$ 66	307 $\pm$ 77	309 $\pm$ 68	150, 300, 440
	663	419 $\pm$ 44	440 $\pm$ 24	424 $\pm$ 40	330, 420, 470
	853	199 $\pm$ 34	203 $\pm$ 82	200 $\pm$ 57	140, 190, 350
CORA-12	216	477 $\pm$ 50	590 <sup>a</sup>	491 $\pm$ 88	400, 470, 660
	381	400 $\pm$ 64	366 $\pm$ 51	389 $\pm$ 63	260, 420, 490
	533	390 $\pm$ 46	--	390 $\pm$ 46	330, 380, 470
	711	498 $\pm$ 43	--	498 $\pm$ 43	470, 480, 560
	876	527 $\pm$ 65	590 <sup>a</sup>	539 $\pm$ 60	420, 540, 610

**Table 5. Cladding outer oxide layer thicknesses:** average value with standard deviation for the remnants of the claddings.

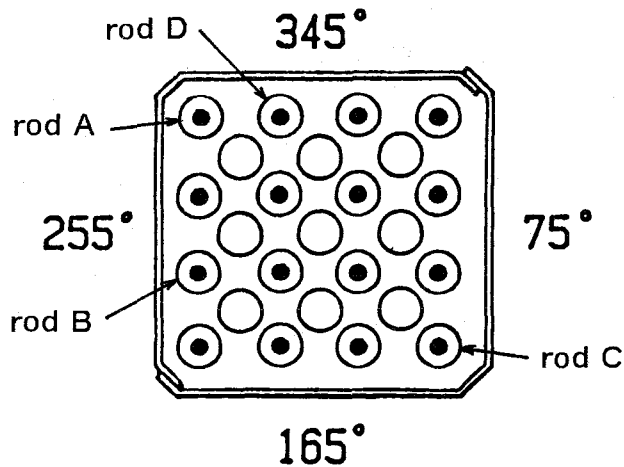
The statistical values are calculated for the heater rods (2. column), the unheated rods (3. column), and all rods analyzed (4. column) at the elevation given (1. column). Further, the minimum (Min.), the median (Med.), and the maximum (Max.) values are shown (last column).

<sup>x</sup>indicates the group of corner rods (CORA-2, 870 mm)

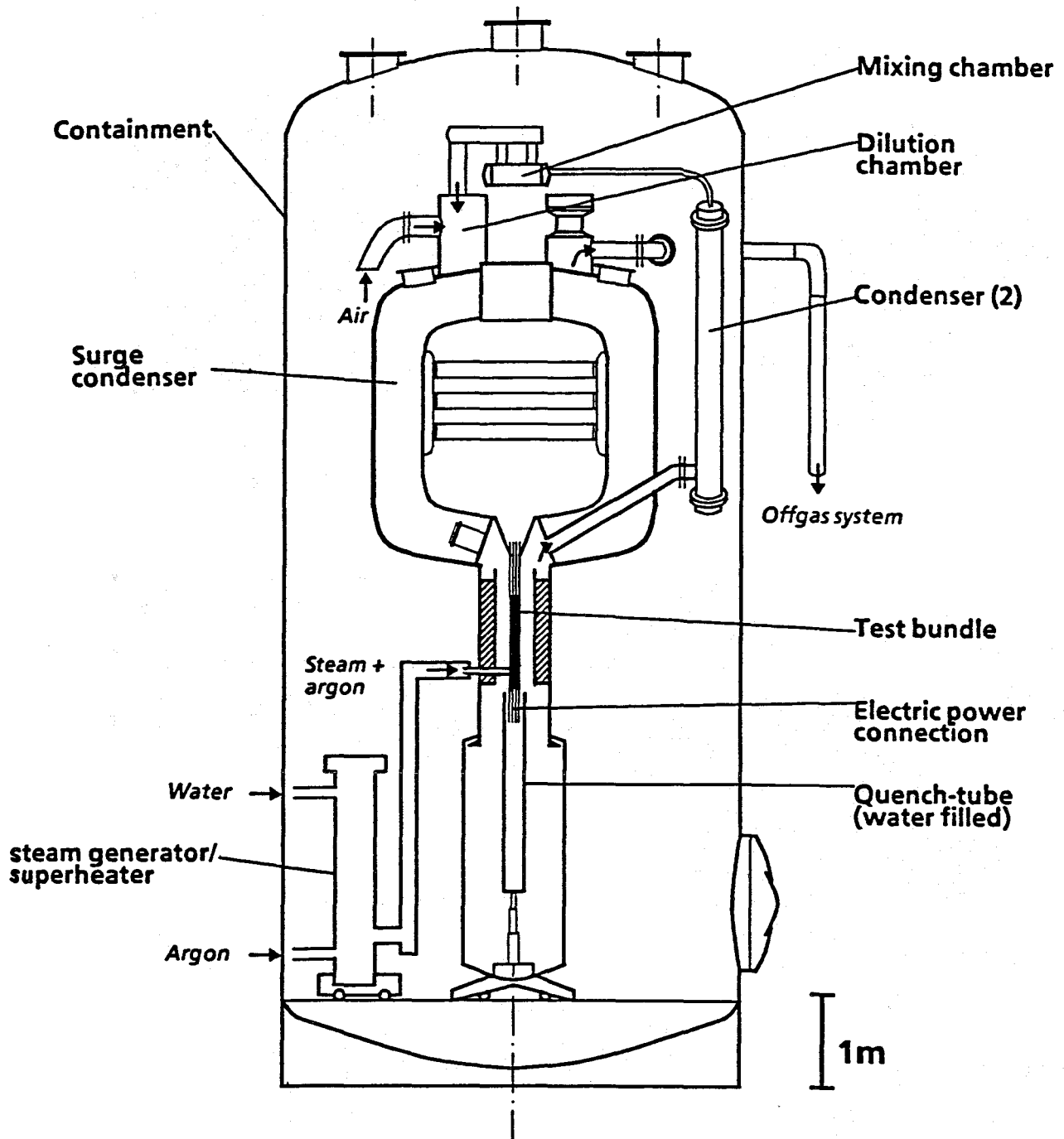
<sup>a</sup> only one rod with remnant cladding

Position within the bundle <sup>x</sup>	Outer diameter of the claddings (min.-max.) (mm)	Circumferential elongation measured (%)	Circumferential elongation calculated by SCDAP (%)
initial value	10.75	Ref.	Ref.
at -13 mm	no significant change	-	< 1
at 268 mm rod A	11.3 - 12.5	5 - 16	ca. 2
rod B	11.5 - 12.0	7 - 12	
at 298 mm rod B	11.5 - 12.0	7 - 12	ca. 3
rod C	11.3 - 12.3	5 - 14	
at 480 mm rod D	11.5 - 12.3	7 - 14	ca. 5
at 870 mm	no intact cladding	-	ca. 3

Table 6. Outer diameter of the intact claddings of CORA-2: comparison between experiment and calculation (position within the bundle<sup>x</sup> is indicated below).



## Appendix E. Figures



KfK

**Figure 1. Schematic overview of the CORA facility:** including the most important features such as test section with the test bundle, steam generator/superheater, and quench device.

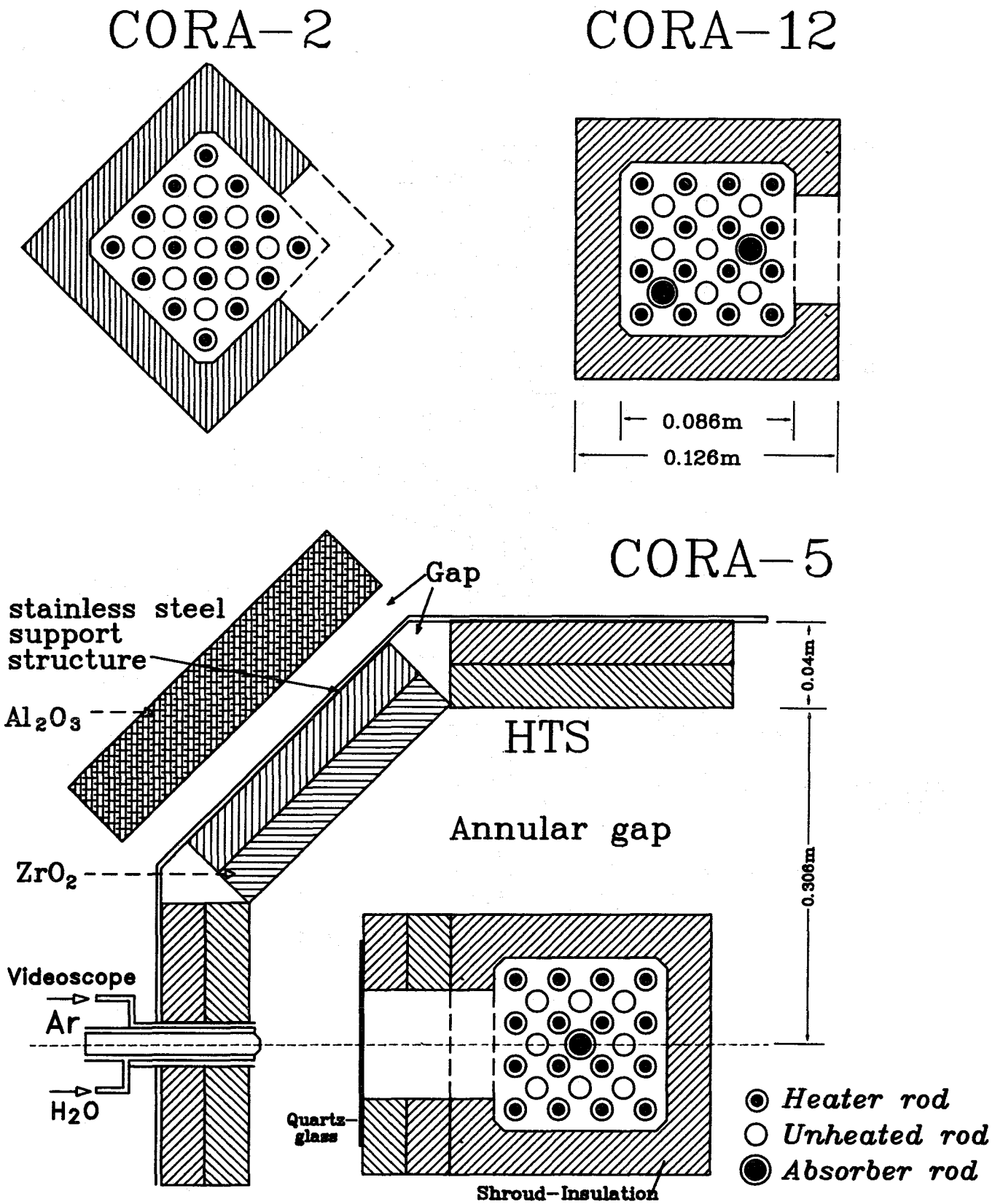
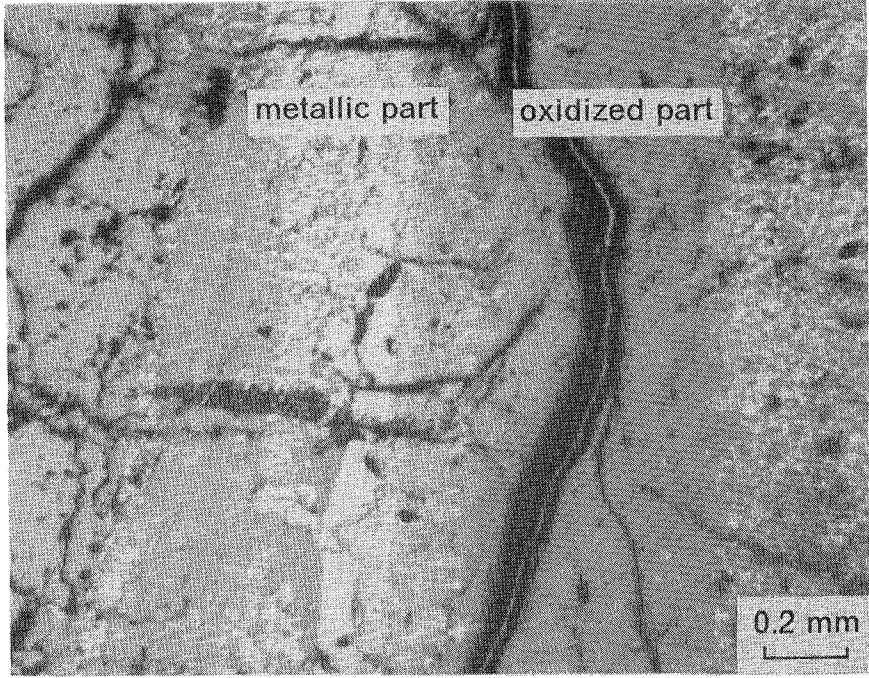
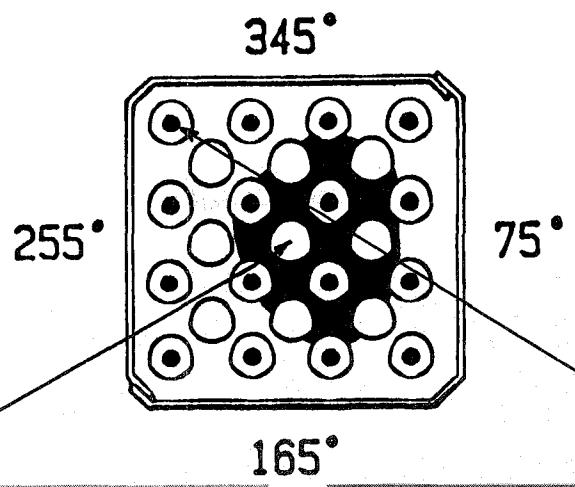
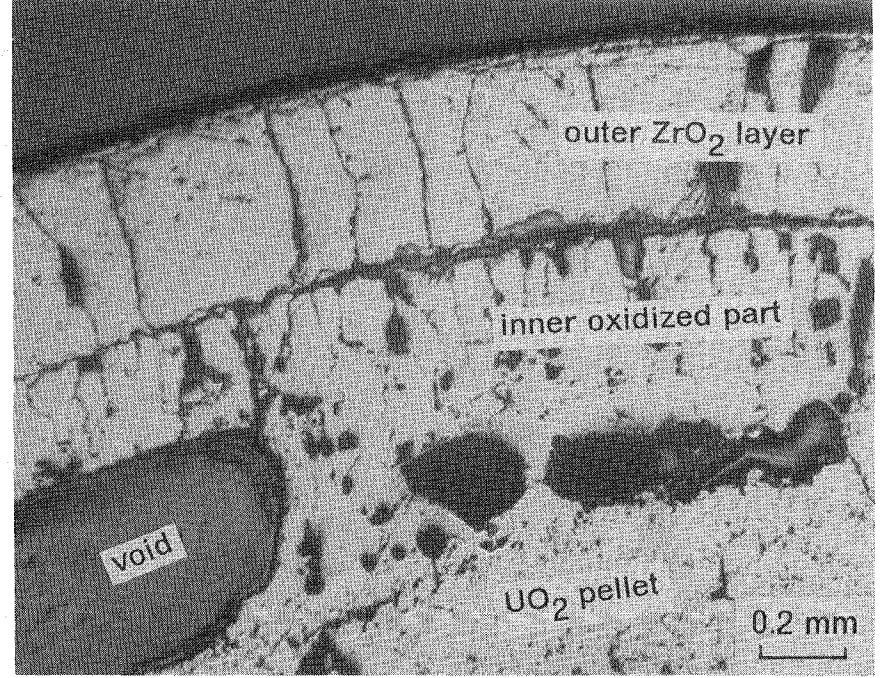


Figure 2. Arrangements of the bundles: top: CORA-2 and CORA-12 bundle, bottom: CORA-5 bundle within the high temperature shield

at 268 mm



(a)



(b)



**Figure 3. CORA-2, fuel rods at 268 mm elevation:** (a) remaining metallic part in the middle of the cladding in the blocked region; (b) complete oxidation of the cladding in the unblocked region



**at 298 mm**

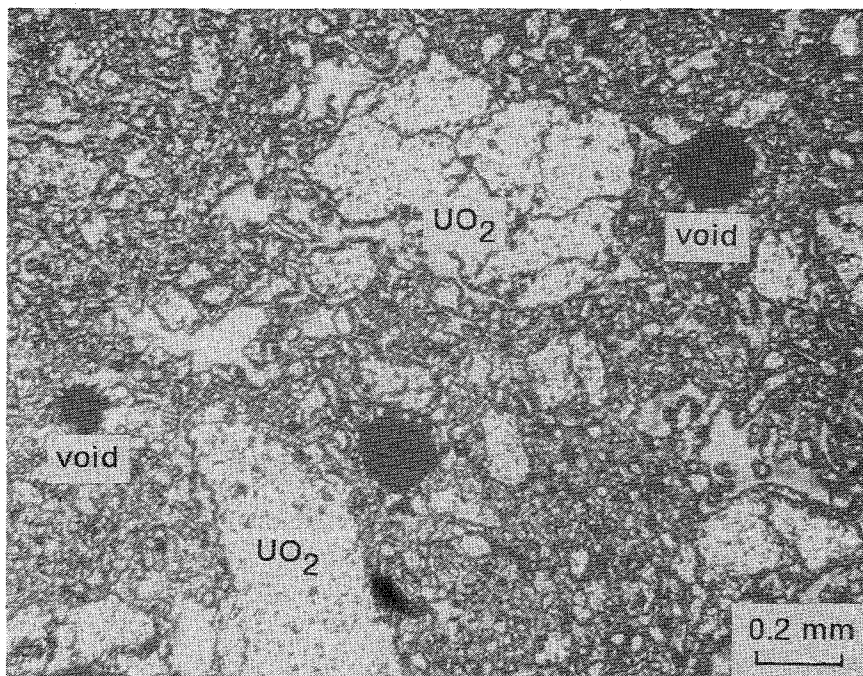
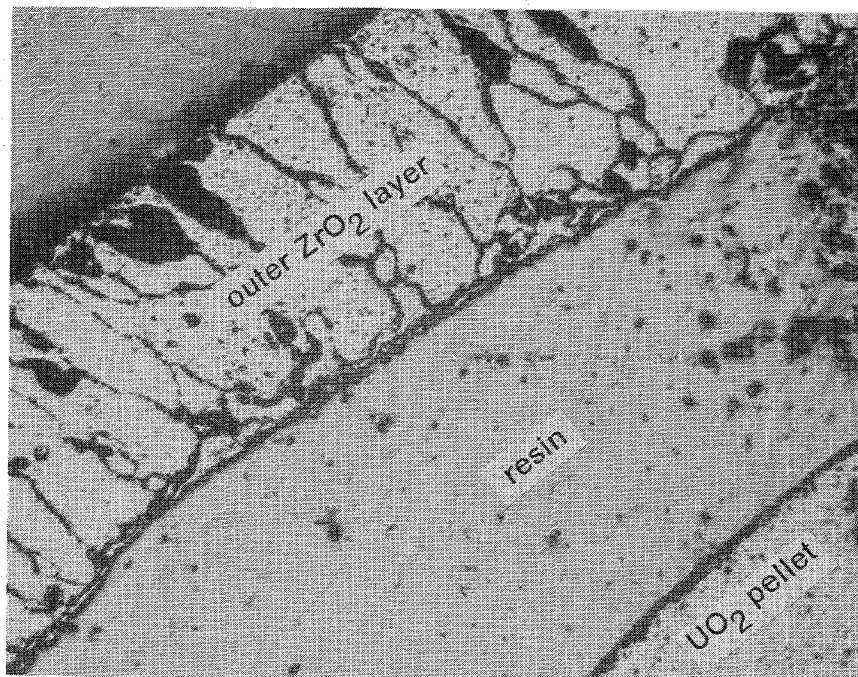
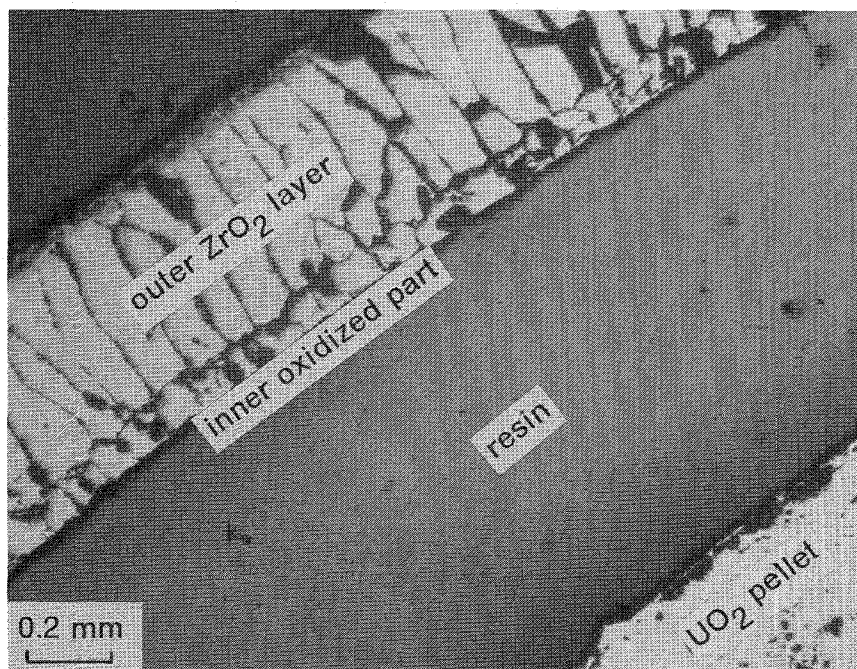


**Figure 4. CORA-2, rubble at 298 mm elevation: on top of the blocked region**

at 480 mm



(a)

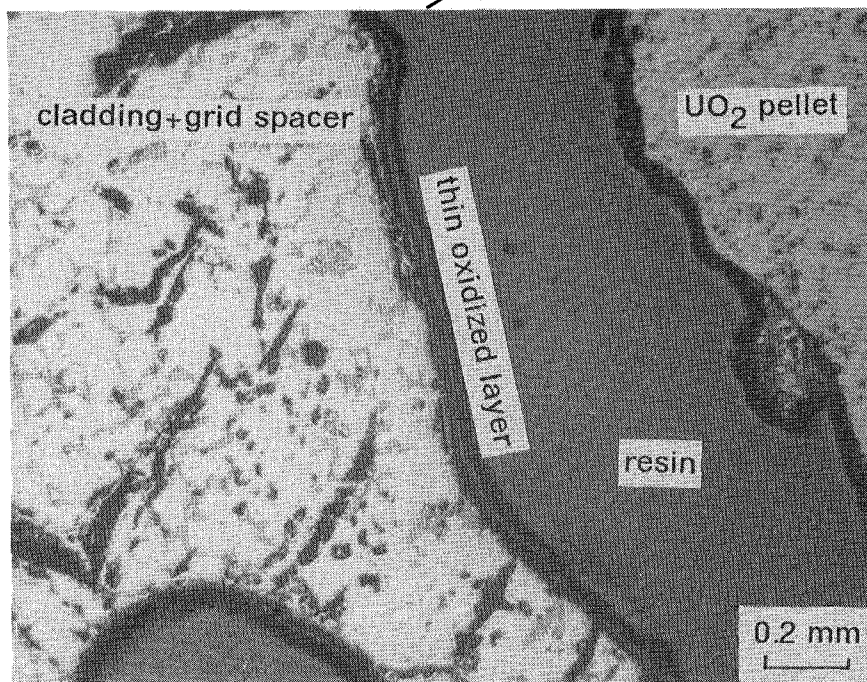
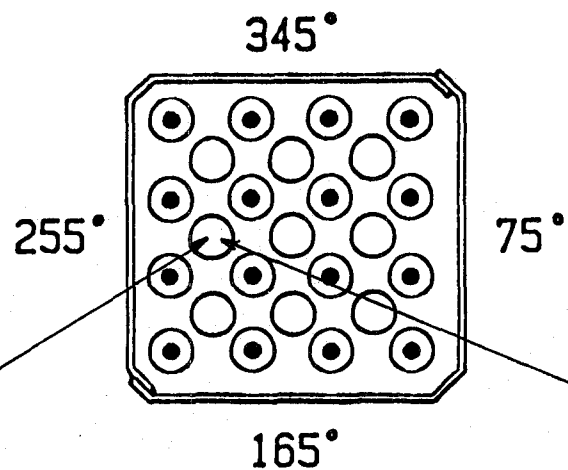


(b)

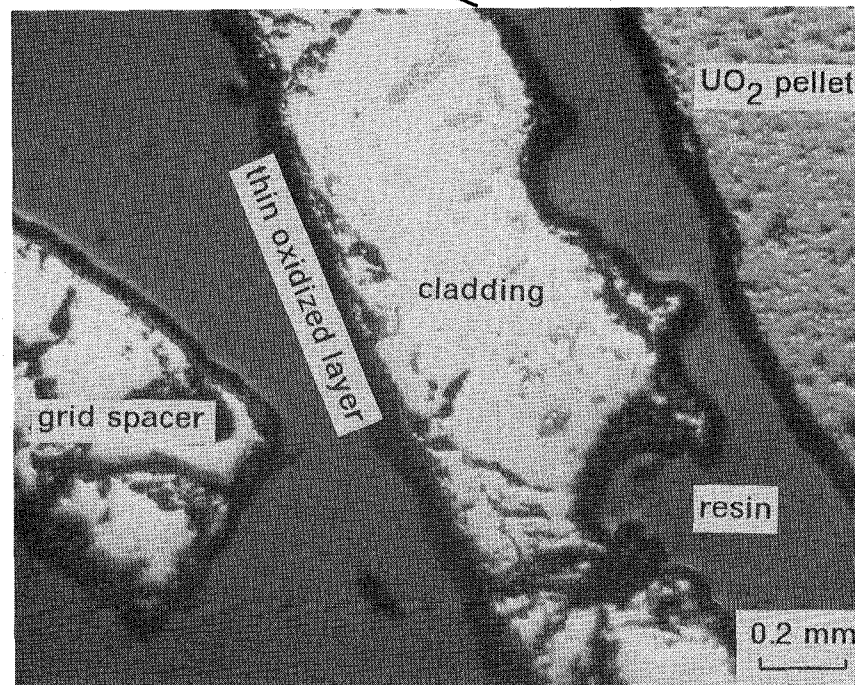
KJK

**Figure 5. CORA-2, fuel rods at 480 mm elevation:** (a) cladding without inner oxidized part; (b) cladding with a thin inner oxidized part. Both types show a large gap between cladding and pellet.

at 870 mm



(a)



(b)



**Figure 6. CORA-2, fuel rods at 870 mm elevation:** (a) a thin oxidized layer on cladding/Zry-spacer/ $\text{UO}_2$  reaction product; (b) a thin oxidized layer on cladding/ $\text{UO}_2$  and Zry-spacer/ $\text{UO}_2$  reaction products.



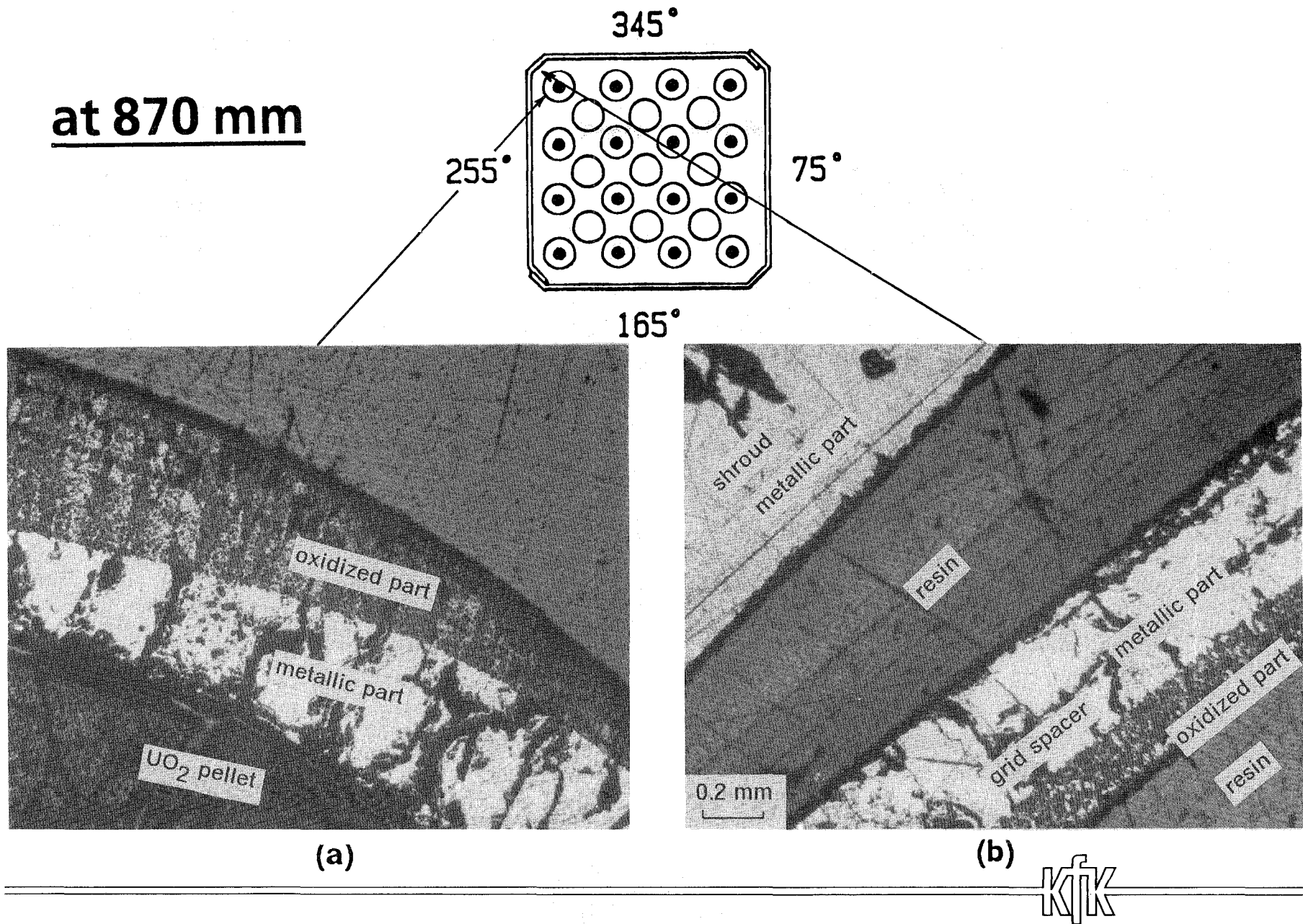
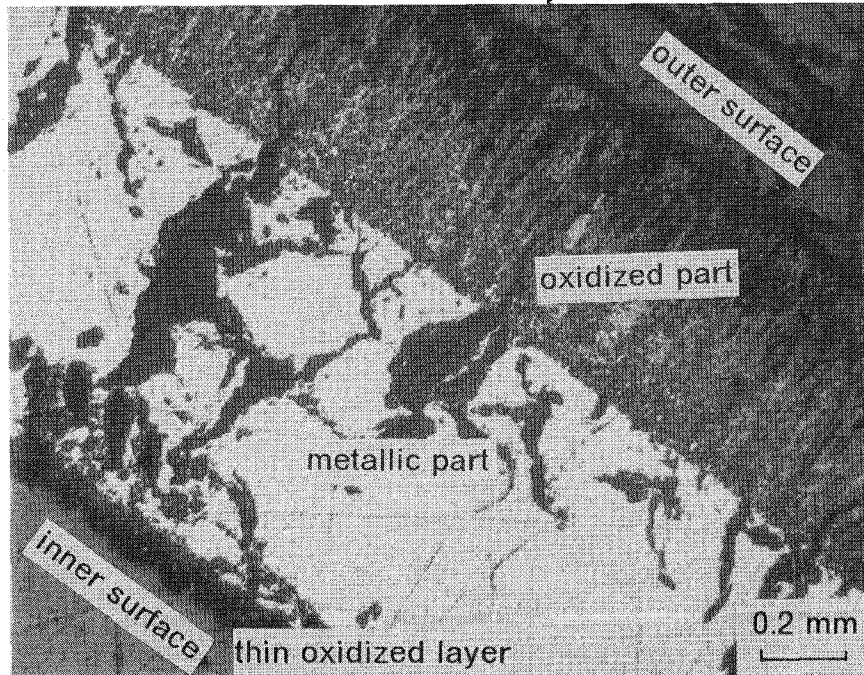
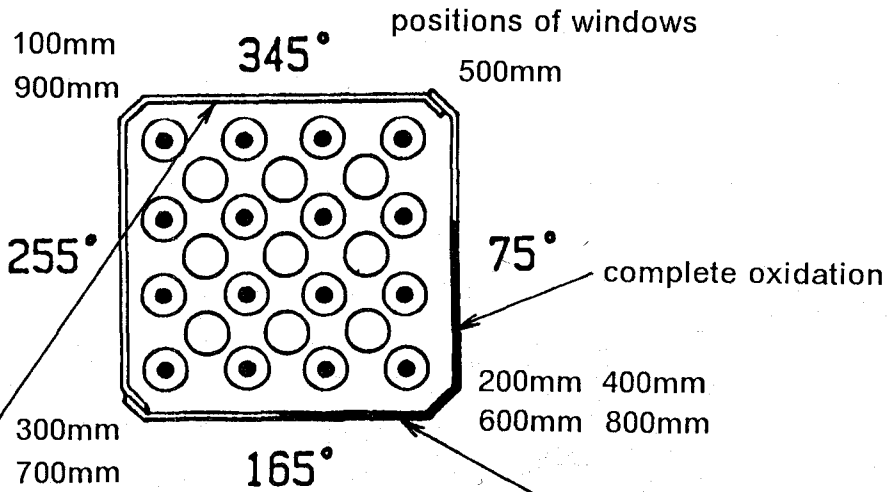
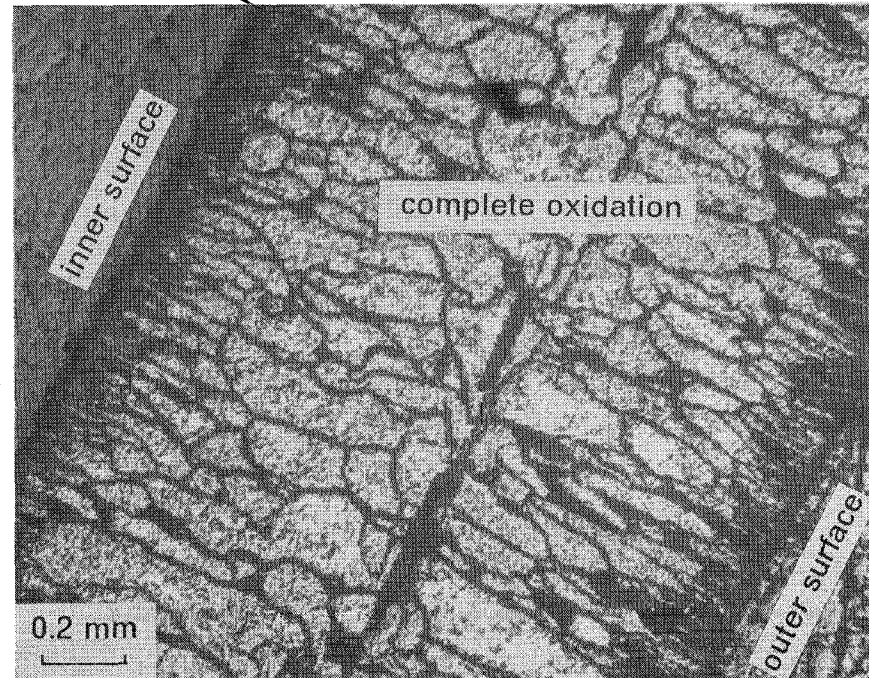


**Figure 7. CORA-2, fuel rod, spacer and shroud at 870 mm elevation:** (a) azimuthal variation of the oxidized layer thickness of the cladding; (b) thick oxidized layer on the inner surface of the spacer facing to the heated rod at corner position.

at 870 mm



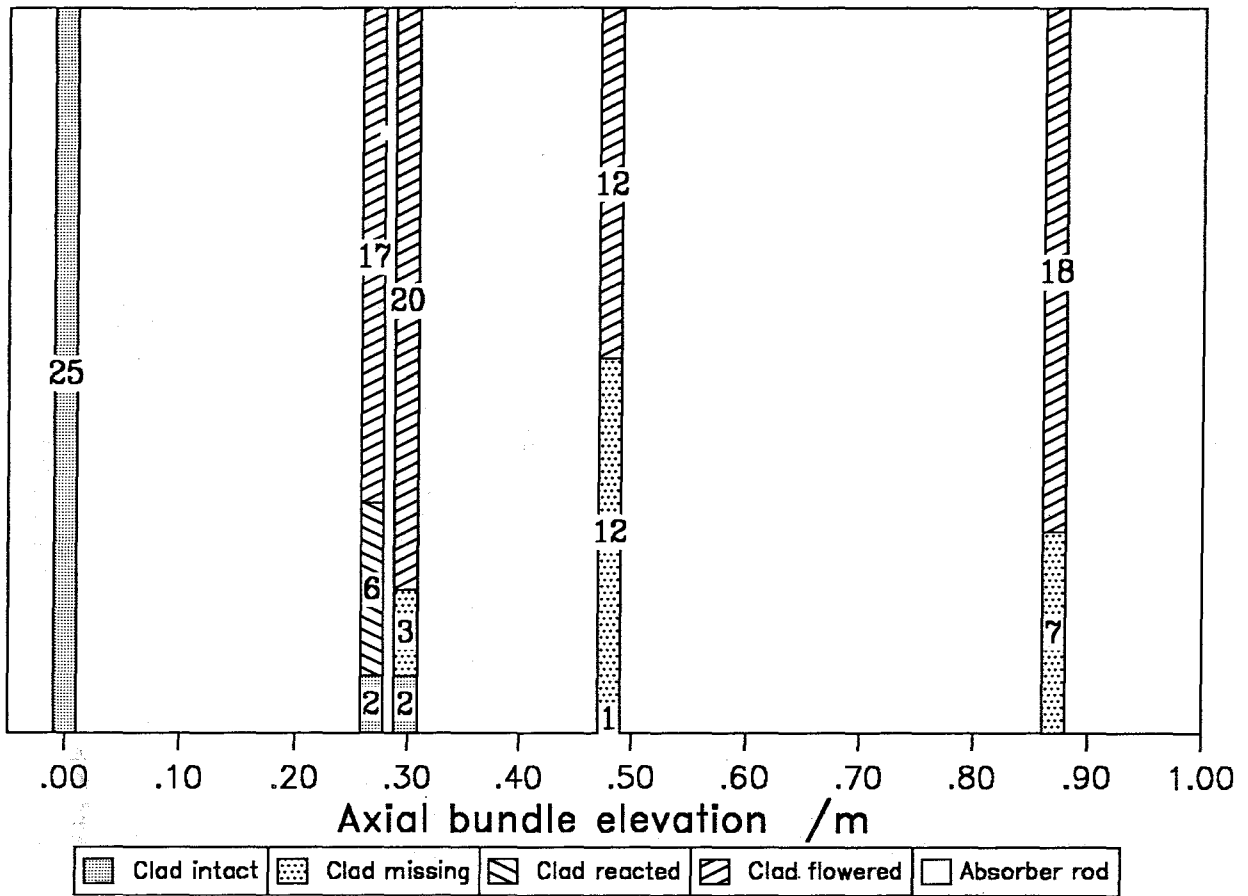
(a)



(b)



**Figure 8. CORA-2, shroud at 870 mm elevation:** (a) thicker oxidized layer formed on the outer surface than on the inner surface; (b) complete oxidation from the both sides with the same oxide structure.



CORA-2 Elevation /mm	Cladding intact	Cladding missing	Cladding reacted	Cladding flowered	Absorber rod
-13	25	0	0	0	0
268	2	0	6	17	0
298	2	3	0	20	0
480	1	12	0	12	0
870	0	7	0	18	0

**Figure 9. CORA-2, end state of the claddings:** claddings are classified as intact, missing, reacted, and flowered.

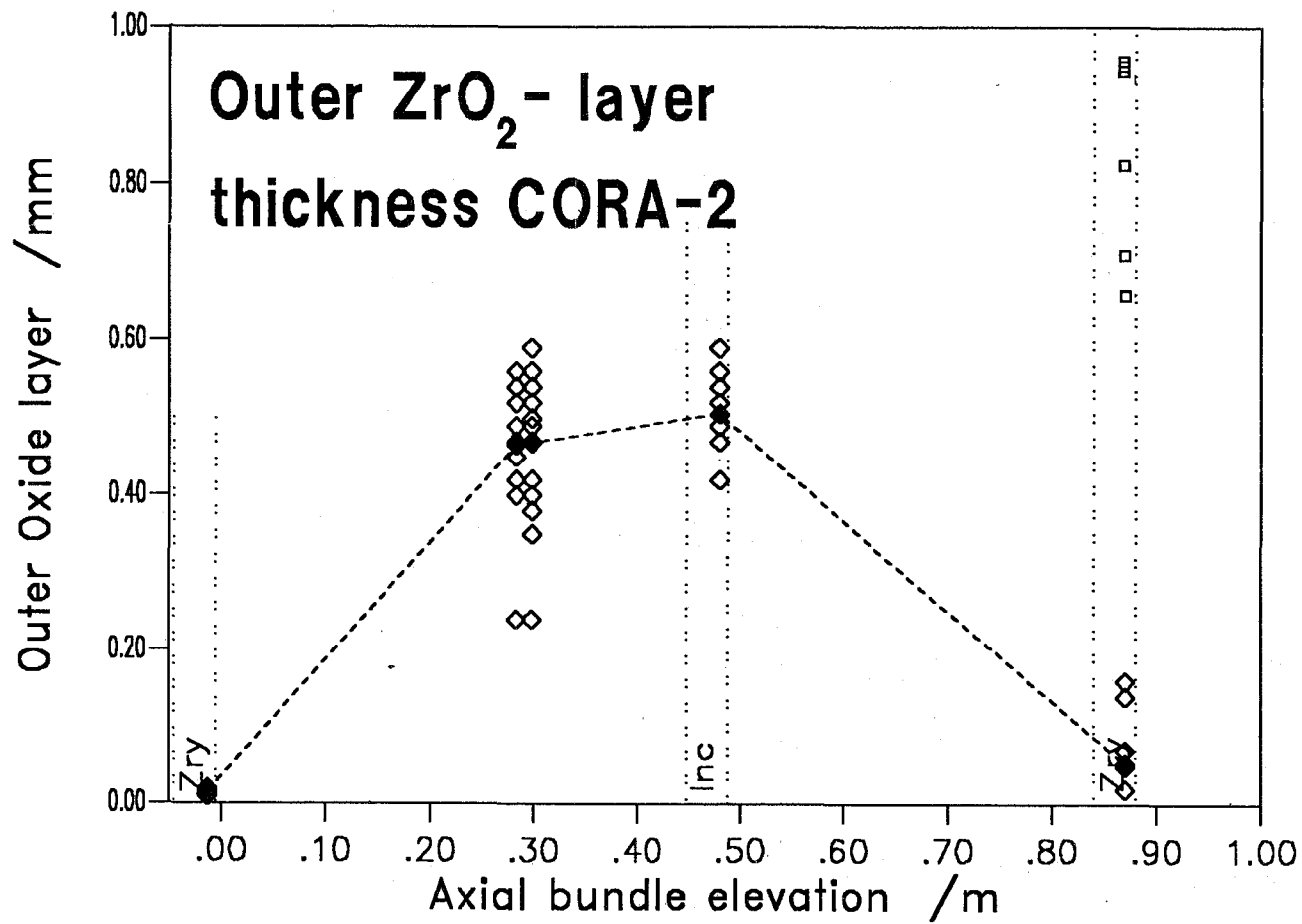


**Figure 10. Outer oxidized layer thicknesses of CORA-2:** solid symbols indicate the average ZrO<sub>2</sub> layer thicknesses. Maximum values of the corner rods at 870 mm are also presented.

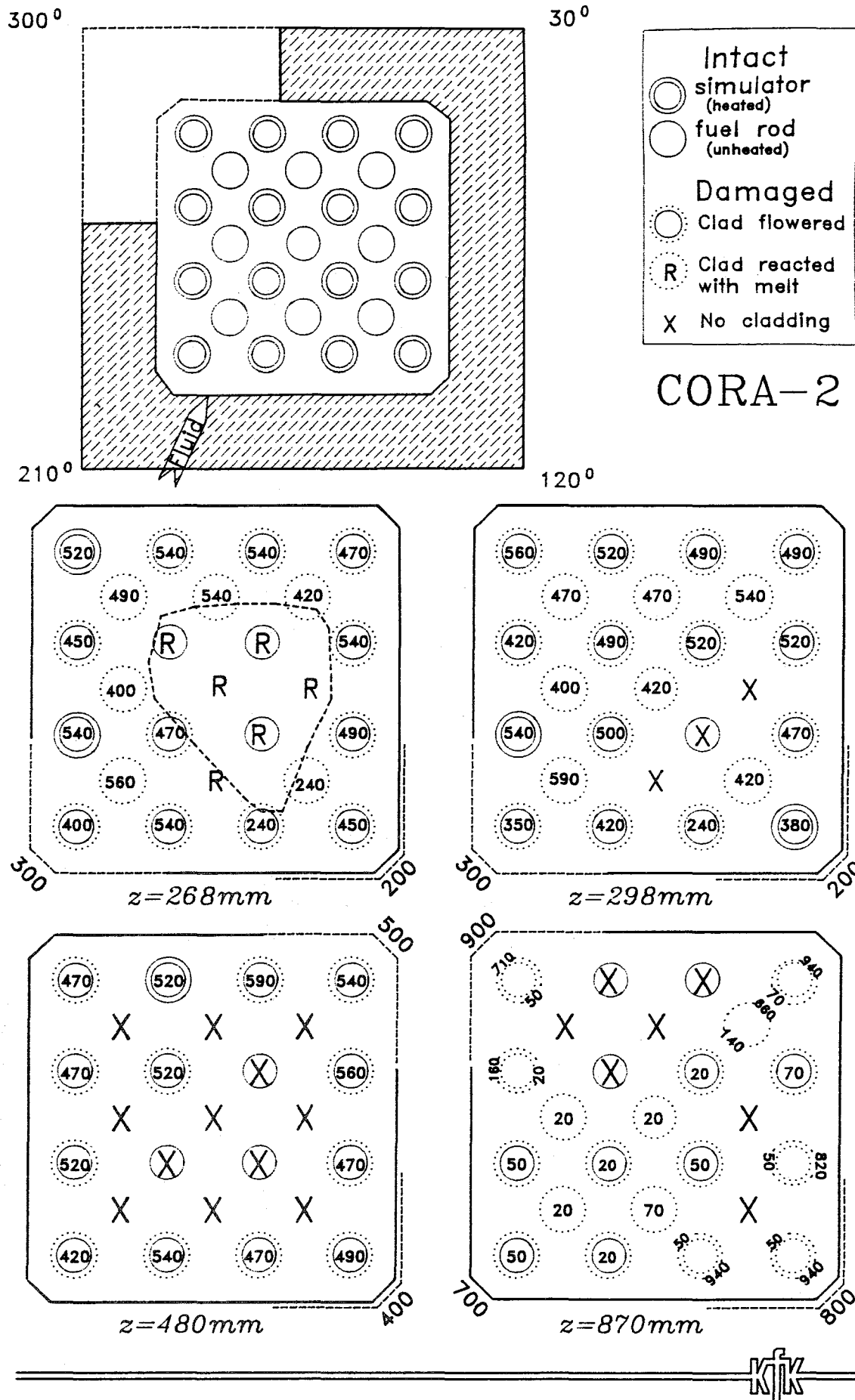
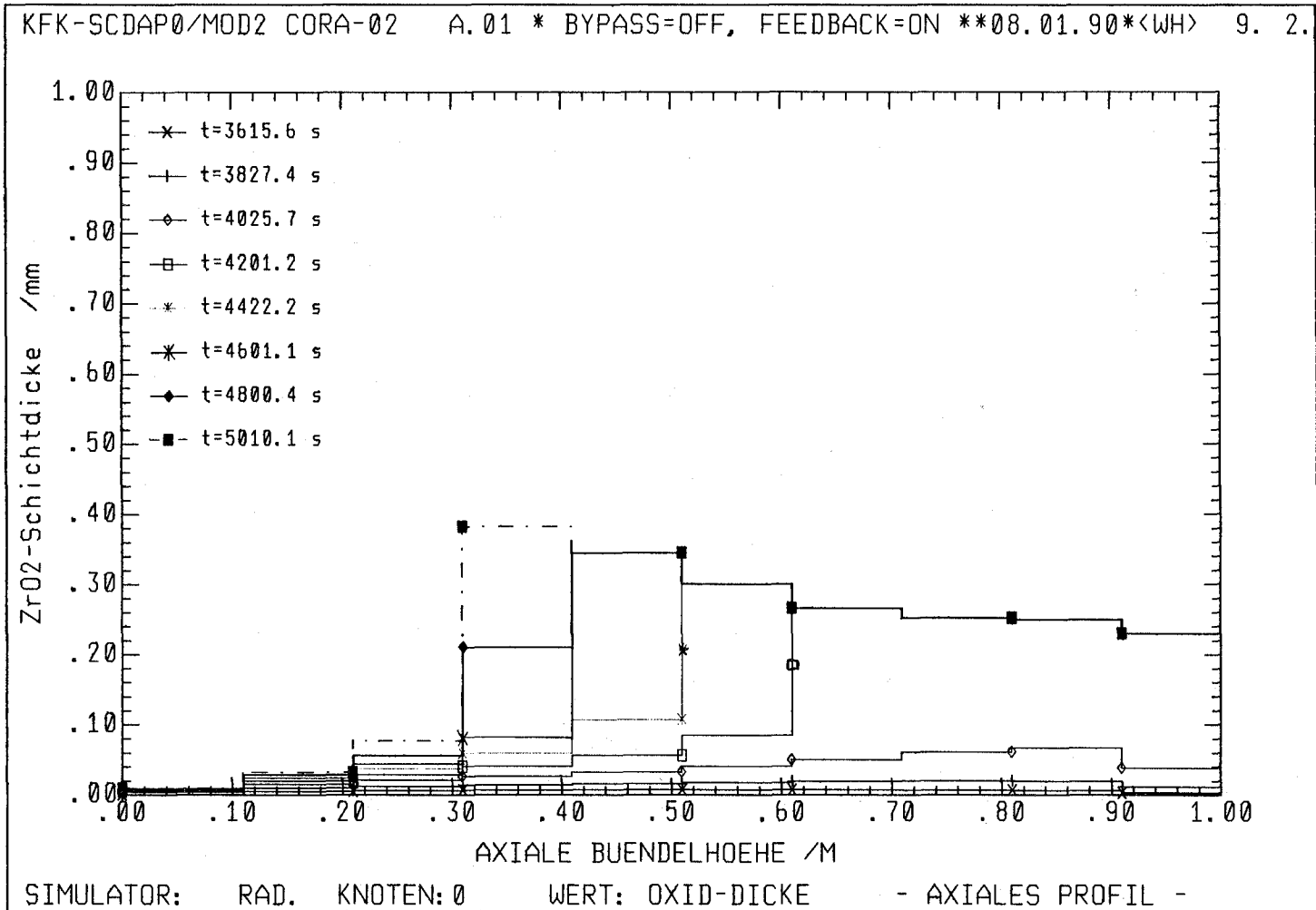


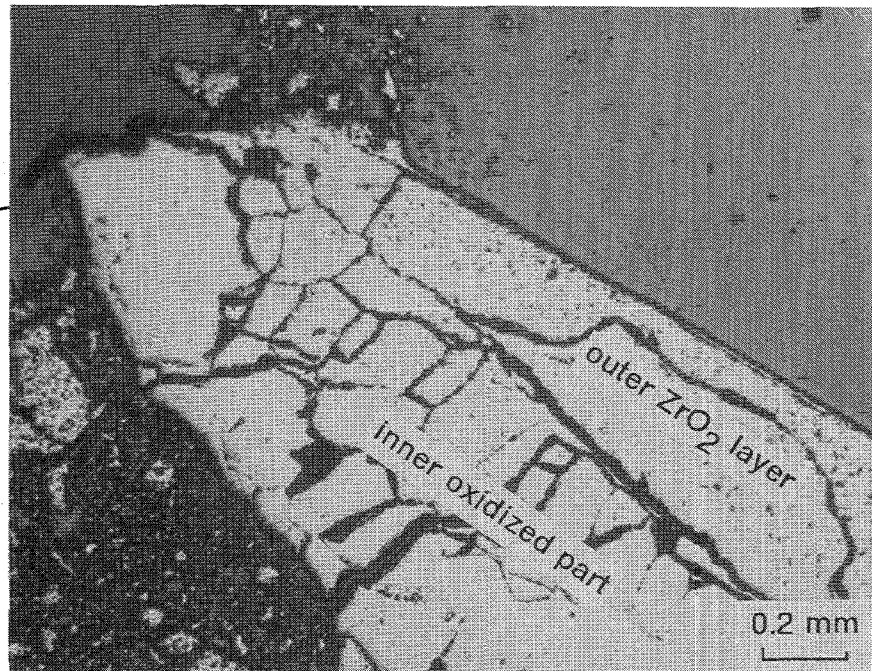
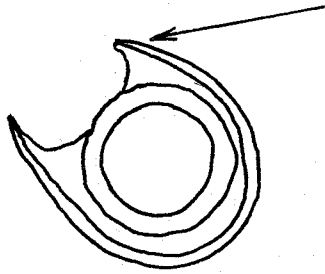
Figure 11. CORA-2, axial and radial variation of the cladding state: numbers indicate outer  $ZrO_2$  layer thicknesses in  $\mu m$ , and the boundaries of blocked areas are marked by dashed lines.





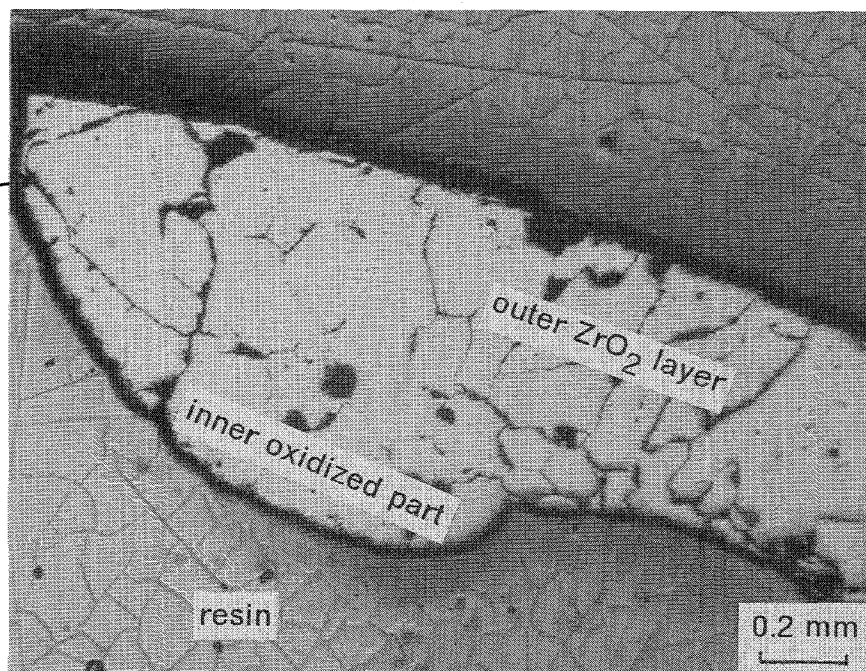
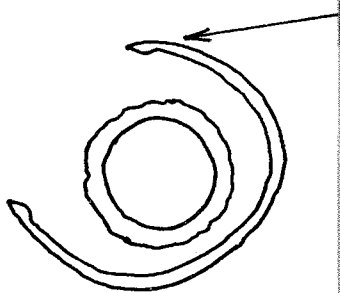
**Figure 12. Calculated outer oxidized layer thickness for CORA-2:** results of a calculation performed with the extended version of SCDAP/MOD1, neglecting the influence of the windows in the shroud /17/.

at 298 mm



(a)

at 480 mm



(b)

KfK

**Figure 13. CORA-2, flowering of the claddings:** (a) remaining of an inner oxidized part at 298 mm; (b) loss of most of inner oxidized part at 480 mm.

at 480 mm

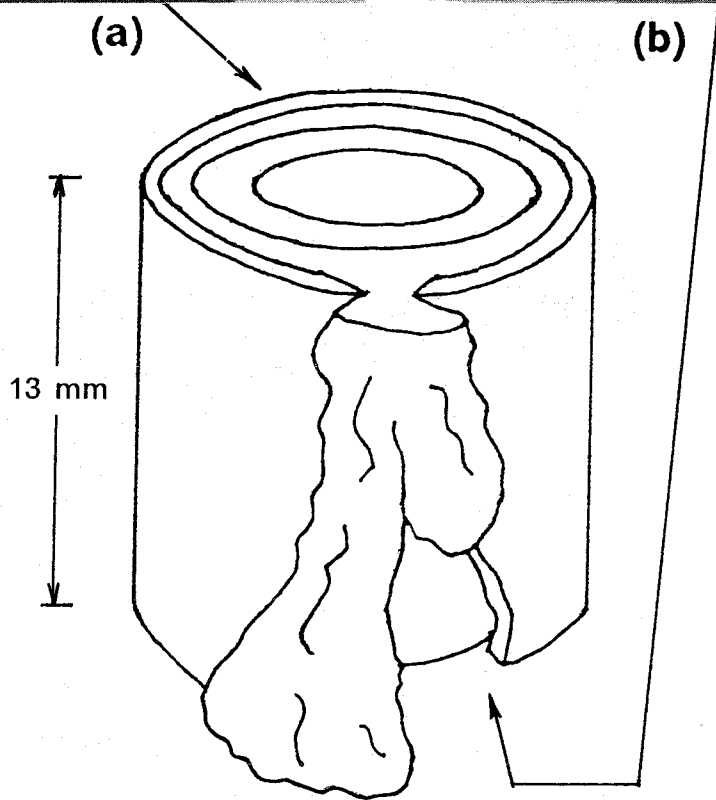
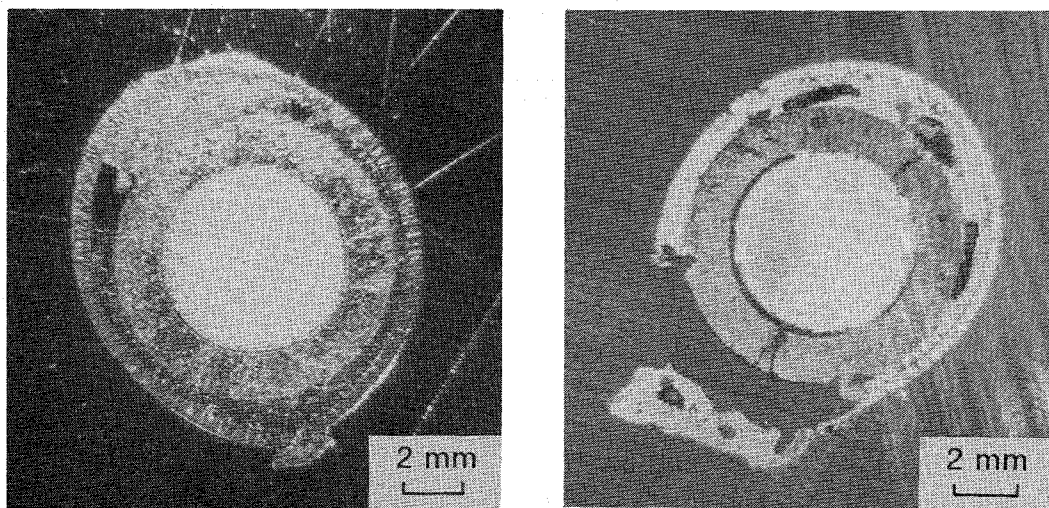


**Figure 14. CORA-2, cladding deformation:** (a) at 480 mm molten material penetrates the  $ZrO_2$  layer and refreezes due to oxidation; (b) at 467 mm failure of the cladding with release of melt forming voids.

at 298 mm

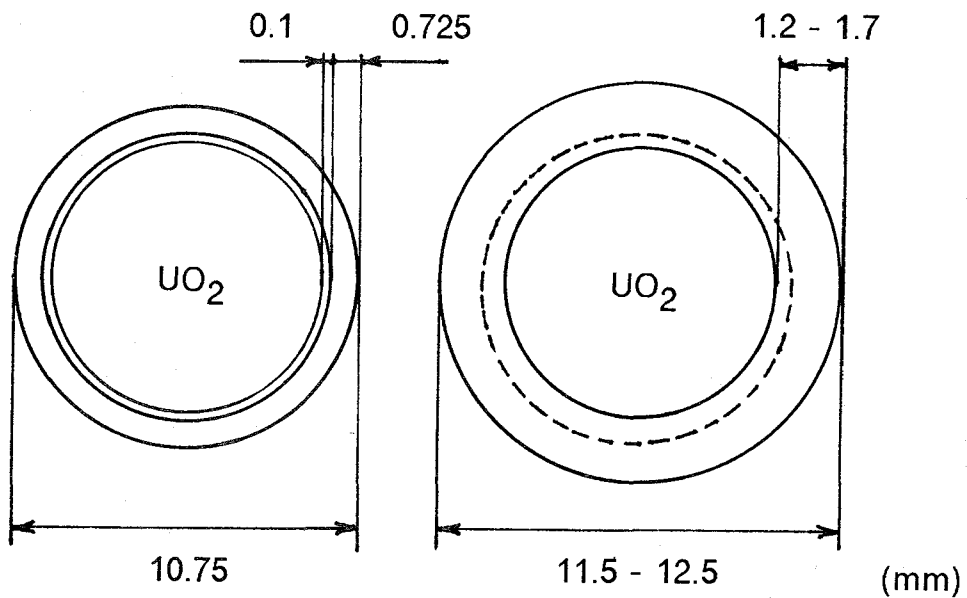
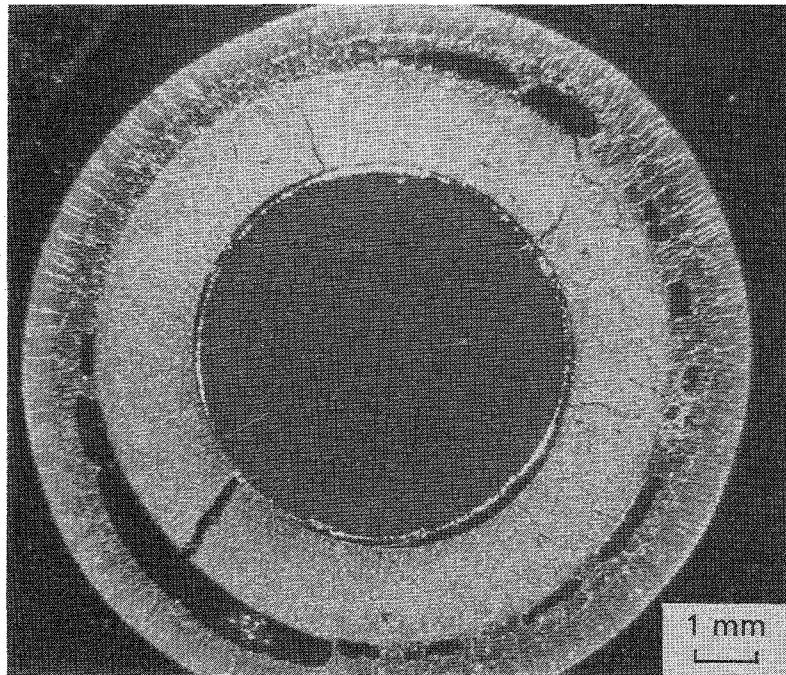


**Figure 15. CORA-2, radial growth of the claddings:** typical intact rod at 298 mm (top), and comparison of the diameters with the initial state in the schematic below left.

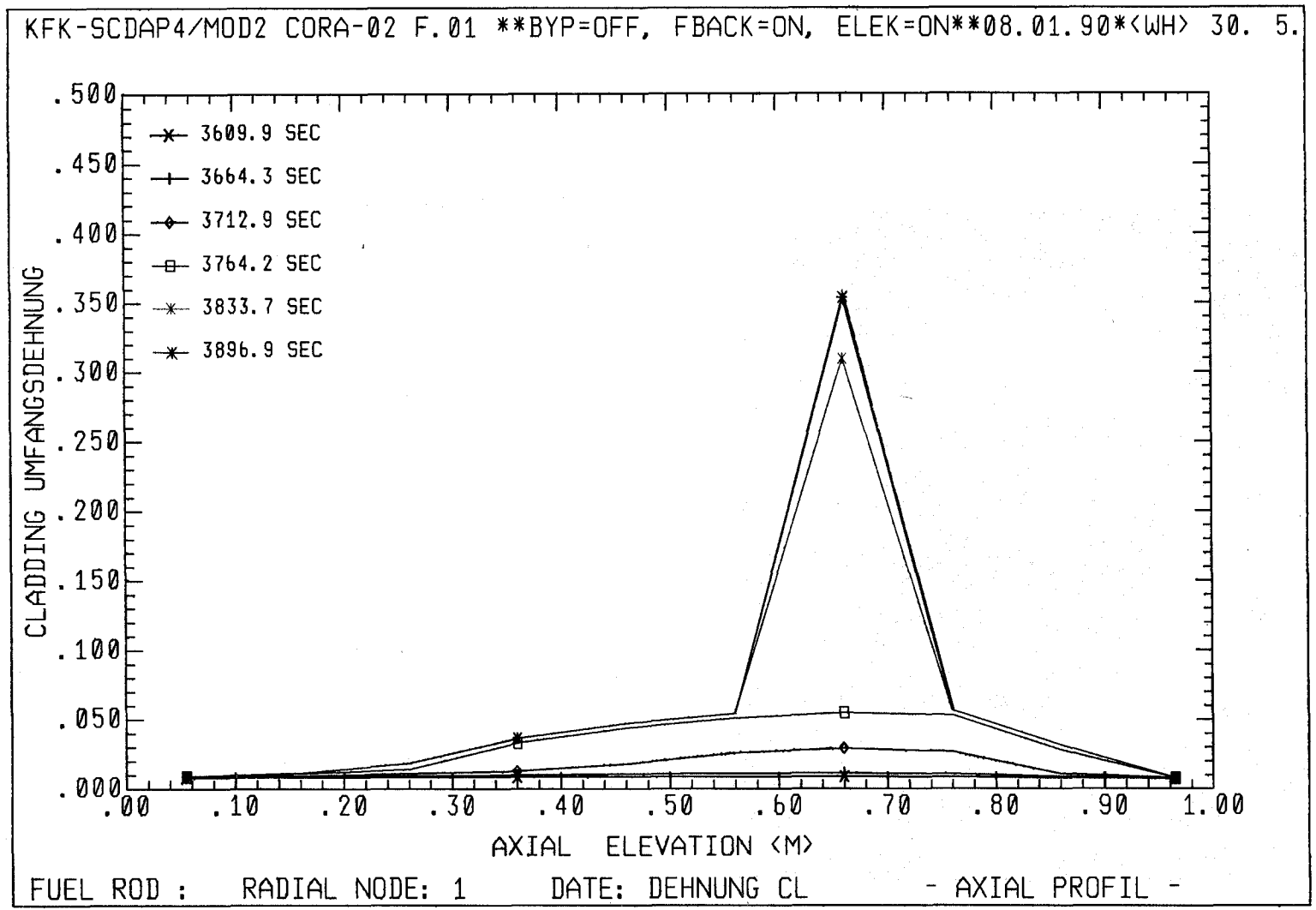
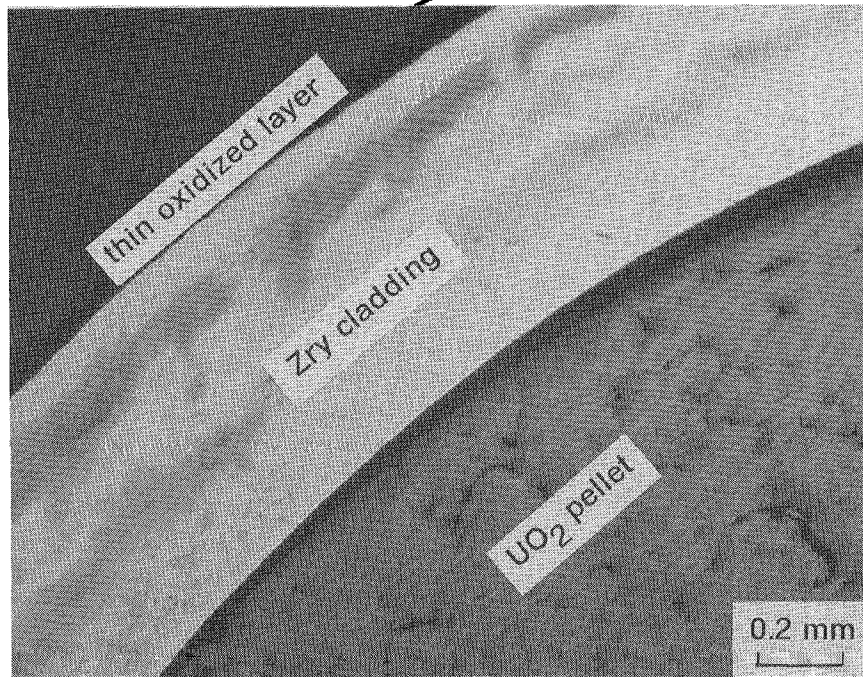
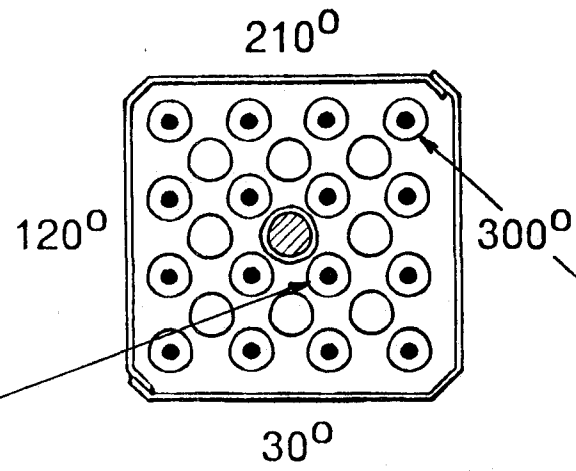
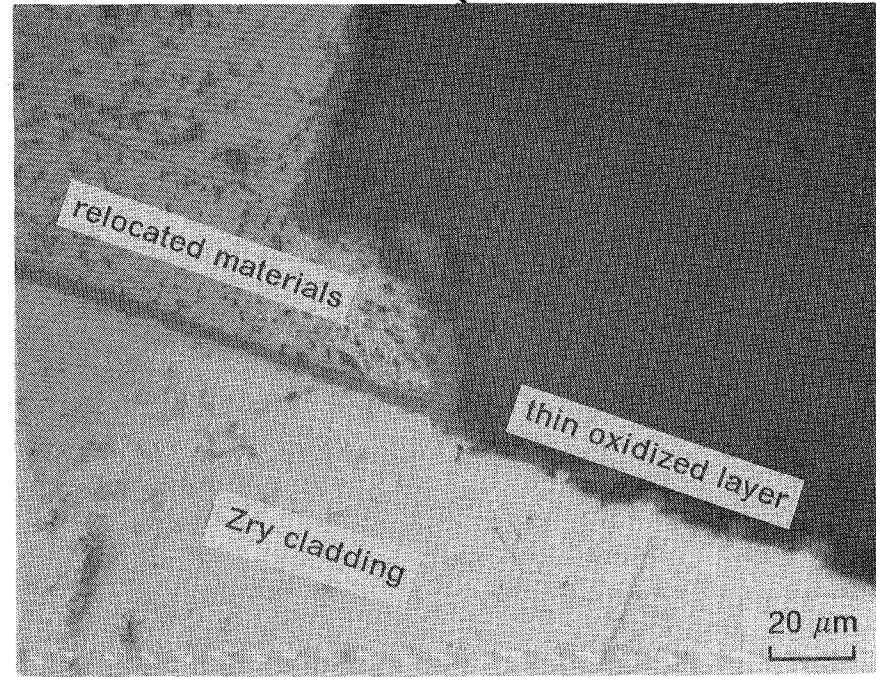


Figure 16. CORA-2, calculated deformation of the claddings: performed with the extended version of SCDAP/MOD1 code indicating clad rupture at 0.65 m bundle elevation /17/.

at 95 mm



(a)



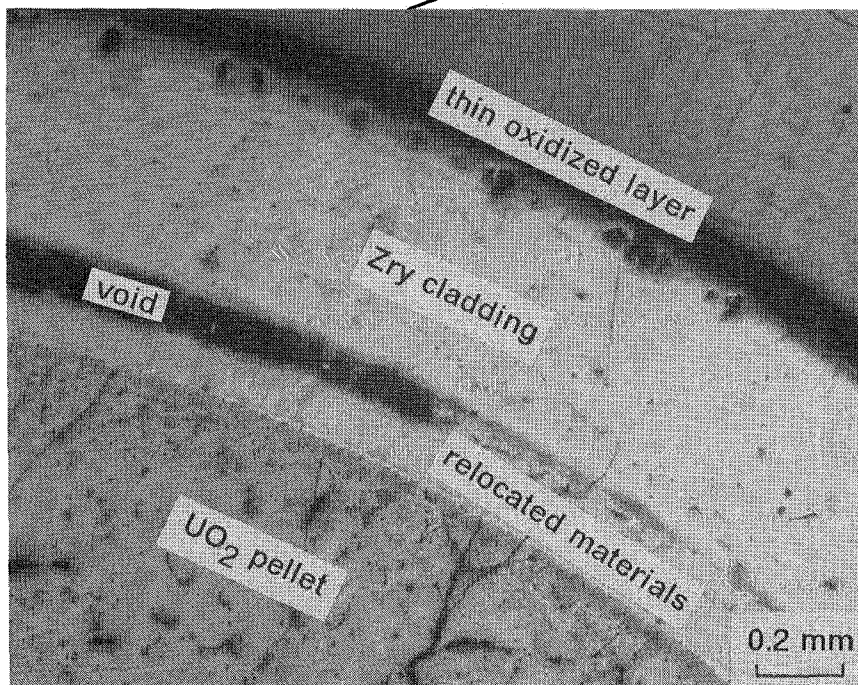
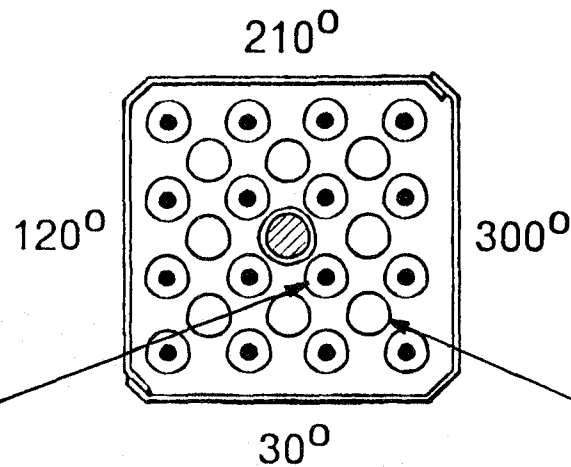
(b)



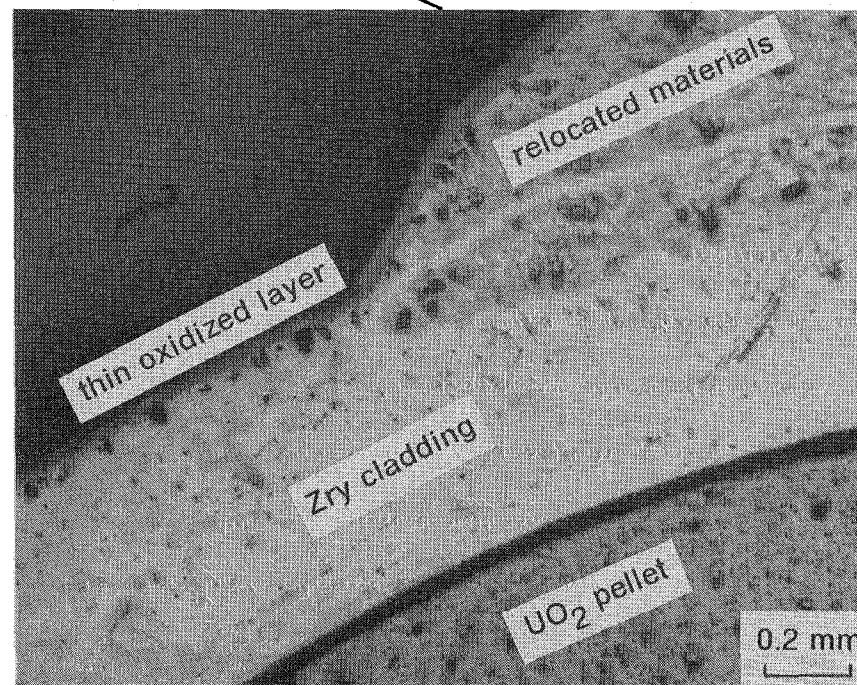
Figure 17. CORA-5, fuel rods at 95 mm elevation: (a) a thin oxidized layer on the outer surface; (b) relocated material on the outer surface.



at 208 mm



(a)

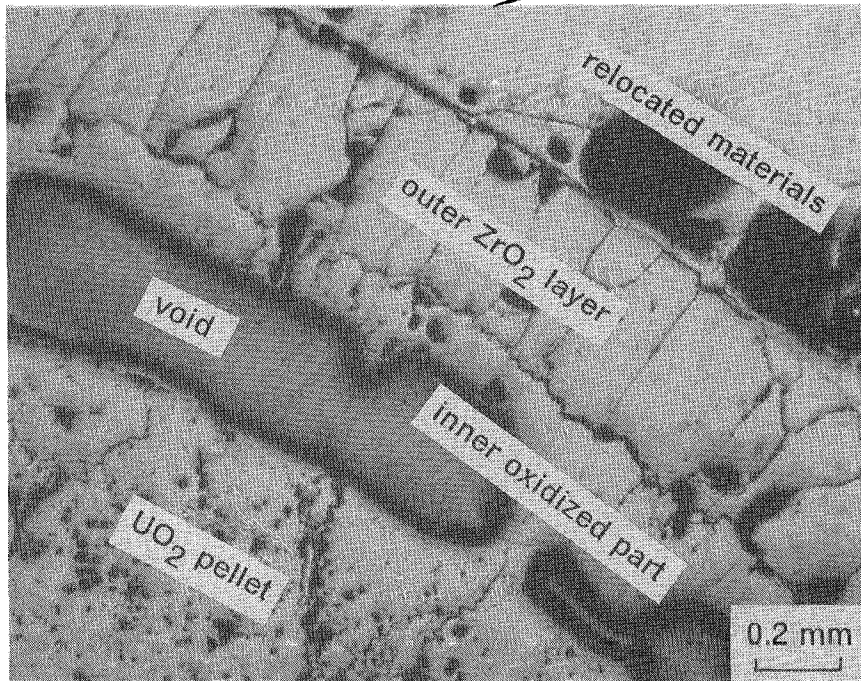
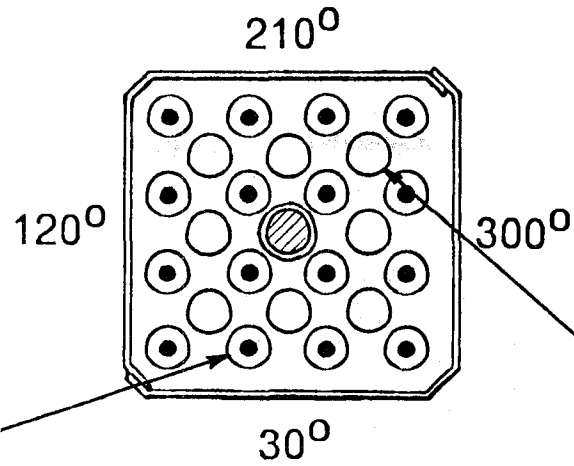


(b)

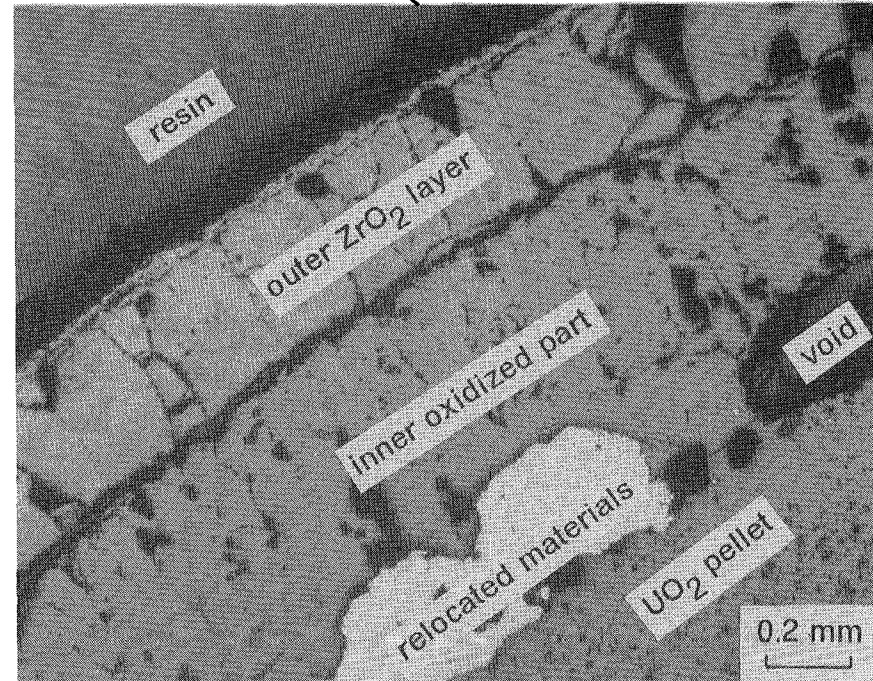


**Figure 18. CORA-5, fuel rods at 208 mm elevation:** (a) locally relocated material between pellet and cladding; (b) relocated material on the outer surface.

at 393 mm



(a)



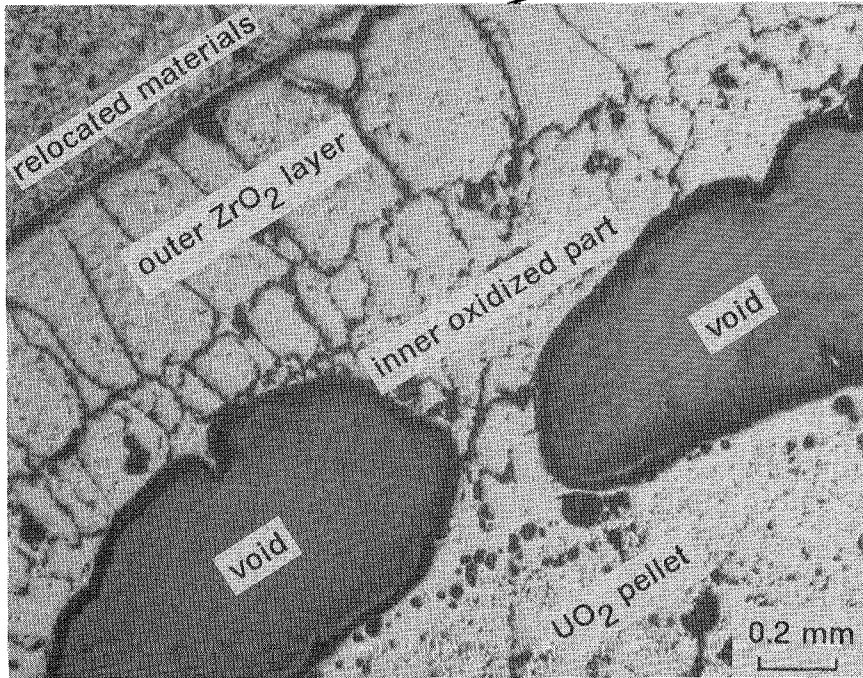
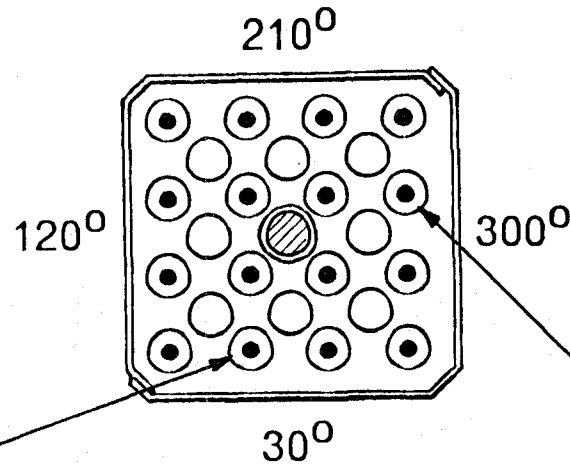
(b)



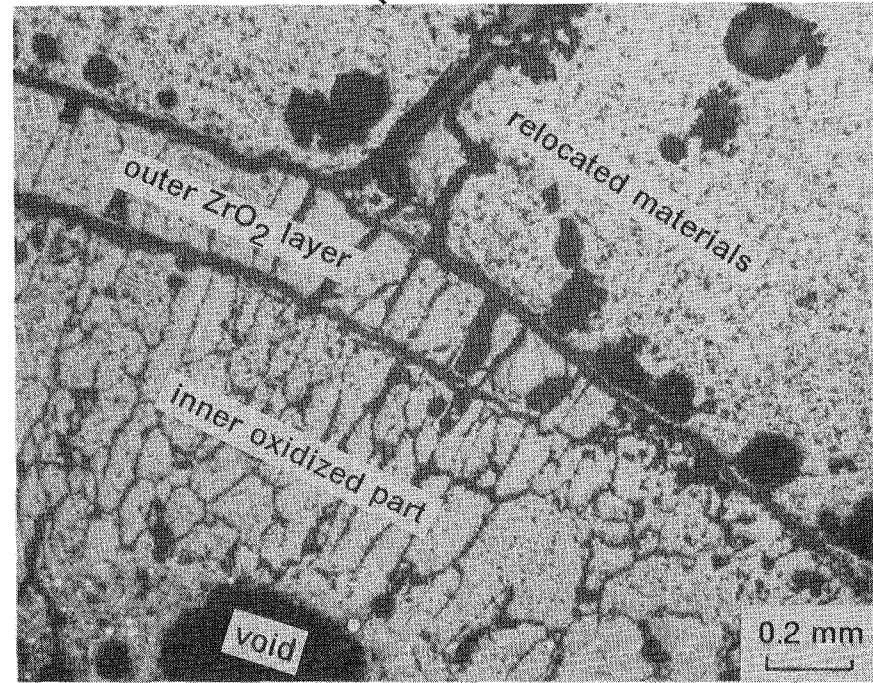
**Figure 19. CORA-5, fuel rods at 393 mm elevation:** (a) complete oxidation of the cladding with voids and relocated material on the outer surface; (b) complete oxidation of the cladding with relocated material on the inner surface.



at 408 mm



(a)

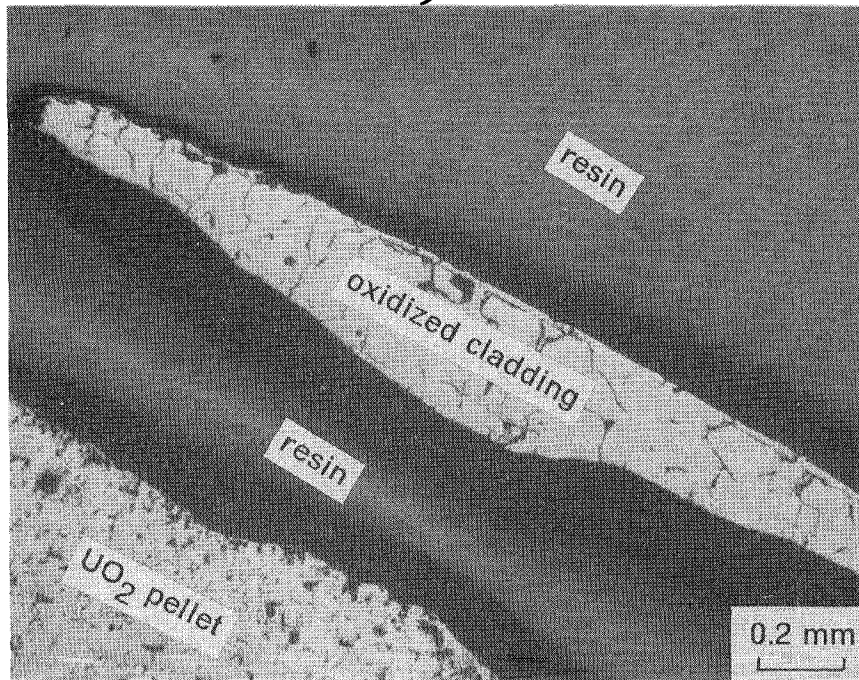
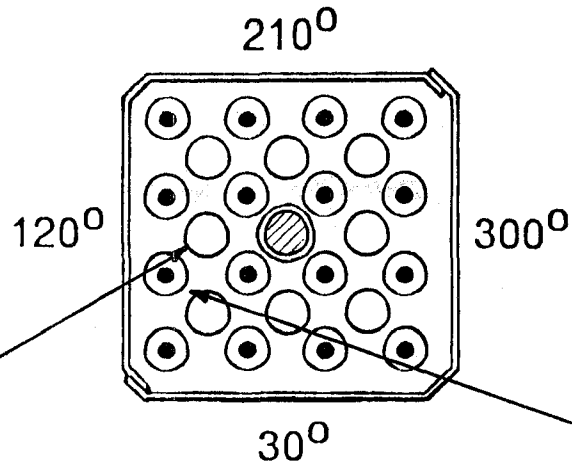


(b)

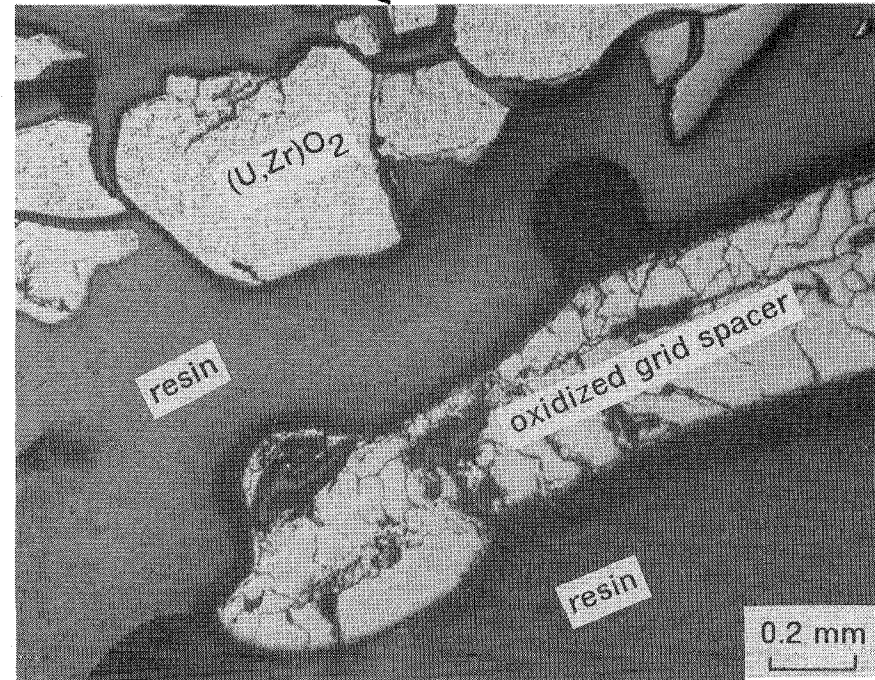


**Figure 20.** CORA-5, fuel rods at 408 mm elevation: (a) complete oxidation of the cladding with voids; (b) complete oxidation at breached part of the cladding.

at 853 mm



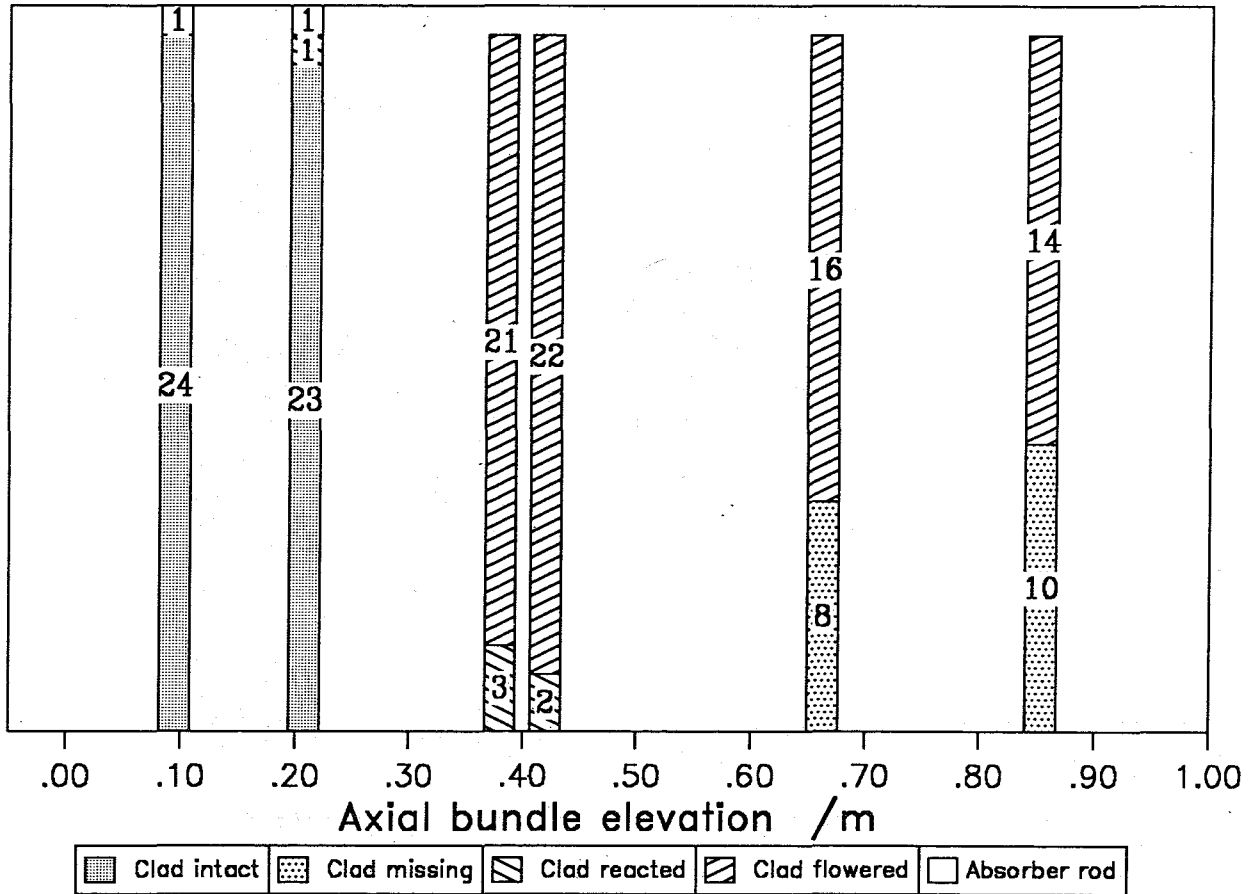
(a)



(b)

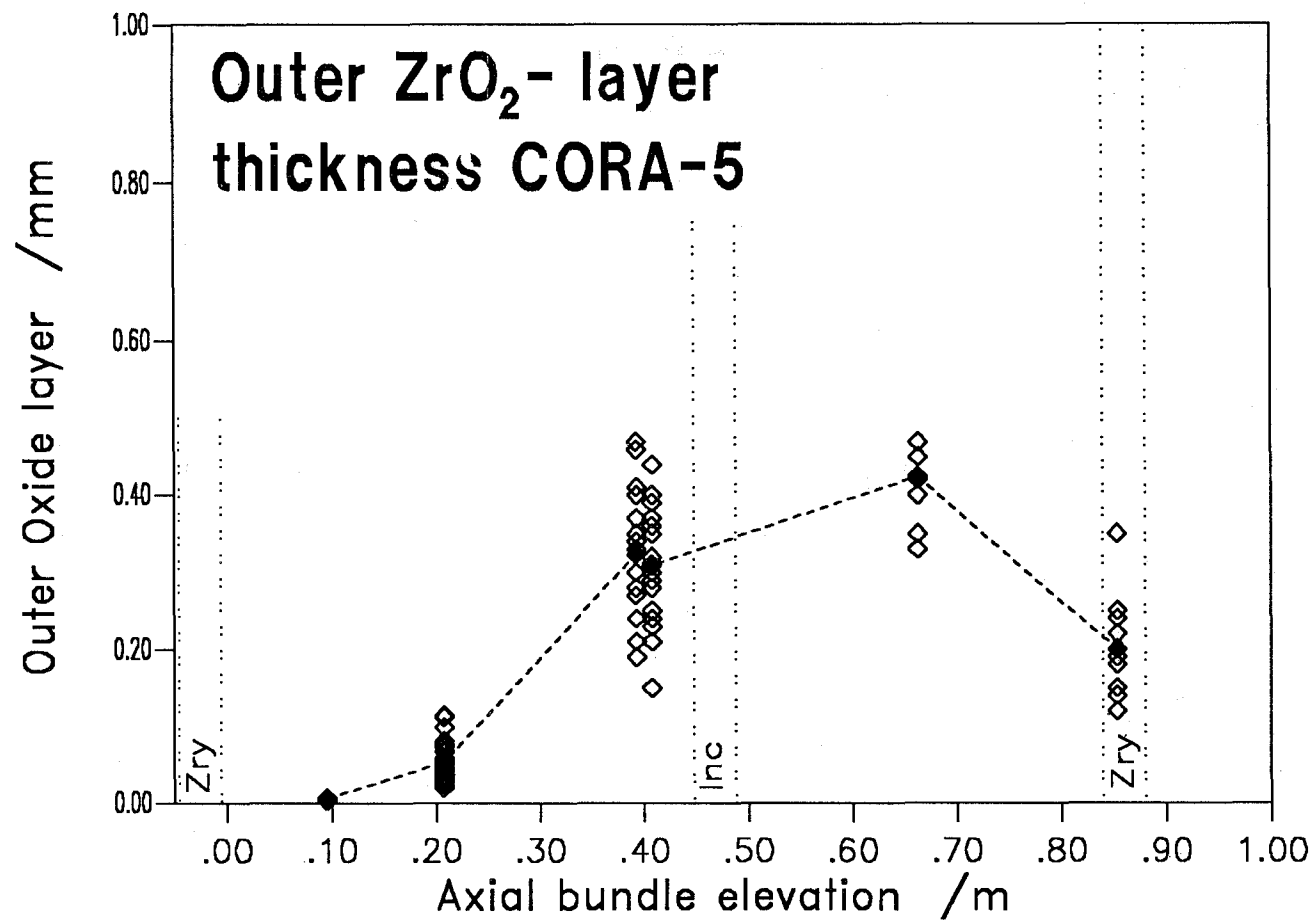


Figure 21. CORA-5, fuel rod and spacer at 853 mm elevation: (a) complete oxidation of cladding remnant; (b) complete oxidation of remnant grid spacer.



CORA-5 Elevation /mm	Cladding intact	Cladding missing	Cladding reacted	Cladding flowered	Absorber rod
95	24	0	0	0	1
208	23	0	1	0	1
393	0	0	3	21	0
408	0	0	2	22	0
663	0	8	0	16	0
853	0	10	0	14	0

Figure 22. CORA-5, end state of the claddings: claddings are classified as intact, missing, reacted, and flowered. Furthermore the clad state of the absorber rod is added.



**Figure 23.** Outer oxidized layer thicknesses of CORA-5: measured for all rods at the elevation given. Solid symbols indicate the average thicknesses.

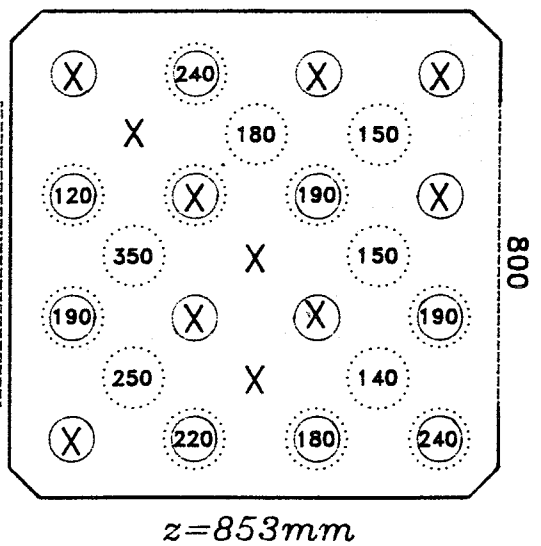
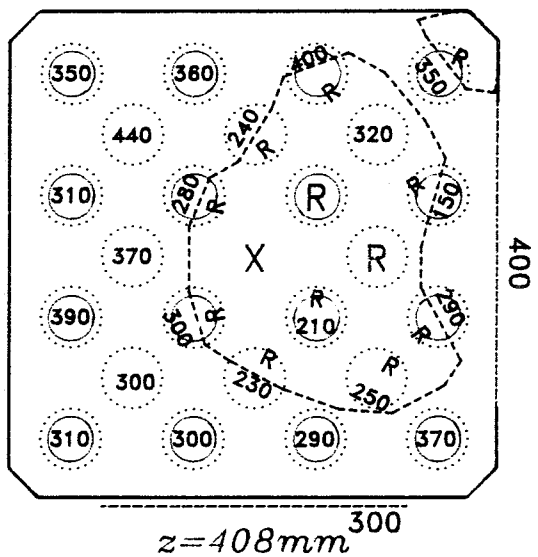
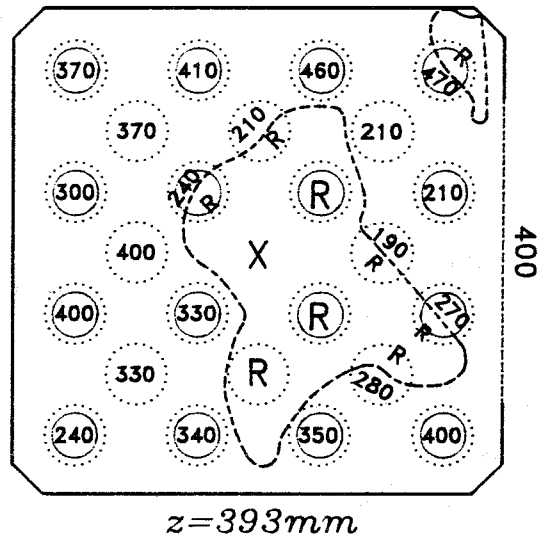
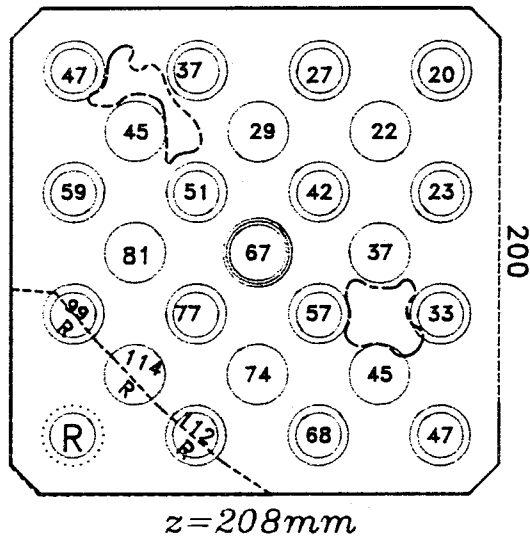
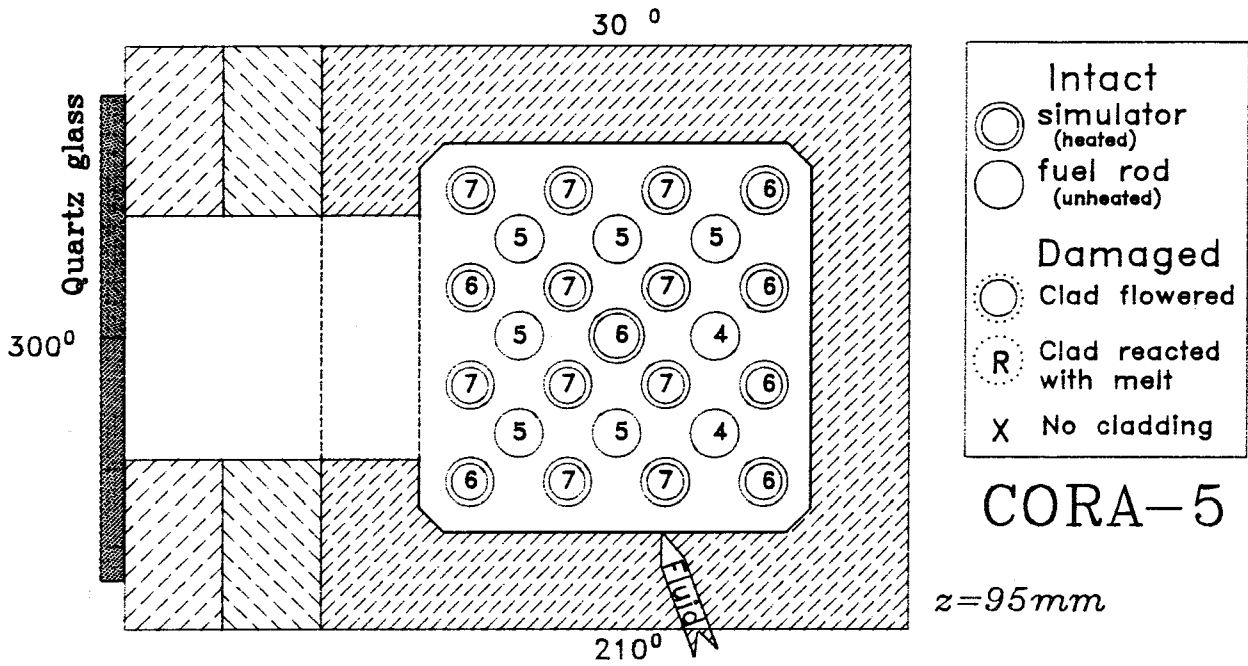
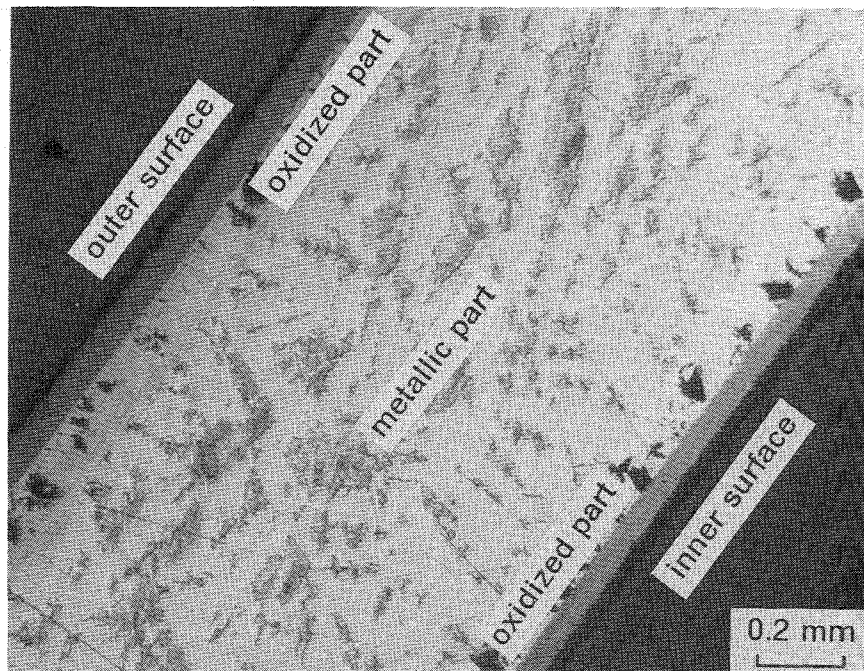


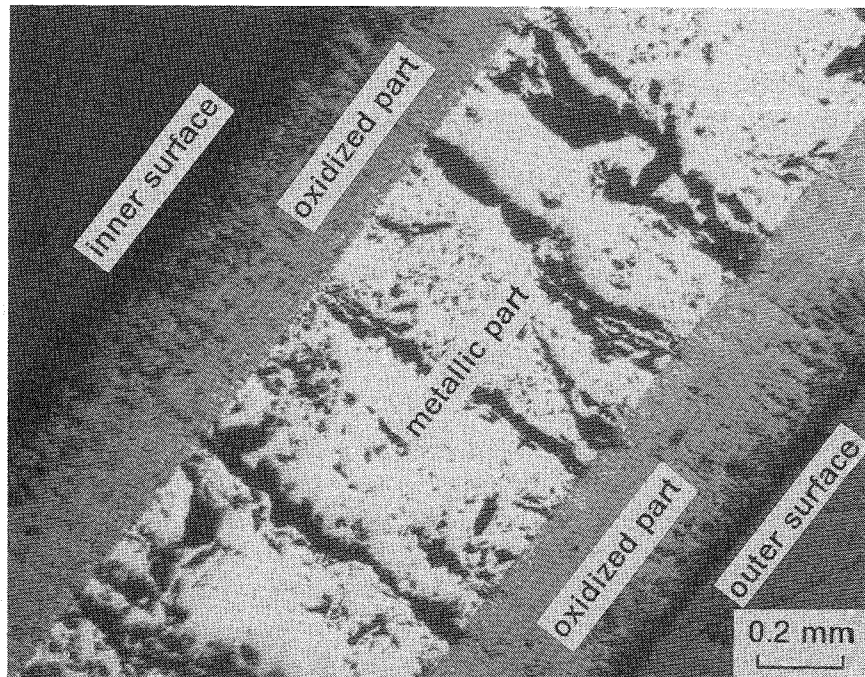
**Figure 24. CORA-5, axial and radial variation of the cladding state:** numbers indicate outer  $\text{ZrO}_2$  layer thicknesses in  $\mu\text{m}$ , and the boundaries of blocked areas are marked by dashed lines.



around 270 mm



(a)

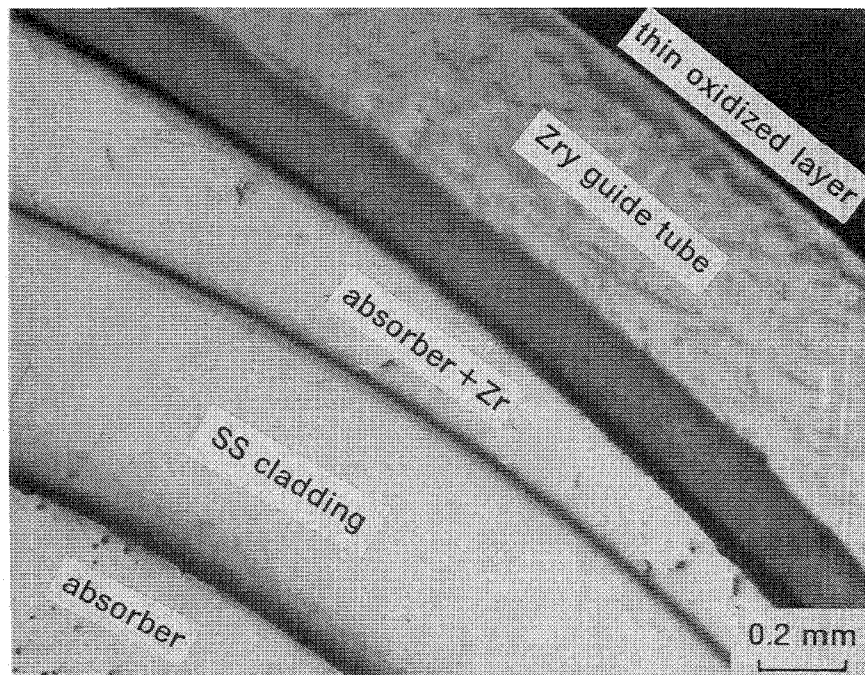


(b)



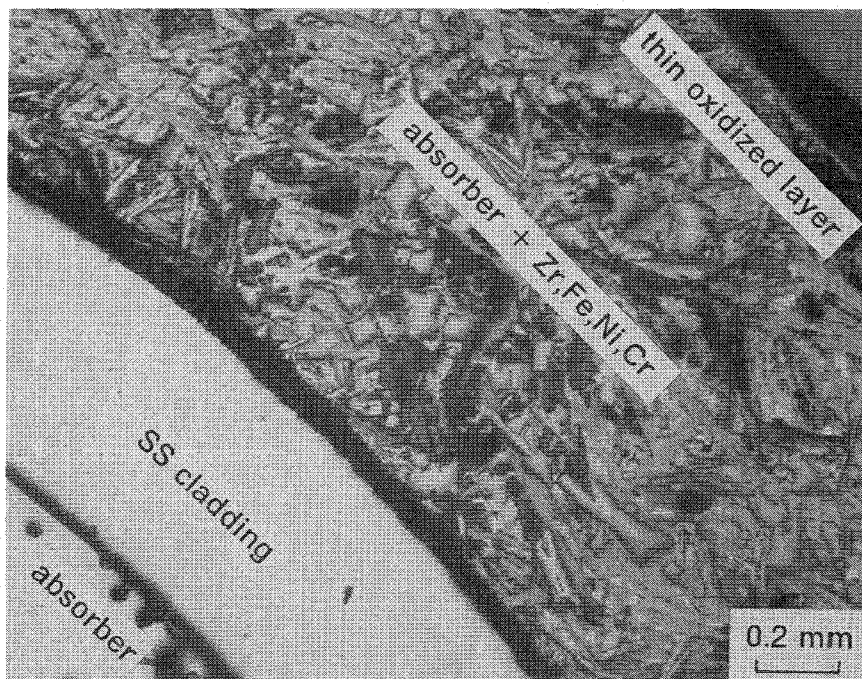
**Figure 25. CORA-5, shroud at around 270 mm elevation:** double-sided oxidation; (a) in the direction of  $30^{\circ}$  as well as (b) in the direction of  $210^{\circ}$ .

at 95 mm



(a)

at 208 mm

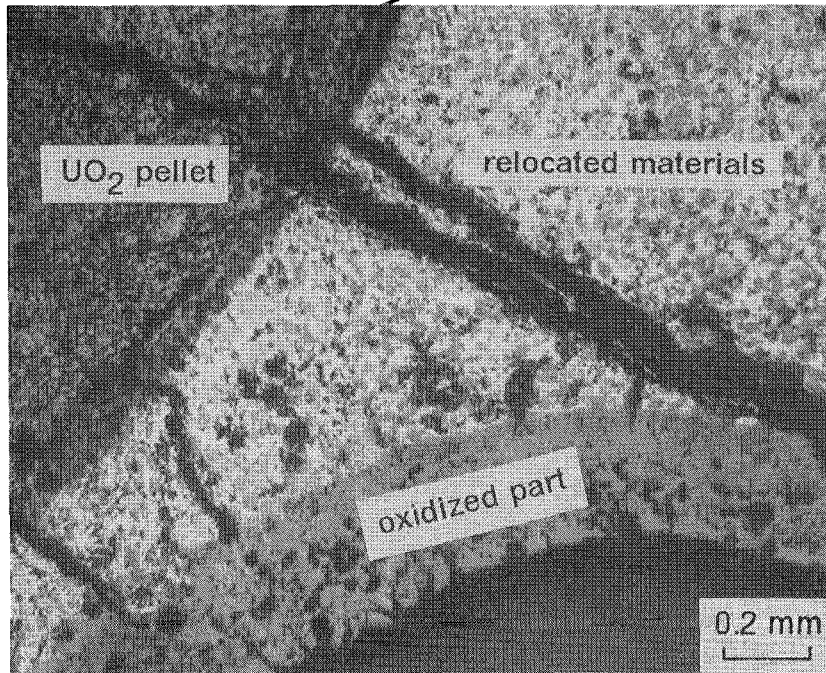
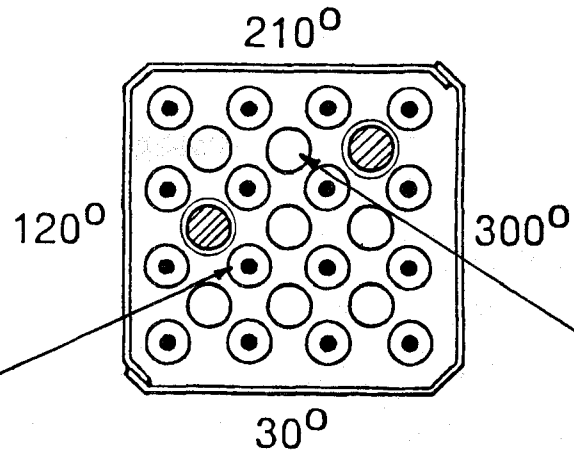


(b)

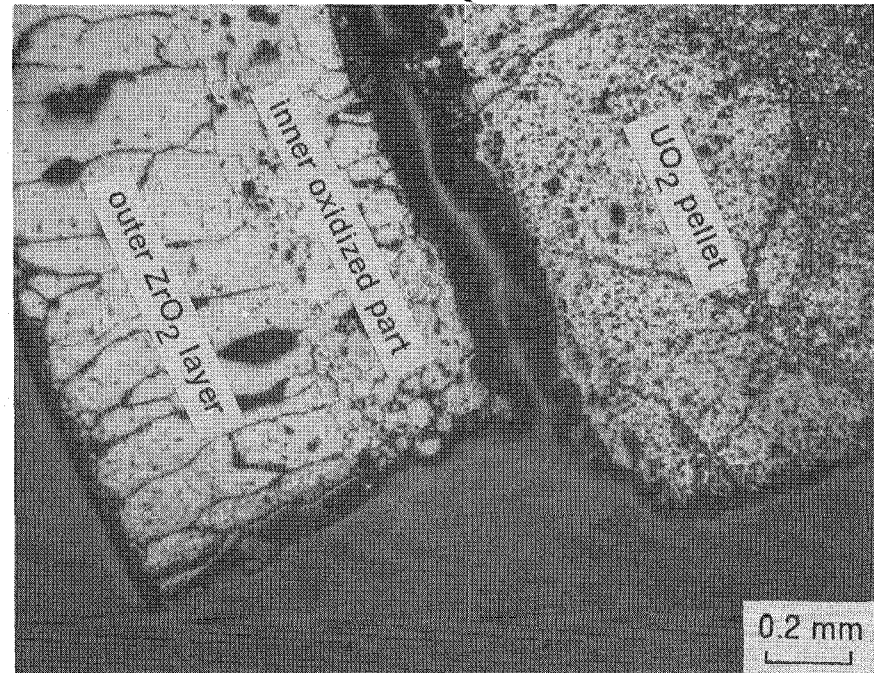


**Figure 26. CORA-5, central absorber rod:** (a) relocated material between ss cladding and Zry guide tube at 95 mm; (b) dissolution of Zry guide tube at 208 mm.

at 216 mm



(a)



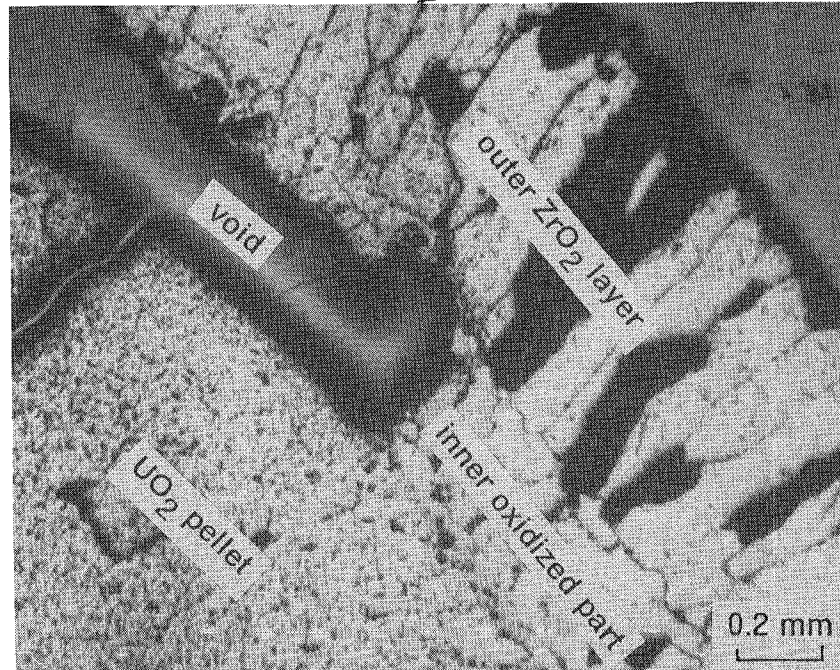
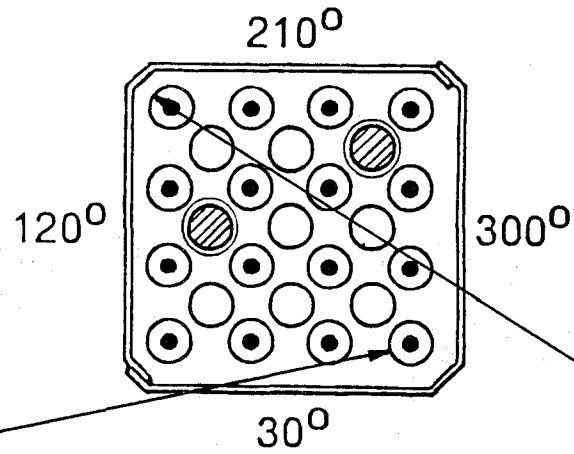
(b)

KfK

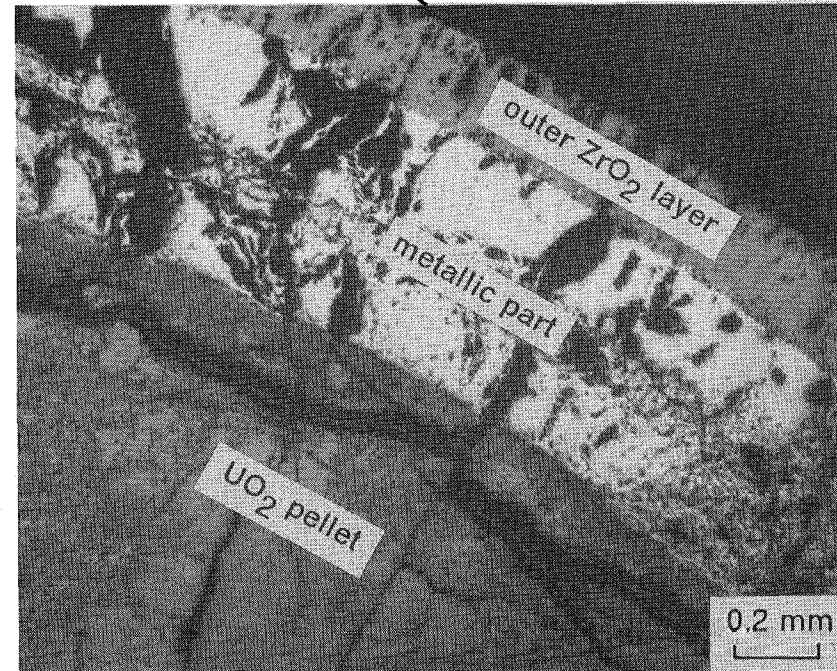
**Figure 27. CORA-12, fuel rods at 216 mm elevation (1):** (a) interaction of the cladding with relocated melt; (b) mechanically broken part of the fuel rod.



at 216 mm



(a)

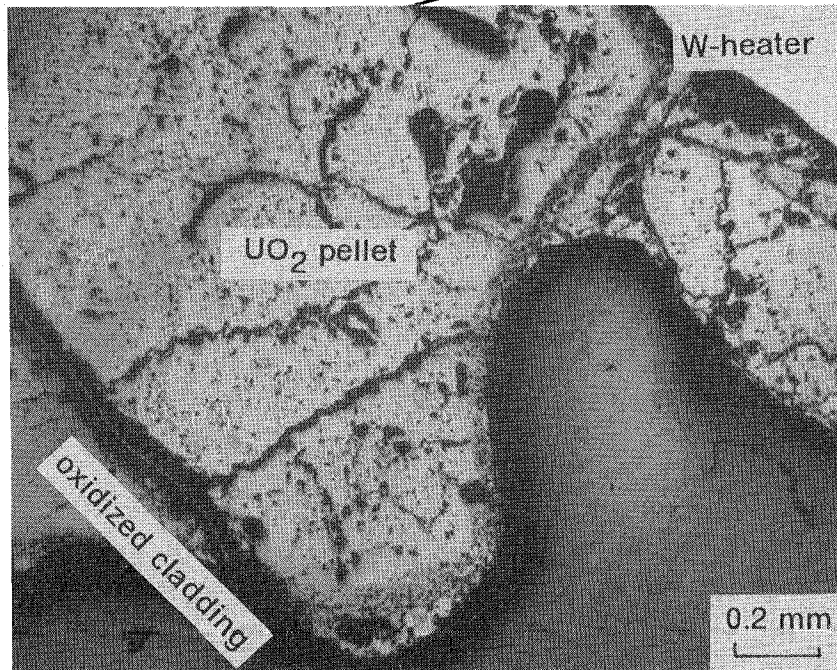
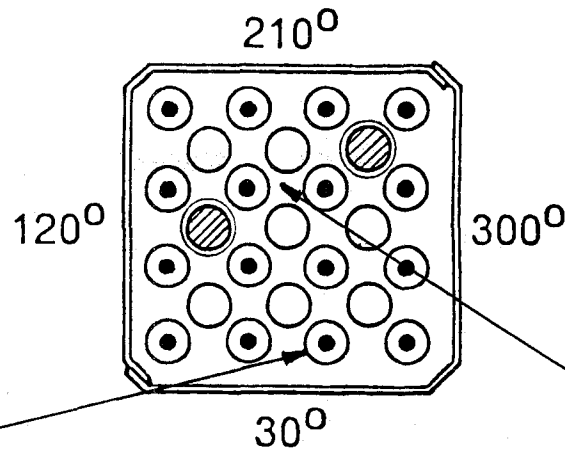


(b)

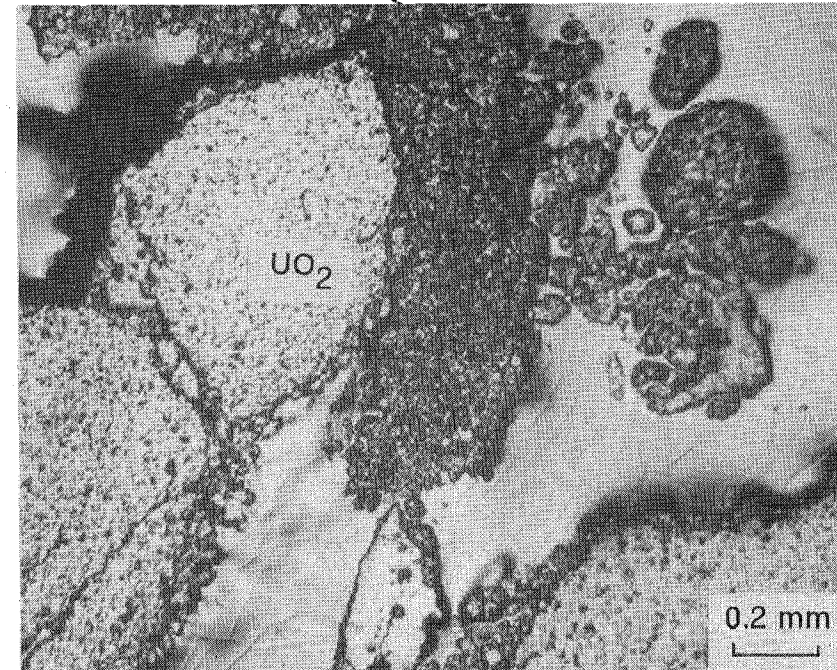


**Figure 28.** CORA-12, fuel rods at 216 mm elevation (2): (a) complete oxidation of the cladding; (b) remaining metallic part in the middle of the cladding.

at 533 mm



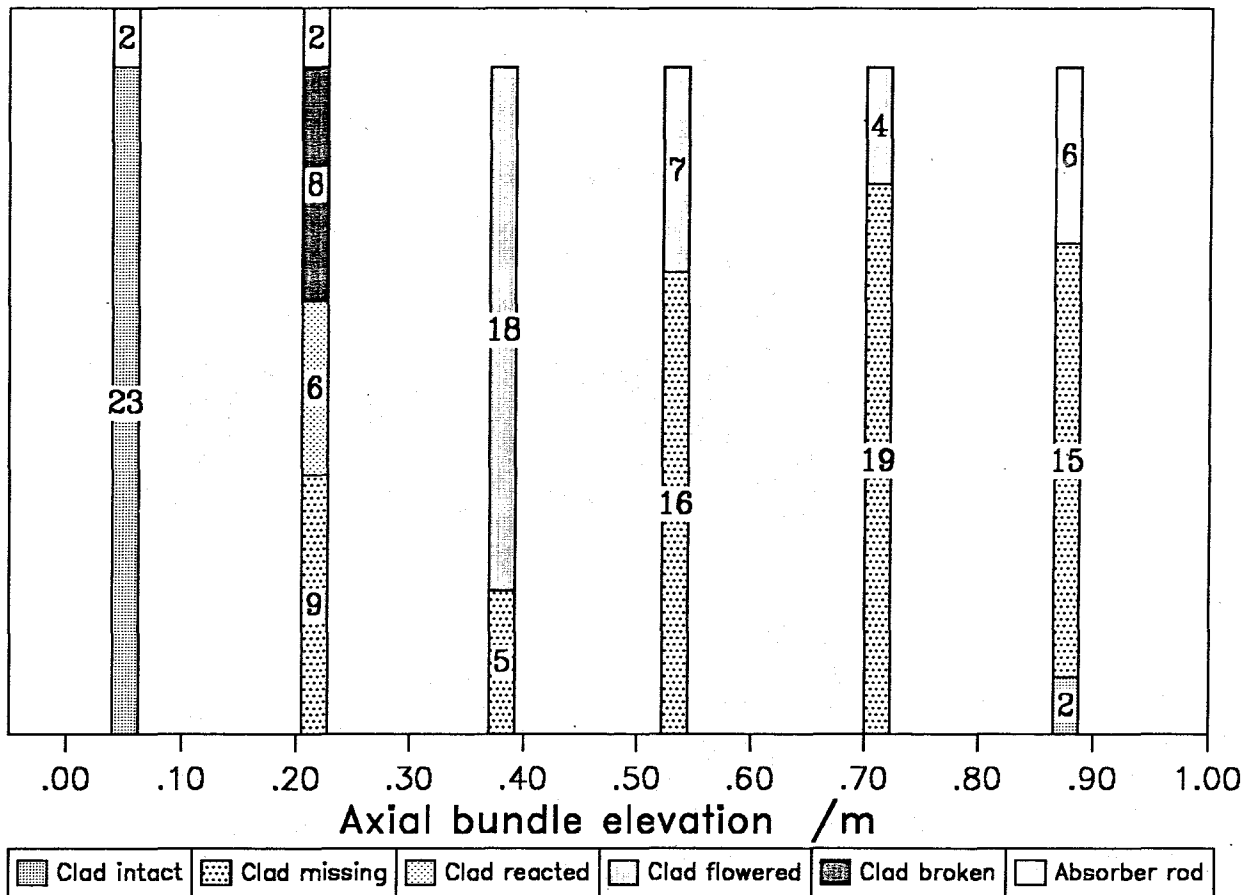
(a)



(b)



**Figure 29. CORA-12, fuel rod and rubble at 533 mm elevation:** (a) interaction of the pellet with relocated melt; (b) rubble which has been collected at the central part of the bundle cross section.



CORA-12 Elevation (mm)	Cladding intact	Cladding missing	Cladding reacted: chemical	Cladding flowered: melting	Cladding broken: mechanical	Absorber rod
51	23	0	0	0	0	2
216	0	9	6	0	8	2
381	0	5	0	18	0	0
533	0	16	0	7	0	0
711	0	19	0	4	0	0
876	2	15	0	6	0	0

**Figure 30. CORA-12, end state of the claddings:** claddings are classified as intact, missing, reacted, flowered, and mechanically broken, may be due to thermal shock. Furthermore the clad state of the two absorber rod is added.

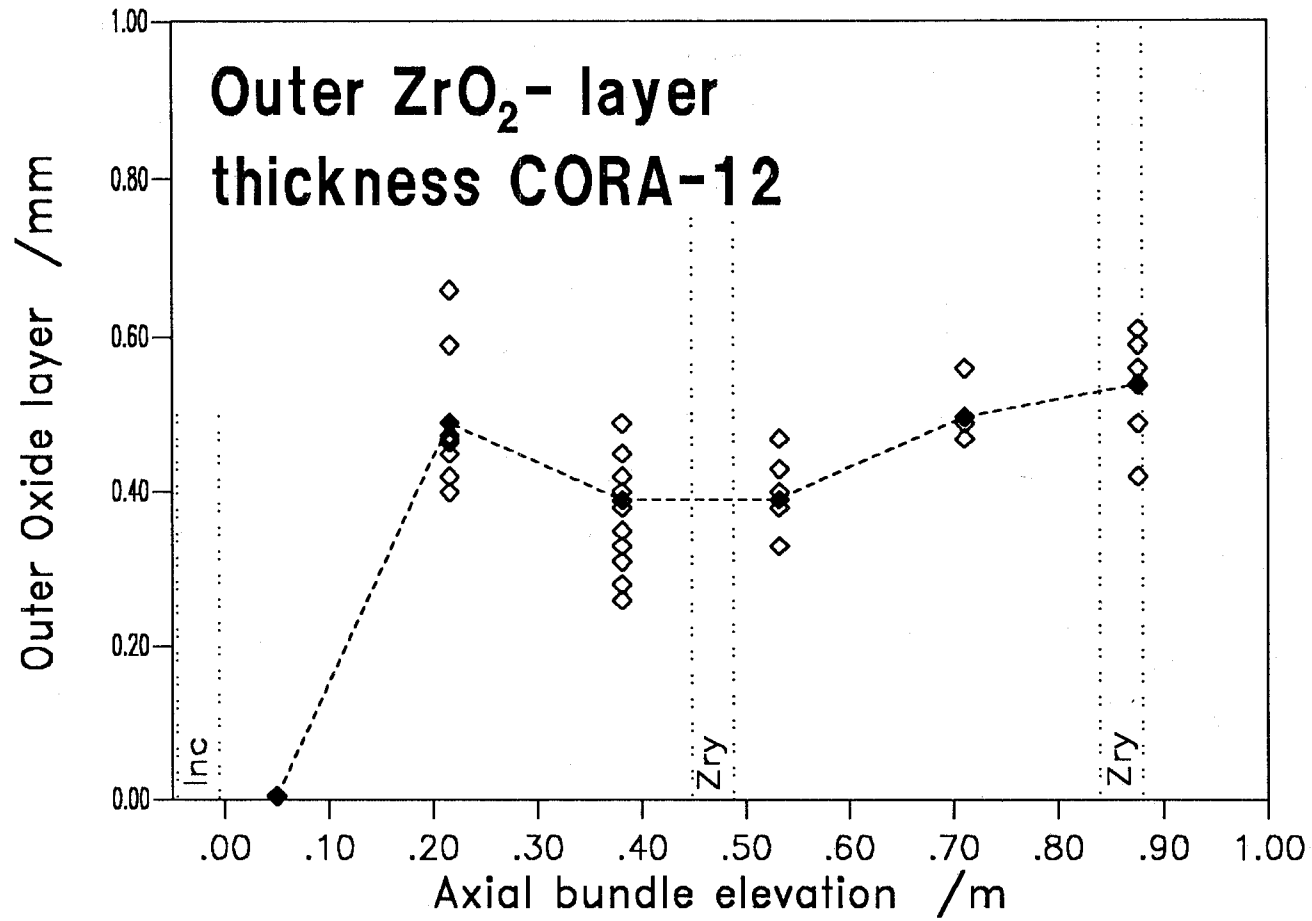


**Figure 31. Outer oxidized layer thicknesses of CORA-12:** measured for all rods at the elevation given. Solid symbols indicate the average thicknesses.

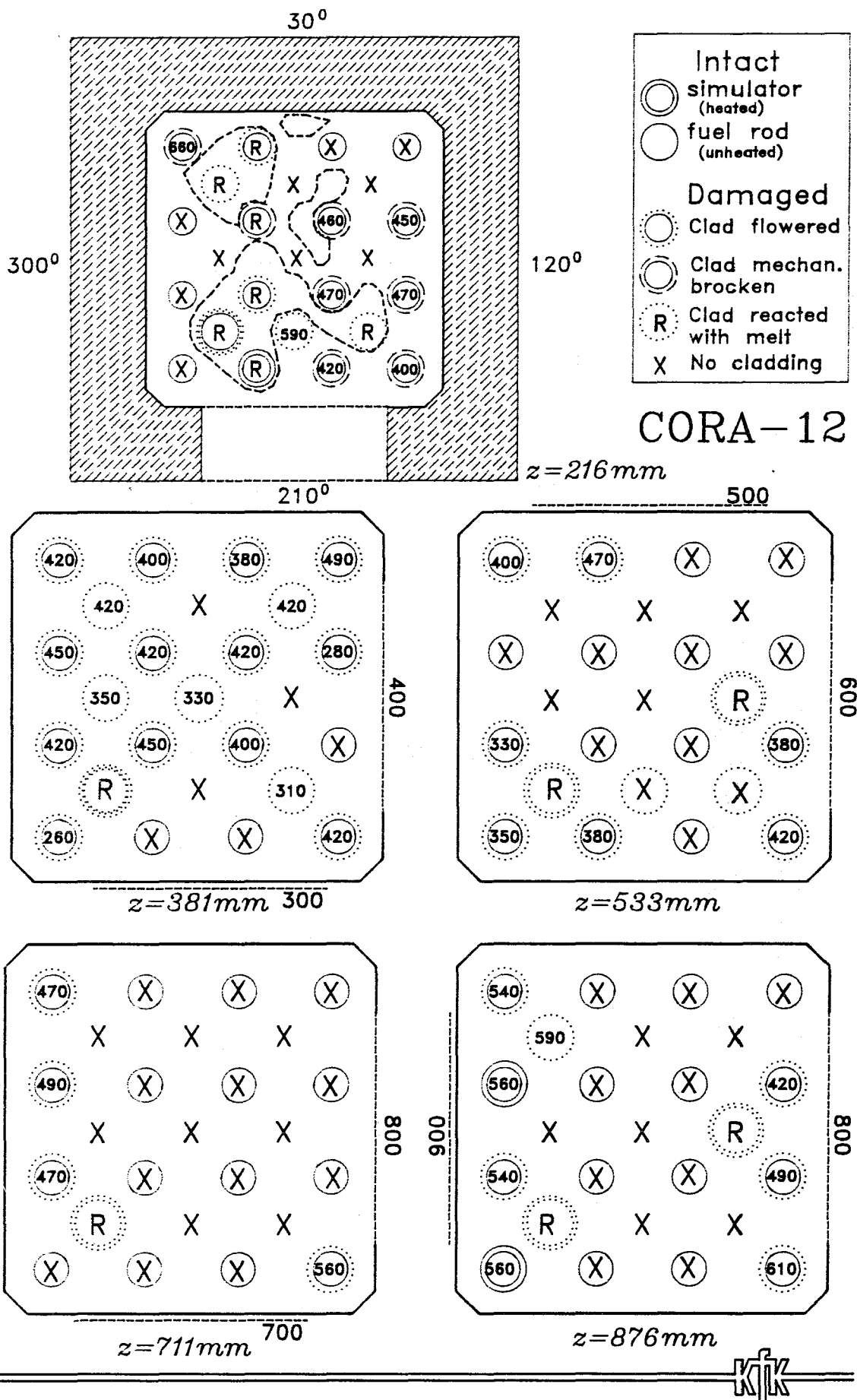
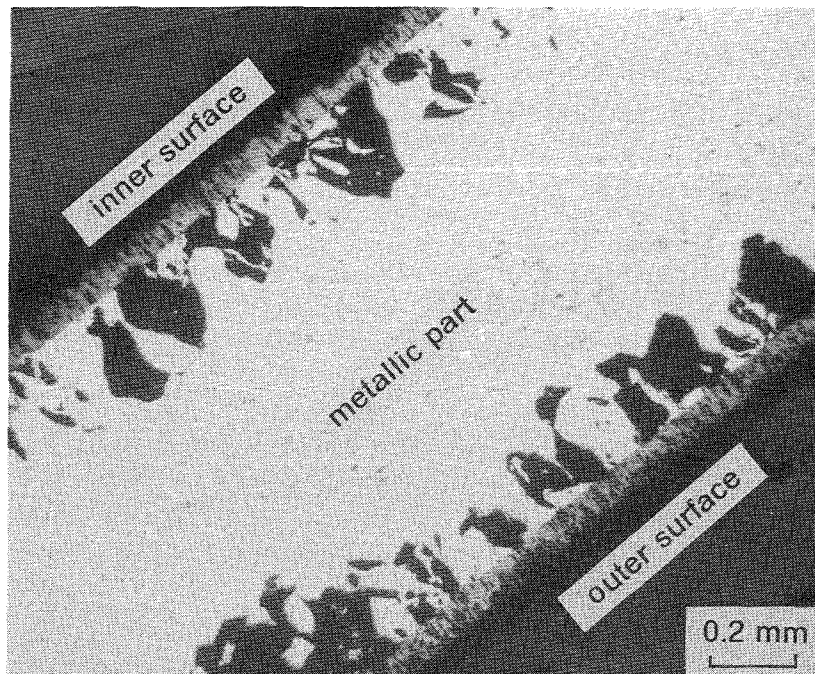


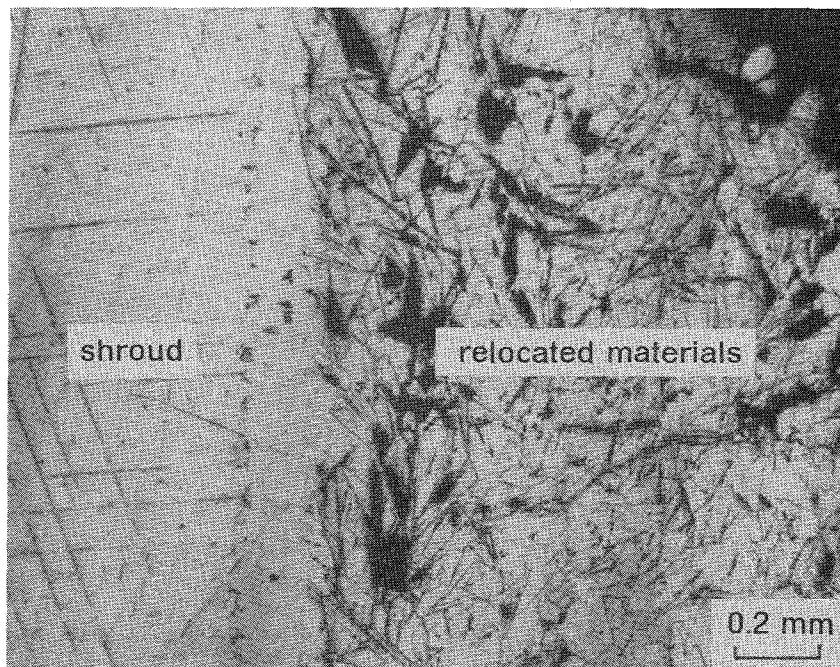
**Figure 32. CORA-12, axial and radial variation of the cladding state:** numbers indicate outer  $\text{ZrO}_2$  layer thicknesses in  $\mu\text{m}$ , and the boundaries of blocked areas are marked by dashed lines.

around 160 mm



(a)

around 100 mm



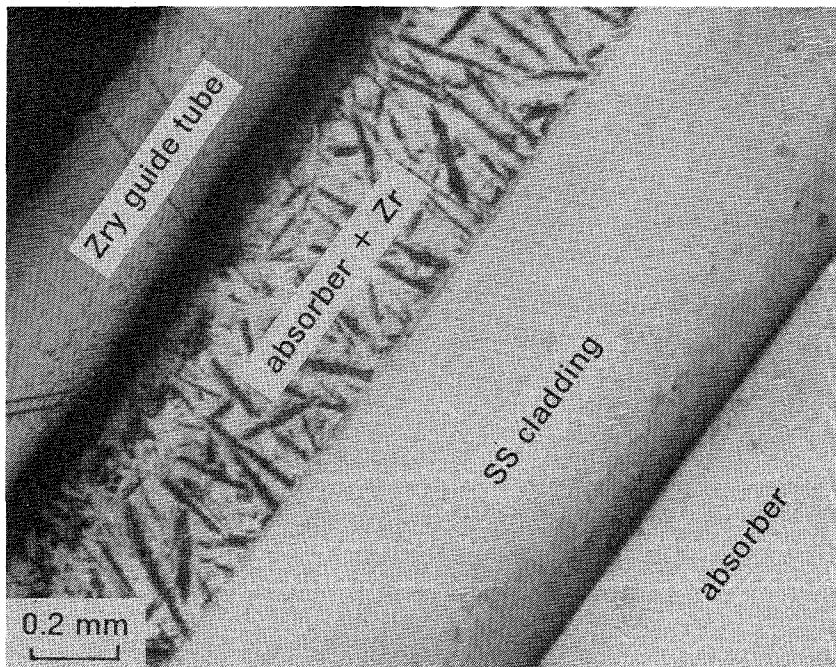
(b)



**Figure 33. CORA-12, shroud oxidation:** (a) double-sided oxidation in the direction of  $300^{\circ}$  at around 160 mm; (b) relocated melt at the outer surface of the shroud in the direction of  $120^{\circ}$  at around 100 mm.



around 100 mm



---

The logo for KFK, consisting of the letters 'KFK' in a stylized, bold, sans-serif font. The letters are interconnected, with the 'K' and 'F' sharing a vertical stroke. The logo is positioned to the right of a horizontal line that spans the width of the page.

**Figure 34. CORA-12, absorber rod:** absorber melt within the ss cladding and relocated material between ss cladding and Zry guide tube at around 100 mm.

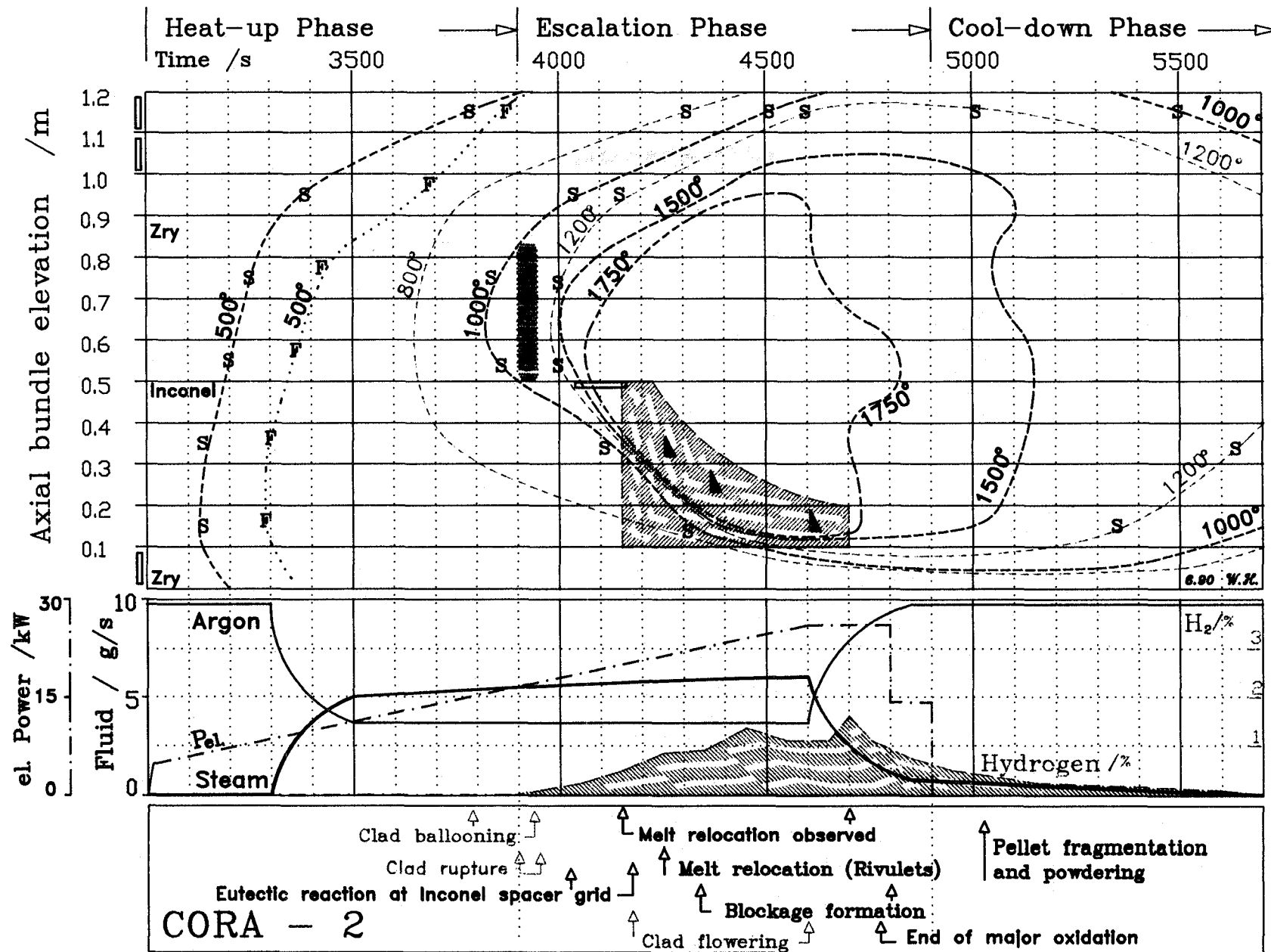


Figure 35. Isothermal diagram of CORA-2: showing temperature front lines in the uppermost part including clad failure (dotted area) and melt relocation observed (dashed area), fluid composition and electric power input (middle). The lowest part contains the sequence of phenomena derived from the test analysis [17].



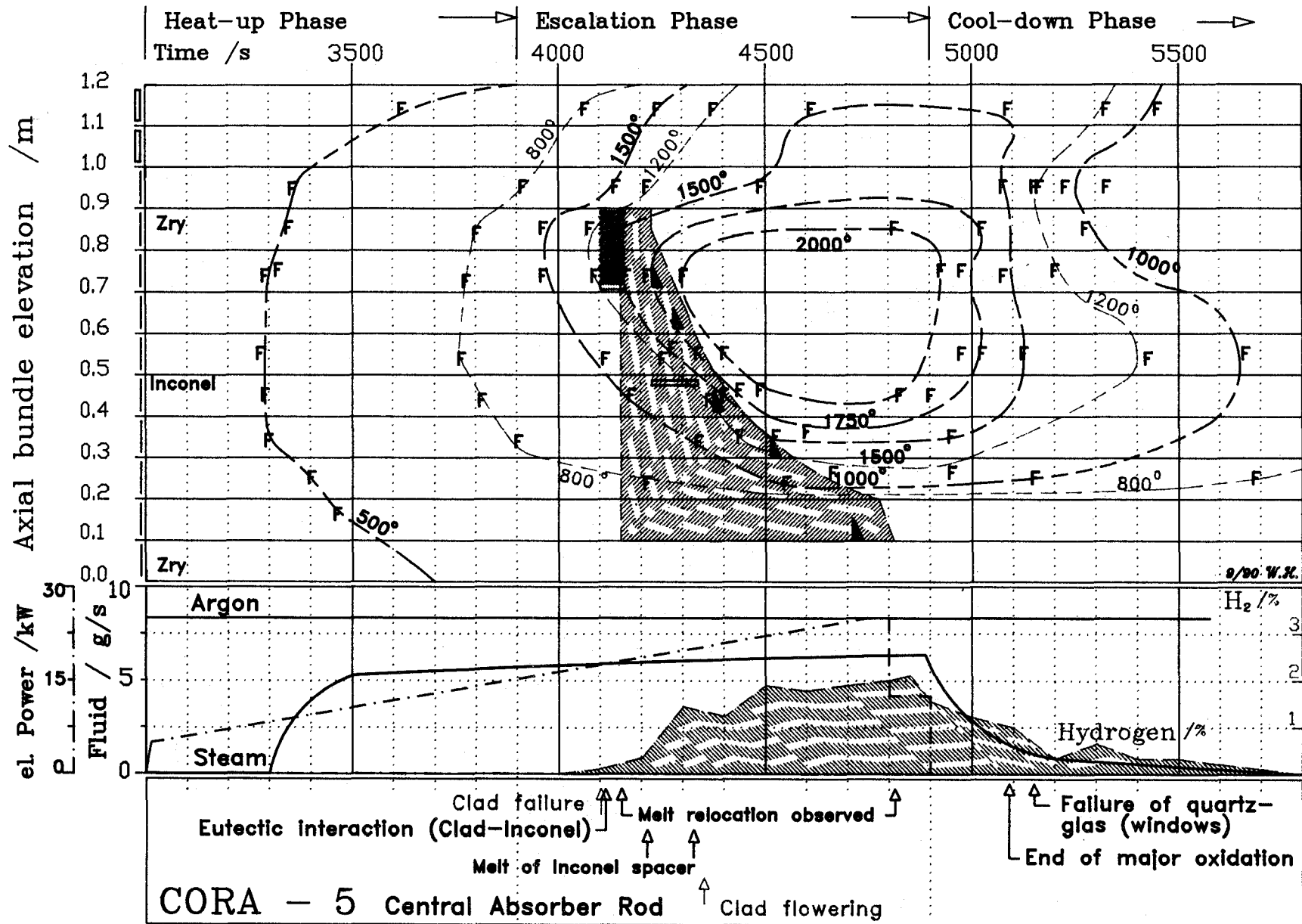


Figure 36. Isothermal diagram of CORA-5: showing temperature front lines in the uppermost part including clad failure (dotted area) and melt relocation observed (dashed area), fluid composition and electric power input (middle). The lowest part contains the sequence of phenomena derived from the test analysis /17/.

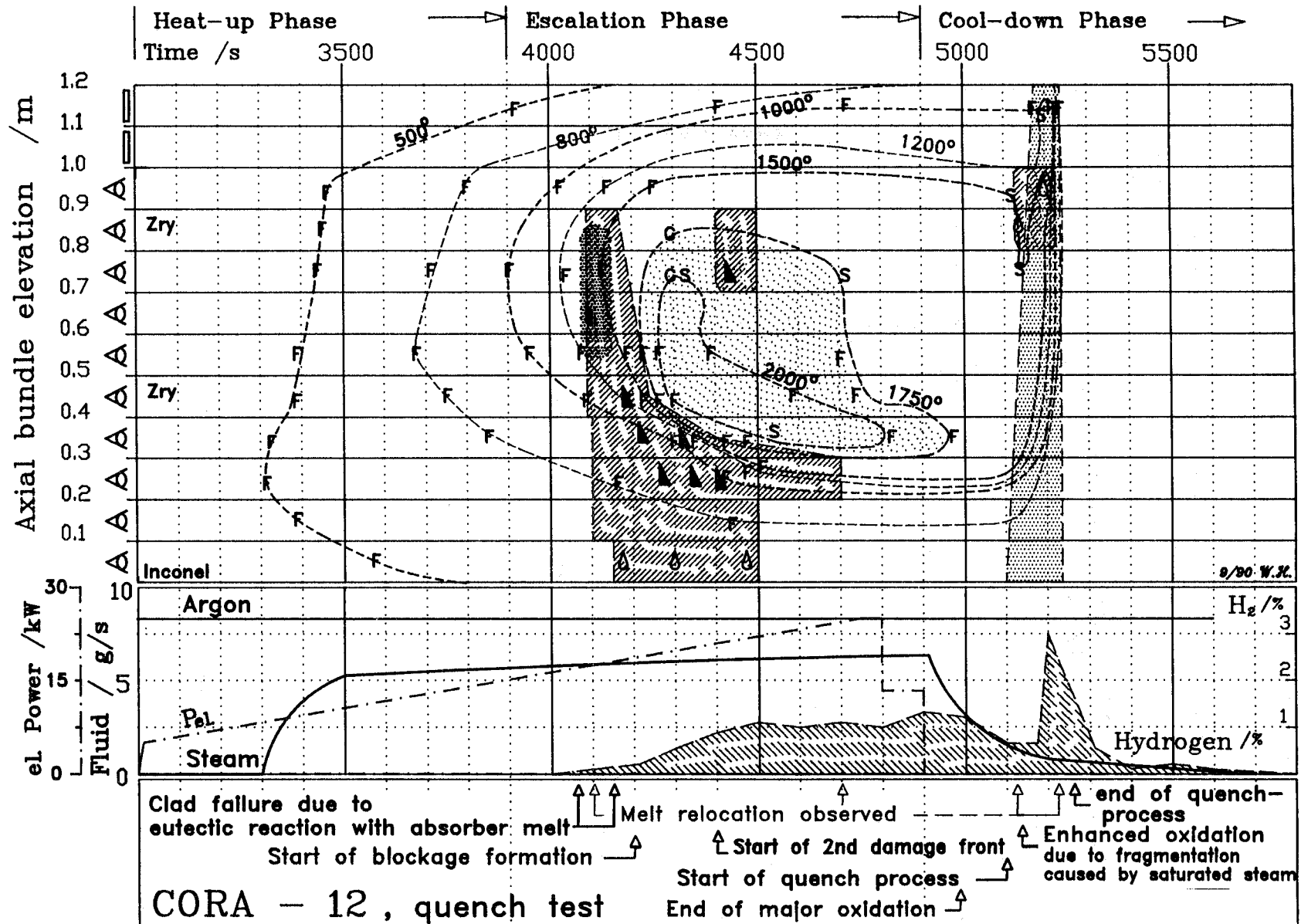
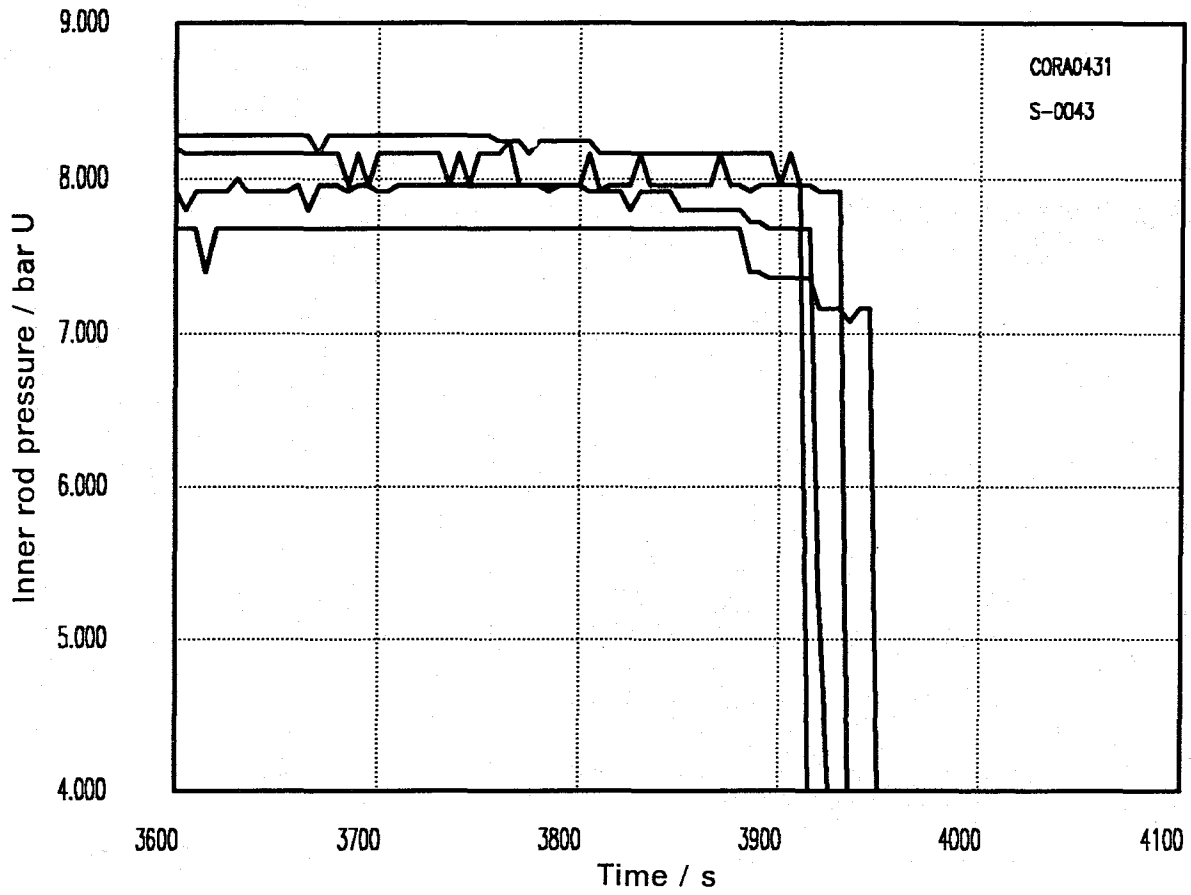
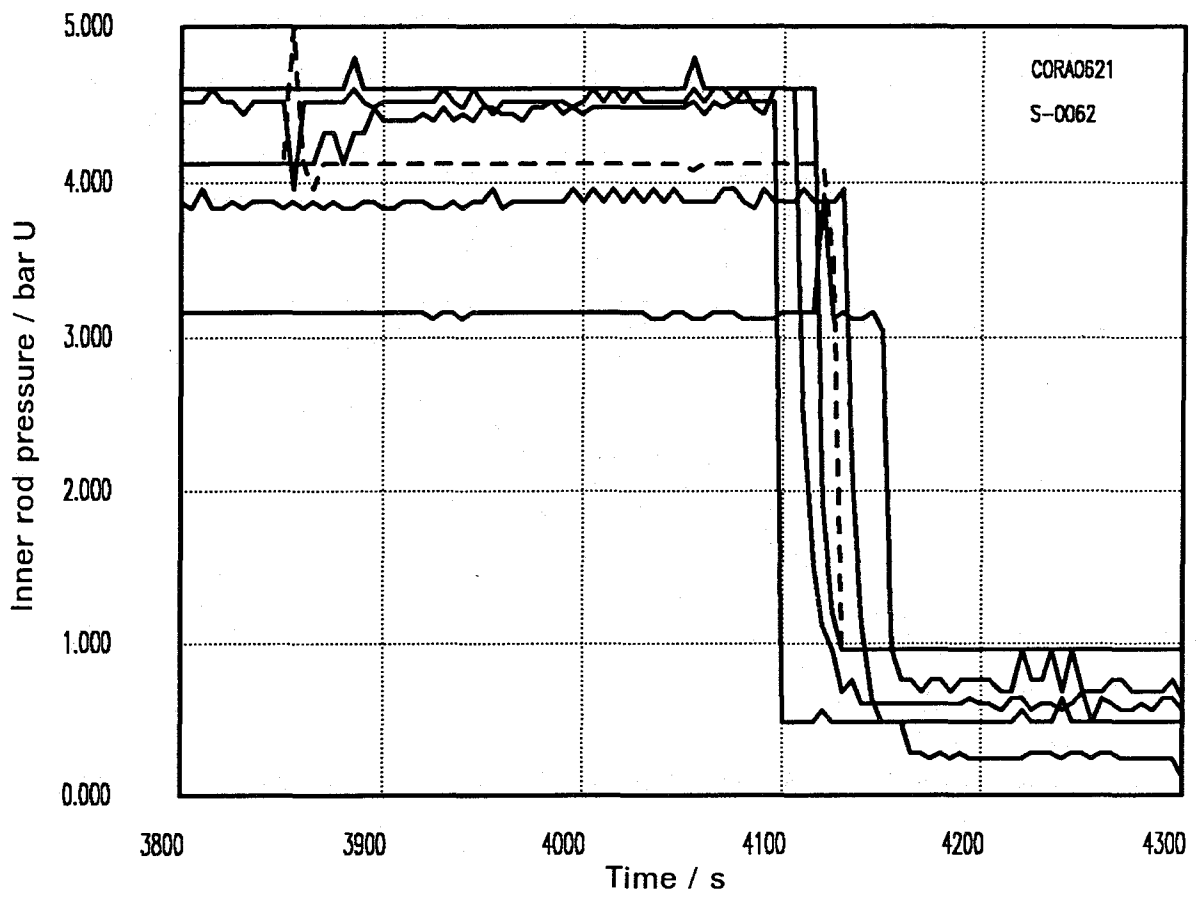


Figure 37. Isothermal diagram of CORA-12: showing temperature front lines in the uppermost part including clad failure (dotted area) and melt relocation observed (dashed area), fluid composition and electric power input (middle). The lowest part contains the sequence of phenomena derived from the test analysis /17/.



**Figure 38. CORA-2, inner rod pressure:** measured for unheated and heated fuel rods.



**Figure 39. CORA-5, inner rod pressure:** measured for unheated and heated fuel rods.

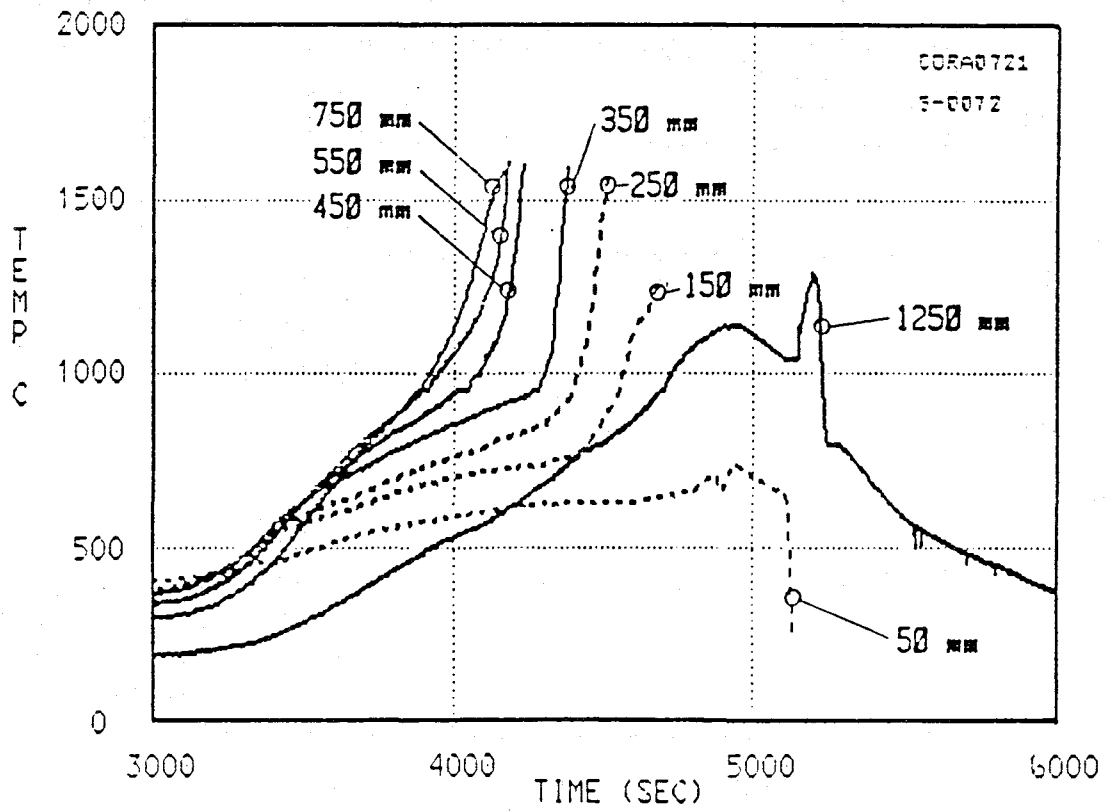


**Figure 40. CORA-12, temperatures of fuel rods:** rapid temperature increase in the cool-down phase at 1250 mm elevation.

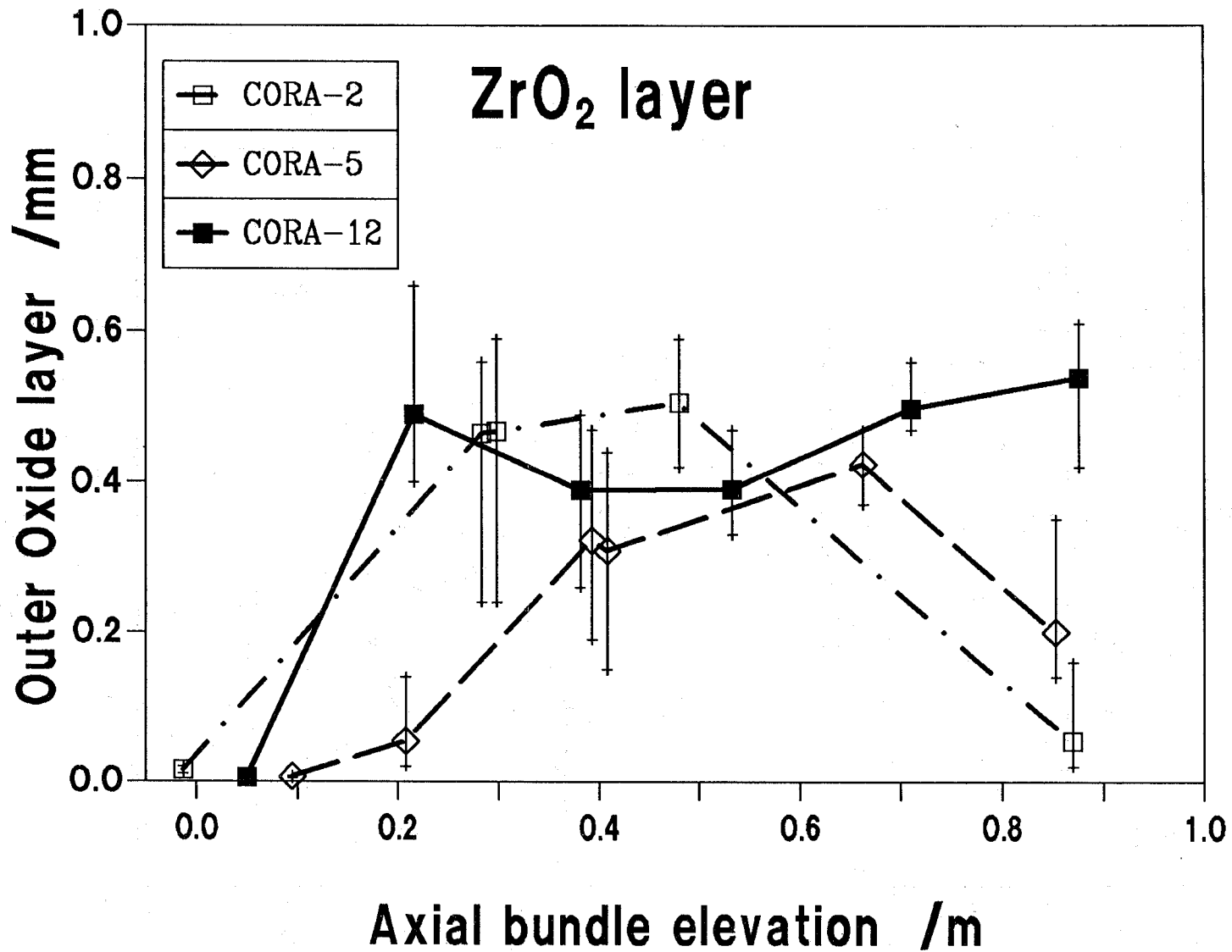
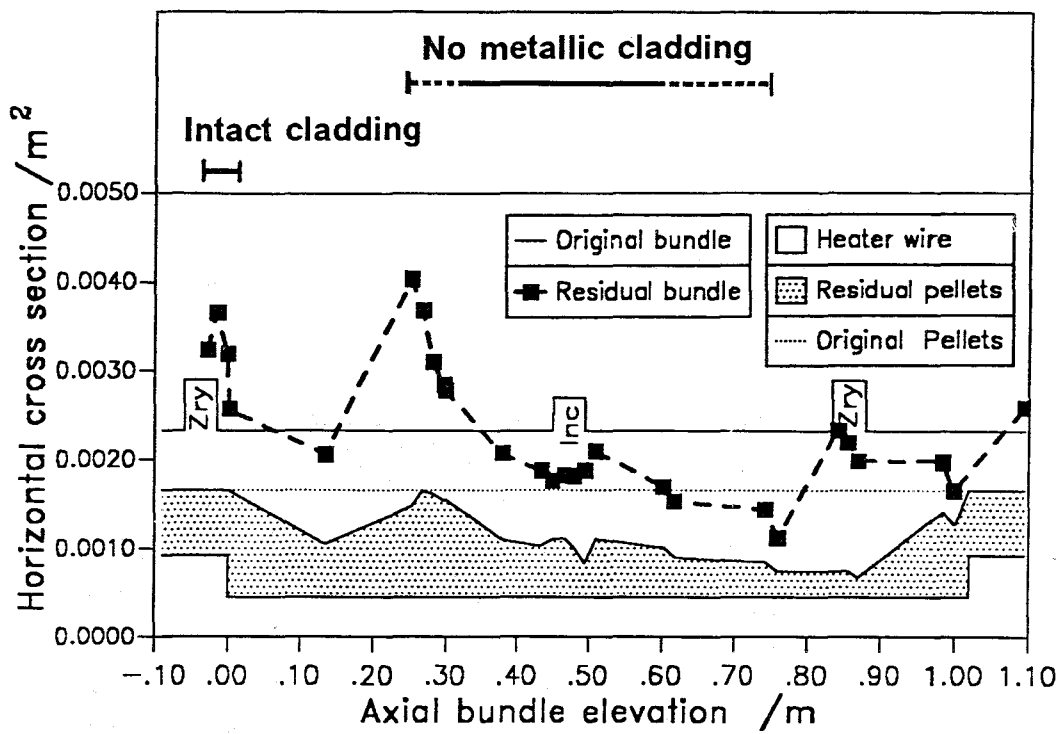
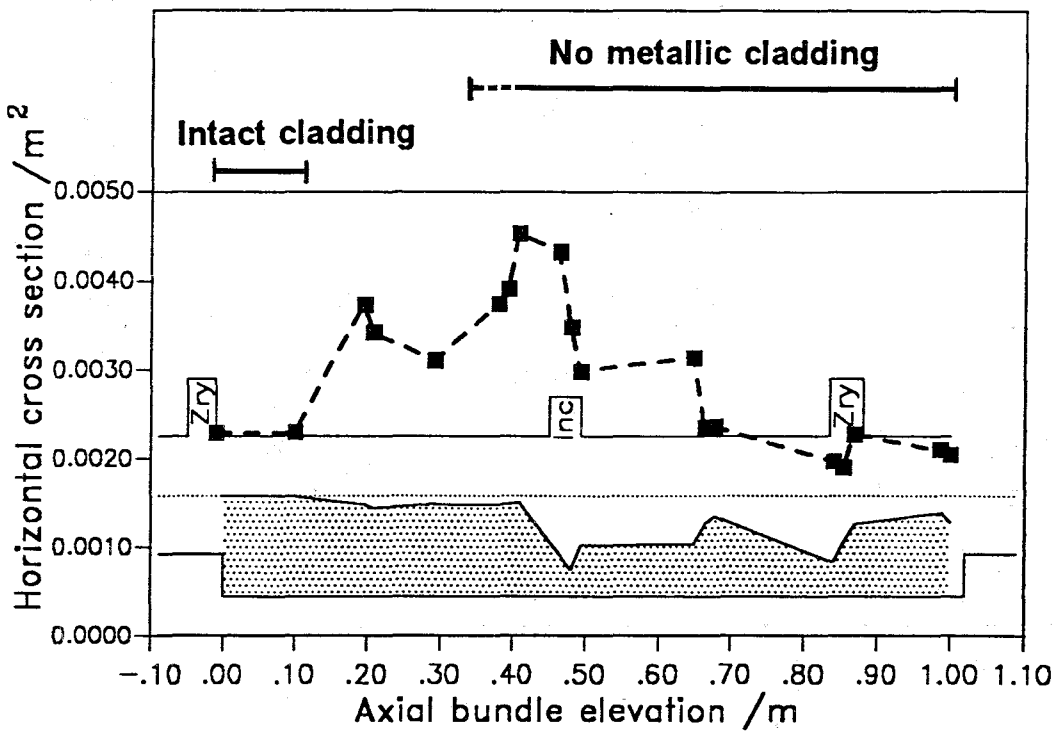


**Figure 41. Outer oxidized layer thicknesses:** comparison of the average values between CORA-2, CORA-5, and CORA-12. Vertical bars indicate the range of measured values.



**CORA-2**



**CORA-5**



**Figure 42. Comparison of the bundle end state:** between CORA-2 (top) and CORA-5 (bottom). The axial profiles in the lower parts of each figure are quoted from ref./14/.

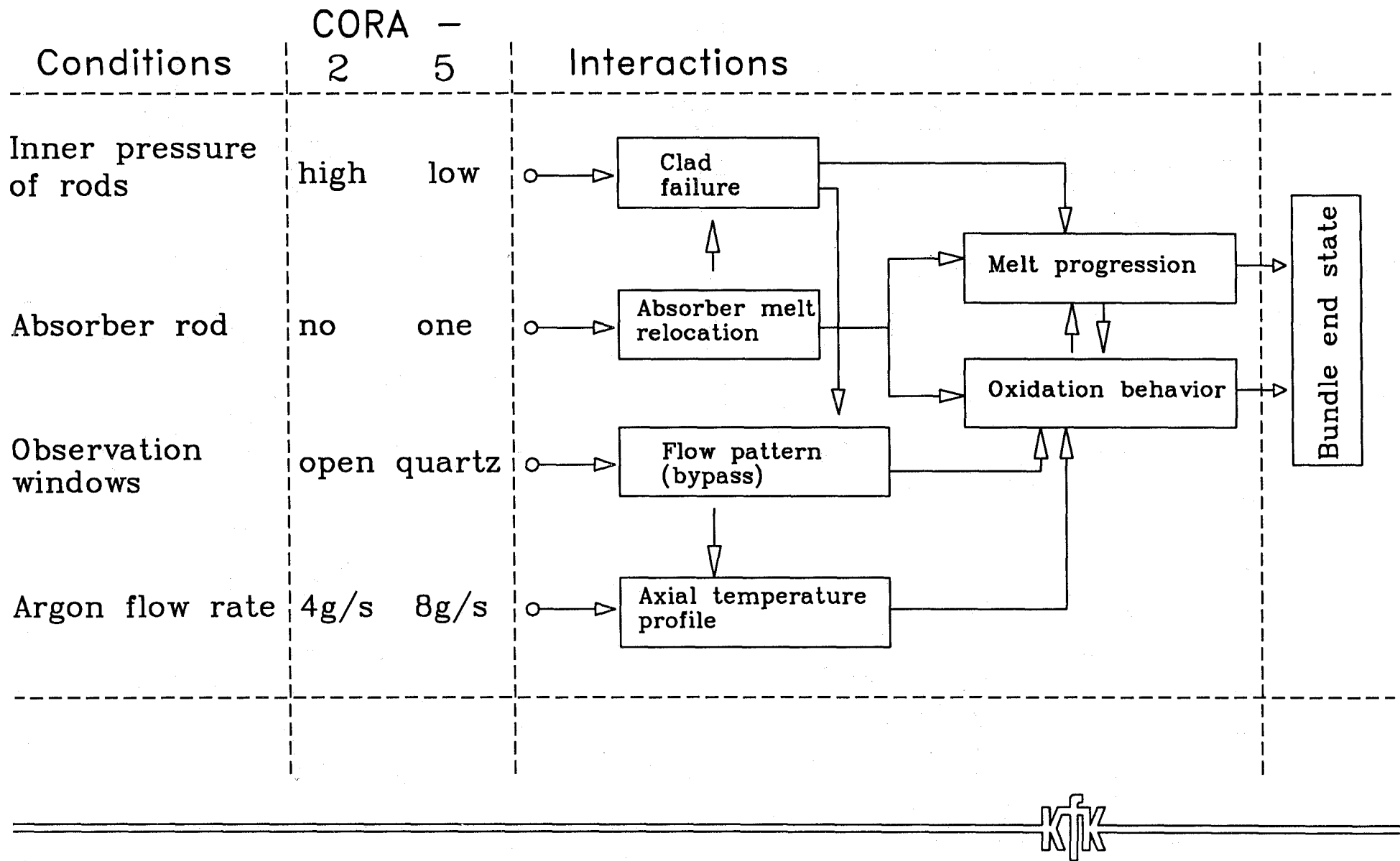


Figure 43. Comparison of the experimental conditions: differences and their influence on the damage progression.



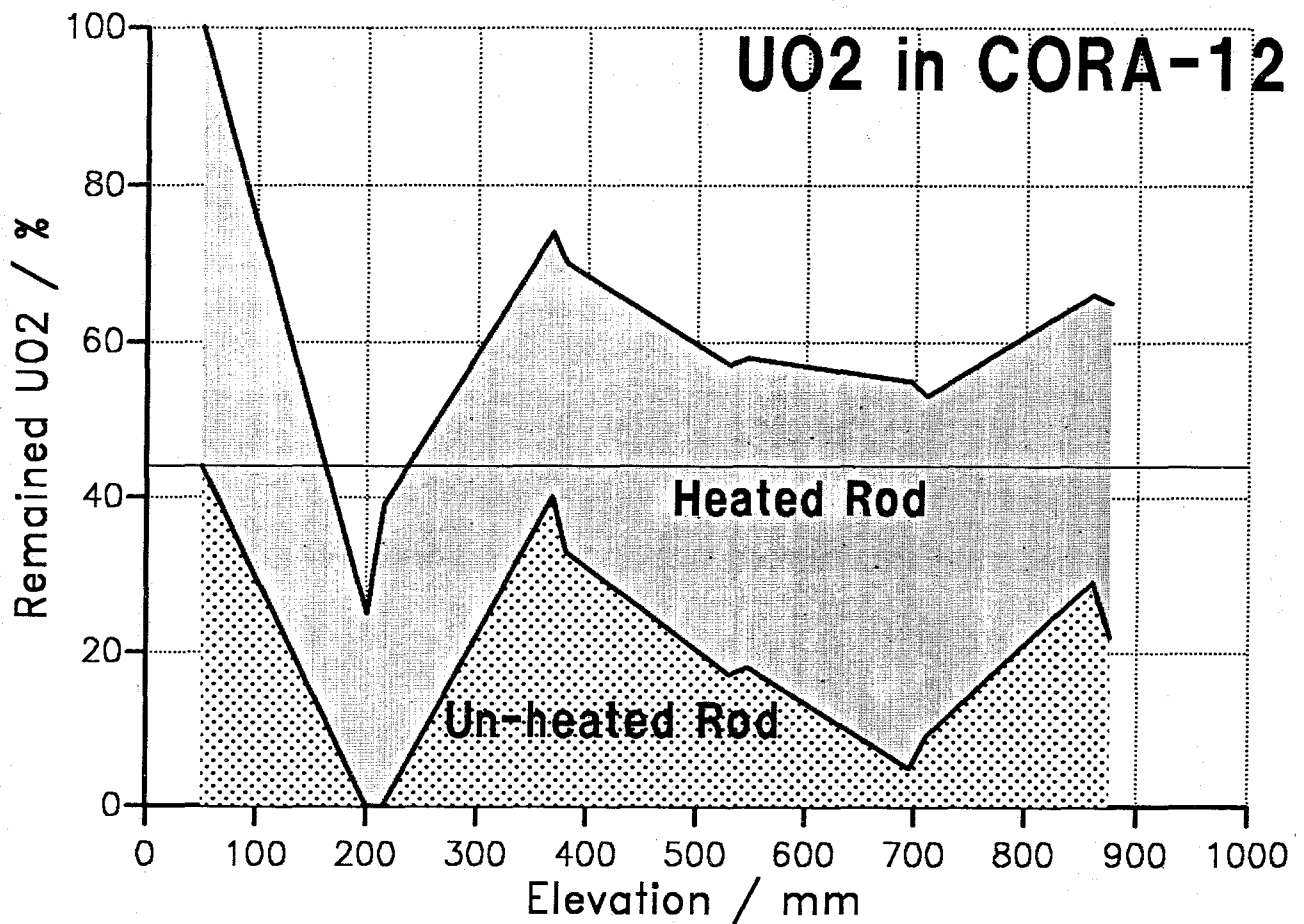
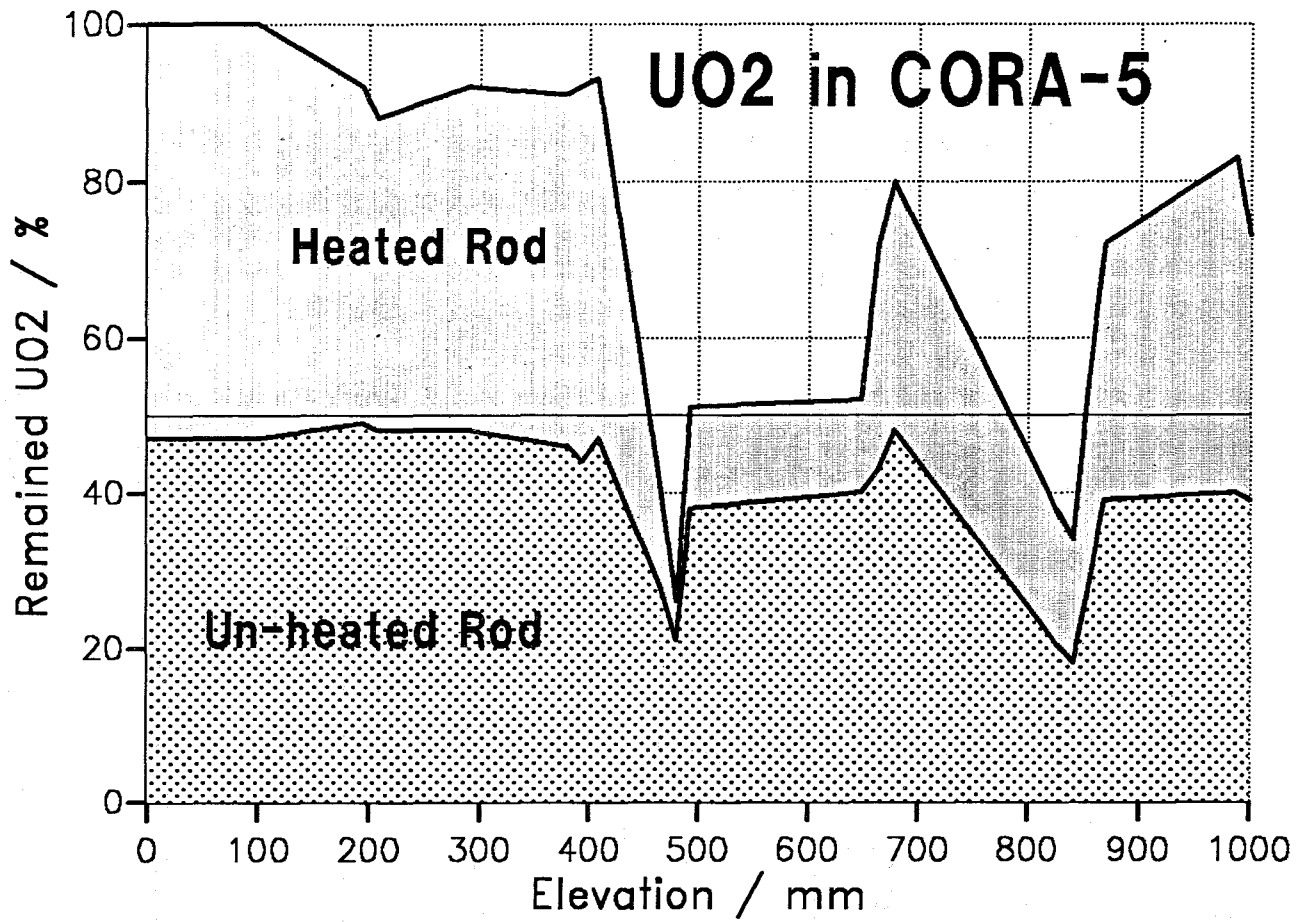


Figure 44. Comparison of the remnants of the pellets: these results are quoted from ref./14/.

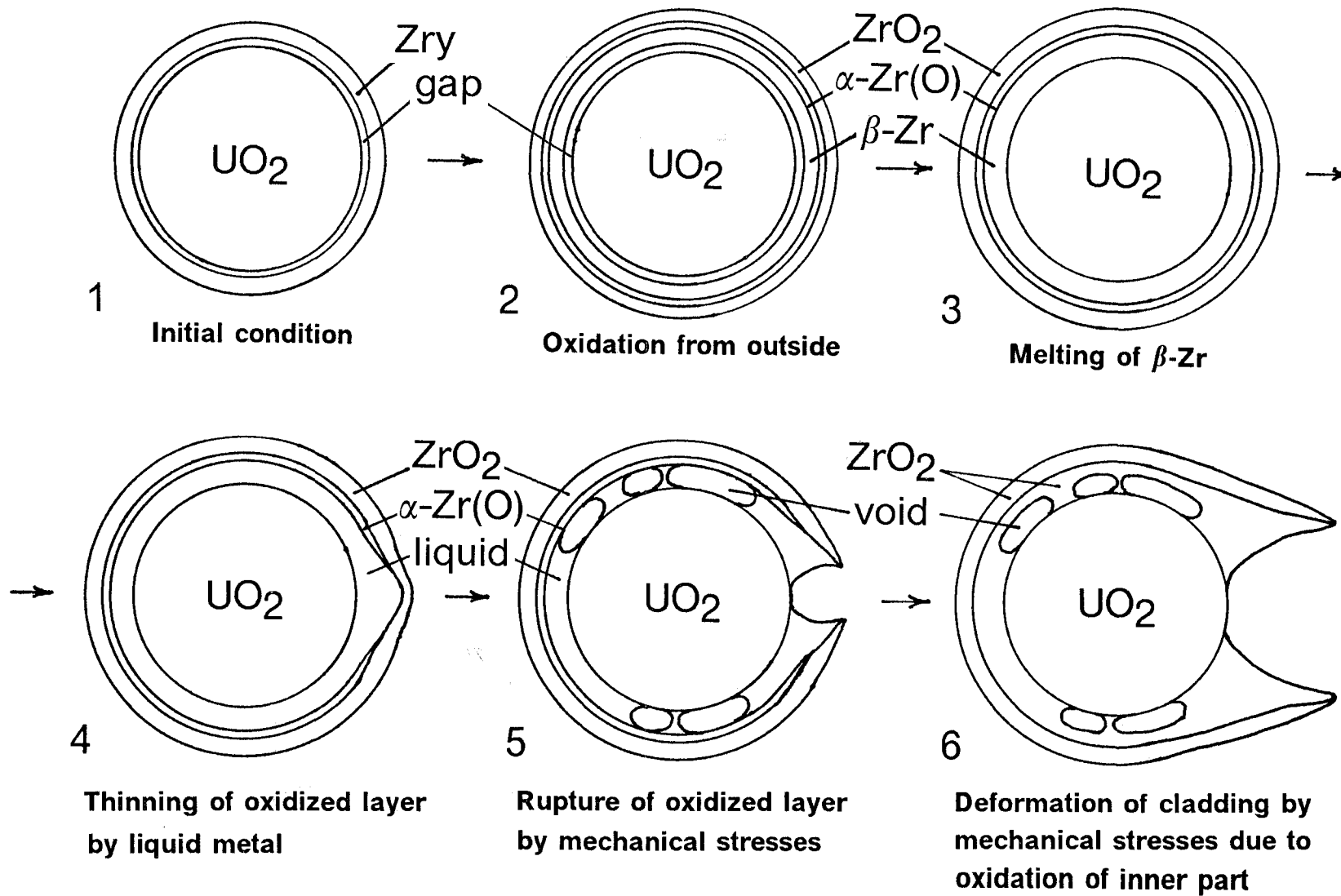


Figure 45. Mechanism of cladding deformation: intermediate states of the proposed model leading to failure and release of melt.